

AN ABSTRACT OF THE THESIS OF

Thomas Charles Lippmann for the degree of Master of Science

in Oceanography presented on February 22, 1989

Title: The Stability and Spatial Variability of Sand Bar Morphology

Redacted for privacy

Abstract Approved: _____

The temporal stability and spatial variability on nearshore sand bar morphology are investigated using a new remote sensing sampling technique and a unique data set spanning two years. The technique rapidly and accurately measures the scales of bar morphology based on the preferential dissipation of incident waves over the shallows of the bar. Video images are recorded and statistical uncertainties associated with wave height modulations are removed by averaging (time exposures). Ground truth testing of the technique was carried out as part of the SUPERDUCK experiment in October, 1986. The time exposures generally provide a good mapping of underlying morphology, allowing detection of the bar and determination of cross-shore and longshore length scales. However, during high waves, persistent surface foam on the shoreward side of the bar crest biases our approach, over estimates the landward extent of the bar crest, and therefore an image differencing technique is needed to remove the bias.

The video technique has been employed over a two year period from October, 1986 to October, 1988 at the SUPERDUCK field site located at the Army Corps of Engineers (CERC) Field Research Facility in Duck, N. C. The data consists of daily conventional and differencing time exposure images covering a beach area extending 660m alongshore and 200m offshore. Morphology in each image is visually classified into an eight state

scheme in which bars are uniquely defined by four descriptive criteria. The model encompasses the full range of possible morphologies from fully dissipative to fully reflective. Definitions of intermediate states serve as an improvement over previous models in the ability to better resolve differences in three-dimensional bar structure. Environmental control using incident wave height reveals that linear bars occur under highest wave conditions ($\bar{H}_s = 1.78\text{m}$) and are relatively unstable (mean residence time ≈ 2 days), whereas shore-attached crescentic bars are the most stable (mean residence time ≈ 11 days) and generally form 5-16 days following peak wave events. Non-rhythmic, three-dimensional bars appear to be transient states (mean residence time ≈ 3 days) irrespective of proximity to the shoreline. Transitions to lower states tend to occur one step at a time (87%) under declining wave conditions, thus representing an accretional progression. Transitions to higher states generally occur under rising wave conditions, indicative of an erosional progression, and are spread more evenly between single (49.5%) and multiple step jumps, with more substantial changes in morphology resulting from larger wave increases.

Time exposure images are also digitized to yield quantitative estimates of bar crest position. The relationship of image intensity to local wave dissipation is modelled by dissipation of a random wave field (after Thornton and Guza, 1983), yielding a theoretical understanding of the physics involved in imaging dissipation. Errors in bar crest estimation are generally less than 35% ($\sim 5-10\%$) of the bar-shore distance, but this value depends on the geometry of each particular profile. Principal component analysis is used to decompose bar position into two-dimensional (linear) and three-dimensional (longshore variable) components. Cross-shore (linear) bar position ranges $\pm 50\text{m}$ (27m standard deviation) about the two year mean and dominates bar variability (74.6%). Three-dimensional bar structure accounts for $\sim 14\%$ of the variance (12m standard deviation). Changes in incident wave height precede cross-shore bar migration by less than one day. Changes in longshore variability are inversely correlated to changing wave conditions, with

bar morphology becoming linear rapidly during storms (on time scales of less than one day). Evolution to significantly three-dimensional structure typically occurs over 5-7 days following peak wave events.

The Stability and Spatial Variability of Sand Bar Morphology

by

Thomas Charles Lippmann

A THESIS

submitted to

Oregon State University

in partial fulfillment of
the requirements for
the degree of

Master of Science

Completed February 22, 1989

Commencement June 1989

APPROVED:

Redacted for privacy

Associate Professor of Oceanography in charge of major

Redacted for privacy

Dean of College of Oceanography

Redacted for privacy

Dean of Graduate School

Date thesis is presented February 22, 1989

Typed by Thomas C. Lippmann

ACKNOWLEDGEMENTS

Since my advisor, Dr. Rob A. Holman, hired me more than three years ago, I'm sure he has had many anxiety attacks watching me grow/flounder in the realm of nearshore science. But for some reason, unbeknownst to most, he has managed to accept me as I am. I thank him for that, and also for his generosity in funding me and allowing me to take part in the many fun experiments and meetings that go along with being a scientist. He has also provided infinite wisdom and character-building advice to help me prepare for the future. So, boss, have a good weekend, from the "Young Seeker of Knowledge".

Other people have been instrumental in my learning process, particularly Dr. Joan Oltman-Shay and Pete Howd. They have always been there to discuss various aspects of my work and provide valuable insight. Paul O'Neill has been extremely generous with his time and effort in helping me ease into the world of computers and experimental instrumentation, and without him this work would not have been possible. Another person deserving thanks is Marcia Turnbull, without whom I would have finished months ago.

Life here in Oceanography was made very enjoyable by the many people I have become associated and to them I give thanks; in particular, to Appelgate, Finney, Murray, John, Margaret, Todd, Cindy, Sara, Steve, Annette, Collin, Beth, Erika and Brian, Marcia, Kathryn, Jim, Chuck, Jim, Tom, Mary Lynn, Dave, Linda, the Mauling Pellets, Neptune, and, of course, N/A. Further thanks to the "people from the North" at Dalhousie University and Halifax, Nova Scotia, especially Dr. Jerk, Meredith, Hebert, and Michelle, for making my stay there memorable. Thanks to Bruce Finney and Dale Adkins for helping me to "grow in the knowledge of fish and their ways", and to Bruce Appelgate, Dave Murray, and Finney for being such good sports after I squashed them in squash. Special thanks to Pete and Kathryn Howd and Mark and Vicki Lorang for putting up with me and letting me maintain my, at times, unconventional lifestyle.

Special thanks to those people who made me laugh and kept my sights in perspective, including Lip, BEL, Shoe, Fish, Free, Aguirre, Momuru, Hilgy, Shaf, Kush, Kent, Tad, Stapes, Todd, and Appleblossom. My old and best friends will never be forgotten (since they keep reminding me how much I owe them). I guess some of their zest for life's simple pleasures has rubbed off on me (in the form of headaches?), and with their unselfish guidance I have tried to adopt a more basic, but worldly, existence with priorities which are best summed up by Matt Fishback: "The guy with the most toys in the end wins."

I appreciate the time and insight provided by my committee members Dr. Paul Komar, Dr. Chuck Rosenfeld, and Dr. Peter Dawson. I am indebted to the entire staff at the FRF in Duck, N.C., for without their conscientious efforts this work could not have been completed. In particular I would like to thank Curt Mason, Bill Birkemeier, and Harriet. Funding for this work was provided by the Office of Naval Research, Coastal Sciences Program, under contract N00014-84-0218 and the U.S. Army Corps of Engineers, Coastal Engineering Research Center under the Barrier Island Sedimentation work unit.

This thesis is dedicated to Sondra Jane Lippmann, my mother, who showed me the value of an education and the lighter side of life's struggles, and provided me with an opportunity to explore the far reaches of that vast void in my head, sometimes referred to as my brain.

TABLE OF CONTENTS

	GENERAL INTRODUCTION	1
CHAPTER I	QUANTIFICATION OF SAND BAR MORPHOLOGY: A VIDEO TECHNIQUE BASED ON WAVE DISSIPATION	4
	ABSTRACT	5
	INTRODUCTION	6
	THEORY	10
	Random Wave Model	11
	Application of the Model	13
	Examples	14
	PHOTOGRAMMETRY	23
	THEORETICAL RESOLUTION AND ACCURACY	28
	FIELD TECHNIQUES	31
	RESULTS	39
	Time Exposures	39
	Differencing Time Exposures	46
	Shoreline Agreement	53
	DISCUSSION	56
	CONCLUSIONS	58
	ACKNOWLEDGEMENTS	60
CHAPTER II	THE STABILITY AND SPATIAL VARIABILITY OF SAND BAR MORPHOLOGY	61
	ABSTRACT	62
	INTRODUCTION	63
	METHOD OF SAMPLING MORPHOLOGY	67

METHODS OF CHARACTERIZING MORPHOLOGY	69	
Sequential Classification Scheme	69	
Longshore Structure in Bar Crest Position	80	
FIELD TECHNIQUES AND DATA COLLECTION	83	
RESULTS	86	
Morphologic Stability	86	
Longshore Variability in Bar Morphology	94	
DISCUSSION	104	
CONCLUSIONS	109	
REFERENCES	111	
APPENDIX A	TRANSITION TABLES	116
APPENDIX B	CROSS-CORRELATIONS	120

LIST OF FIGURES

<u>Figure</u>		<u>Page</u>
I - 1	(a) Oblique snap-shot of wave breaking on October 10, 1986 at low tide during the SUPERDUCK experiment. (b) A ten-minute time exposure from the same date and tide. The white band at the shoreline is the dissipation maximum corresponding to the shore break, while the band offshore indicates the presence of a sand bar.	8
I - 2	Model results as waves are shoaled over a plane beach profile (top panel). The behavior of H_{rms} and $\langle \epsilon \rangle$, plotted against offshore distance, is shown for the random wave model in the bottom panel.	16
I - 3	Model test results for wave shoaling and dissipation over a surveyed profile (top panel) from Torrey Pines beach on October 20, 1978. The cross-shore behavior of H_{rms} and $\langle \epsilon \rangle$ are shown for the random wave model in the lower panel.	17
I - 4	Model results for wave shoaling and dissipation over a barred beach profile (top panel) from SUPERDUCK on October 11, 1986. The cross-shore behavior of H_{rms} and $\langle \epsilon \rangle$ are shown for the random wave model in the lower panel.	18
I - 5	Influence of deep water rms wave height, H_0 , over a barred beach profile (top panel) from SUPERDUCK on October 11, 1986. The effect of increasing H_0 on dissipation, $\langle \epsilon \rangle$, and local wave height, H_{rms} , at offshore locations are shown in the middle and lower panels, respectively.	20
I - 6	Fractional error in locating the bar crest from theoretical dissipation maxima plotted against non-dimensional wave height, H_C^* .	22
I - 7	Geometry and labeling conventions used for photogrammetry.	24

- I - 8 Map of the field site during the October portion of SUPERDUCK. 32
The stippled area indicates the ground coverage in the field of view of the camera. Cross-shore transect SD200 is the location of some example profiles in the text while SD210 is the location closest to the main instrument line in SUPERDUCK. Longshore spacing for the CRAB survey lines was 20 m (there exists an intermediate line, SD205, between the two lines indicated).
- I - 9 Rectified time exposure image obtained at low tide on October 16, 1986 34
encompassing the minigrid area. The longshore and cross-shore distances are scaled equally with ticmark spacing of 50 m. The thin white band indicates the shore break while the broader offshore band shows breaking over the bar. The relative size in raster width reflects the pixel resolution in the original time exposure.
- I - 10 Example cross-shore intensity profile and bathymetry for October 16, 1986 during SUPERDUCK. The intensity values are non-dimensional with absolute magnitudes that are not related to the bathymetry. 35
- I - 11 Three-dimensional oblique views of the minigrid survey during SUPERDUCK. (Courtesy Bill Birkemeier and the FRF). 36
- I - 12 Local bathymetry and cross-shore intensity profiles from a simple time exposure obtained at mid tide on October 6, 1986. The three transects were chosen as having the best-defined bars. 40
- I - 13 Rectified time exposure image encompassing the minigrid area obtained at low tide on October 11, 1986. The longshore and cross-shore distances are scaled equally with ticmark spacing of 50 m. The image contrast has been stretched to better reveal the bar location. The weak offshore intensity maximum corresponds to a poorly-defined second bar. 41
- I - 14 Location of the mean shoreline, measured bar crest (solid squares), and intensity maxima from simple time exposures obtained at low, mid, and high tide on October 11, 1986. The stippled area indicates the area around the crest for which the water depth is within 5% of h_c . 43
- I - 15 Shore-parallel transects centered over the mean bar distance, 60 m (upper panel) and 70 m (lower panel) offshore, from a simple time exposure obtained at low tide on October 16, 1986. Variations of intensity correspond to the underlying bathymetry. 45

I - 16	Rectified differencing time exposure obtained at low tide on October 12, 1986. The bright white band offshore indicates the presence of a sand bar, whereas the shoreline is indicated by a relative darkness within the shorebreak region. The longshore and cross-shore distances are scaled equally with ticmark spacing of 50 m.	47
I - 17	Location of mean shoreline, measured bar crest (solid squares), and intensity maxima from differenced time exposures obtained at low and mid tide on October 9, 1986. The stippled area indicates the area around the crest for which the water depth is within 5% of h_c .	49
I - 18	Local bathymetry and cross-shore intensity profiles from a differenced time exposure obtained at mid tide on October 9, 1986 for the three best-defined sand bar locations.	50
I - 19	Location of mean shoreline, measured bar crest (solid squares), and intensity maxima from differenced time exposures obtained at low, mid, and high tide on October 11, 1986. The stippled area indicates the area around the crest for which the water depth is within 5% of h_c .	51
I - 20	Location of mean shoreline, measured bar crest, and intensity maxima from differenced time exposures obtained at low, mid, and high tide on October 16, 1986. The stippled area indicates the area around the crest for which the water depth is within 5% of h_c .	52
I - 21	Results from differencing time exposures on October 9, 11-13, 15-16 showing the fractional error in locating the bar crest plotted against non-dimensional wave height, H_C^* . Negative $\Delta x/x_{bar}$ values indicate a landward offset in intensity bar location estimate.	54
I - 22	All shoreline intensity maxima locations from simple time exposures obtained at low, mid, and high tide on October 6, 9-16 plotted against measured shoreline location. The regression line is given by $y = -14.8 + 1.15x$ ($r = 0.92$).	55
II - 1	Six state classification scheme of Wright and Short, 1984, shown on the left side, and our eight state classification scheme, shown on the right side. Comparisons between the two models are indicated with arrows between similar morphologic states.	66

II - 2	Classification criteria arranged in a workable flow chart. Morphologic classifications are based on one tertiary and three binary decisions. Each individual morphologic bar type (from the right hand side of Figure 1) is uniquely defined in this manner.	71
II - 3	Example time exposures which best represent the six observed morphologies at the field site. a) <i>Bar Type B</i> ; August 9, 1987 b) <i>Bar Type C</i> ; January 10, 1988 c) <i>Bar Type D</i> ; October 17, 1987 d) <i>Bar Type E</i> ; January 25, 1987 e) <i>Bar Type F</i> ; March 6, 1987 f) <i>Bar Type G</i> ; December 25, 1986.	73
II - 4	Results from morphological classification tests showing the tendency to classify bar types in states other than the consensus state. The highest percentage of classified bar types defines the consensus bar type, also indicated by the bold letters in the upper left corner of each graph.	81
II - 5	Map of the field site for the two year data record. The position of the camera in relation to the FRF pier and the study area is indicated. Longshore and cross-shore distances are relative to the FRF coordinate system. The stippled area indicates the ground coverage in the field of view of the camera.	84
II - 6	Histograms of probability of bar occurrence (%), P_i (upper panel), total number of transitions, N_i , to each state (middle panel), and mean, τ_i , and standard deviations, s , of mean residence times for each state (lower panel).	88
II - 7	Histograms of \bar{H}_s , \bar{P}_0 , $\overline{H_s/L_0}$, and $\overline{H_s/T}$ for each bar type.	92
II - 8	Two year mean shoreline and bar crest position for differencing time exposure data (upper panel) and the corresponding standard deviations alongshore (lower panel). The longshore and cross-shore distances are relative to the FRF coordinate system shown in Figure 5.	95
II - 9	The first five EOF's from the decomposition of the differencing bar crest data. Spatial factors are shown on the left side, where the longshore distance is relative to the FRF coordinate system and the EOF values are non-dimensional. Corresponding amplitude time series are shown on the right side, along with relative variance contributions. The time scale (along the bottom) is in months, and the cross-shore distances are in meters and are relative to the two year mean (Figure 8).	96

II - 10	a) Cross correlation diagram showing $A(t)$ vs. H_s for lags out to ± 14 days. b) Same cross-correlations only with each time series detrended with their 21 day means prior to analysis. For each the negative lags indicate H_s leading. The 95% confidence intervals (dashed lines) were calculated using the long-lag artificial skill method after Davis, 1976.	98
II - 11	Cross correlation diagram showing $\Delta A(t)$ vs. ΔH_s for lags out to ± 14 days. The negative lags indicate ΔH_s leading. The 95% confidence intervals (dashed lines) were calculated using the long-lag artificial skill method after Davis, 1976.	99
II - 12	a) Cross correlation diagram showing $\Delta A(t)$ vs. $(\Delta H_s)_{\max}$ for lags out to ± 14 days. The negative lags indicate $(\Delta H_s)_{\max}$ leading. The 95% confidence intervals (dashed lines) were calculated using the long-lag artificial skill method after Davis, 1976. b) Plot of $\Delta A(t)$ (abscissa) vs. $(\Delta H_s)_{\max}$ (ordinate) for the maximum correlation observed at zero lag.	101
II - 13	Cross correlation $V(t)$ vs. H_s for lags out to ± 14 days. The negative lags indicate H_s leading. The 95% confidence intervals (dashed lines) were calculated using the long-lag artificial skill method after Davis, 1976.	102
II - 14	Cross correlation $\Delta V(t)$ vs. ΔH_s for lags out to ± 14 days. The negative lags indicate ΔH_s leading. The 95% confidence intervals (dashed lines) were calculated using the long-lag artificial skill method after Davis, 1976.	103
B - 1	Cross correlation $A(t)$ vs. P_0 for lags out to ± 14 days. The negative lags indicate waves leading. The 95% confidence intervals (dashed lines) were calculated using the long-lag artificial skill method after Davis, 1976.	121
B - 2	Cross correlation $A(t)$ vs. H_s/L_0 for lags out to ± 14 days. The negative lags indicate waves leading. The 95% confidence intervals (dashed lines) were calculated using the long-lag artificial skill method after Davis, 1976.	122
B - 3	Cross correlation $A(t)$ vs. H_s/T for lags out to ± 14 days. The negative lags indicate waves leading. The 95% confidence intervals (dashed lines) were calculated using the long-lag artificial skill method after Davis, 1976.	123
B - 4	Cross correlation $\Delta A(t)$ vs. ΔP_0 for lags out to ± 14 days. The negative lags indicate waves leading. The 95% confidence intervals (dashed lines) were calculated using the long-lag artificial skill method after Davis, 1976.	124

LIST OF TABLES

<u>Table</u>	<u>Page</u>
I - 1 Sampling time, wave conditions and video quality for morphology images discussed in the text.	38
II - 1 Classification criteria used to describe bar morphology. Each corresponding bar type uniquely defined in this manner is shown in the last column.	70
II - 2 Number of transitions to each bar to each bar type, N_i , and total number of observations, P_i , and average residence times, τ_i , for each bar type.	87
II - 3 Percent transitions between morphologic bar types. Initial states are along the top and resulting states are listed on the left. The total number of transitions to each state, N_i , are shown at the bottom of each column.	90
II - 4 \bar{H}_s (bold) and $\overline{\Delta H}_s$ for each transition. Initial states are along the top and resulting states are listed on the left. Statistics computed from less than 3 transitions are indicated with an asterisk.	93
A - 1 \bar{P}_0 (bold) and $\overline{\Delta P}_0$ for each transition. Initial states are along the top and resulting states are listed on the left. Statistics computed from less than 3 transitions are indicated with an asterisk.	117
A - 2 $\overline{H_0/L_0}$ (bold) and $\overline{\Delta H_0/L_0}$ for each transition. Initial states are along the top and resulting states are listed on the left. Statistics computed from less than 3 transitions are indicated with an asterisk.	118
A - 3 $\overline{H_s/T}$ (bold) and $\overline{\Delta H_s/T}$ for each transition. Initial states are along the top and resulting states are listed on the left. Statistics computed from less than 3 transitions are indicated with an asterisk.	119

- B - 5 Cross correlation $\Delta A(t)$ vs. $\Delta H_s/L_0$ for lags out to ± 14 days. The negative lags indicate waves leading. The 95% confidence intervals (dashed lines) were calculated using the long-lag artificial skill method after Davis, 1976. 125
- B - 6 Cross correlation $\Delta A(t)$ vs. $\Delta H_s/T$ for lags out to ± 14 days. The negative lags indicate waves leading. The 95% confidence intervals (dashed lines) were calculated using the long-lag artificial skill method after Davis, 1976. 126
- B - 7 Cross correlation $V(t)$ vs. P_0 for lags out to ± 14 days. The negative lags indicate waves leading. The 95% confidence intervals (dashed lines) were calculated using the long-lag artificial skill method after Davis, 1976. 127
- B - 8 Cross correlation $V(t)$ vs. H_s/L_0 for lags out to ± 14 days. The negative lags indicate waves leading. The 95% confidence intervals (dashed lines) were calculated using the long-lag artificial skill method after Davis, 1976. 128
- B - 9 Cross correlation $V(t)$ vs. H_s/T for lags out to ± 14 days. The negative lags indicate waves leading. The 95% confidence intervals (dashed lines) were calculated using the long-lag artificial skill method after Davis, 1976. 129
- B - 10 Cross correlation $\Delta V(t)$ vs. ΔP_0 for lags out to ± 14 days. The negative lags indicate waves leading. The 95% confidence intervals (dashed lines) were calculated using the long-lag artificial skill method after Davis, 1976. 130
- B - 11 Cross correlation $\Delta V(t)$ vs. $\Delta H_s/L_0$ for lags out to ± 14 days. The negative lags indicate waves leading. The 95% confidence intervals (dashed lines) were calculated using the long-lag artificial skill method after Davis, 1976. 131
- B - 12 Cross correlation $\Delta V(t)$ vs. $\Delta H_s/T$ for lags out to ± 14 days. The negative lags indicate waves leading. The 95% confidence intervals (dashed lines) were calculated using the long-lag artificial skill method after Davis, 1976. 132

THE STABILITY AND SPATIAL VARIABILITY OF SAND BAR MORPHOLOGY

GENERAL INTRODUCTION

An over simplified, but surprisingly astute, generalization of beach processes is that *big waves move sand* (P. V. O'Neill, pers. comm.). Clearly, though, much more complicated physical processes contribute to the control of coastal sedimentation, in which a common phenomena is the presence of nearshore sand bars (Komar, 1976). These large and mobile features constitute a major part of an interesting, and very complex, sediment transport regime. Since they are very dynamic, they can have a profound effect on the many physical processes impacting the nearshore environment.

Observations of various natural bar forms have been quite extensive in the literature. These observations range from linear bars with no longshore variability, to crescentic bars with regular longshore periodicity, to multiple barred beaches. The movement from one state to another has been of interest to many field studies, however the processes that govern this transition have not been clearly demonstrated. Past field studies have concentrated on two primary objectives: 1) developing equilibrium bar formation models which predict the scales of the bar, and 2) developing sequential morphological models which predict the shape of the bar.

In the first approach, investigators have devised conceptual models for linear bar formation through processes based on the shoaling and breaking regions of incident waves (Keulegan, 1948; Shepard, 1950; Miller, 1976; Greenwood and Davidson-Arnott, 1979), waves standing in the cross-shore, such as reflected incident waves, or progressive edge waves (Carter et al., 1973; Lau and Travis, 1973; Short, 1975; Bowen, 1980). The standing wave models have an advantage in that they predict the cross-shore length scale of the bar from the period of the standing wave.

Models have also been proposed for the generation of three-dimensional or crescentic bar forms. Bowen and Inman (1971) first showed that crescentic bars could be formed by the drift velocities associated with standing edge waves. This work was later extended by Holman and Bowen (1982) to the formation of oblique and other more complicated bar systems. These models also predict cross-shore length scales, and further predict the longshore length scale associated with periodic bar forms.

In the second approach of past field studies, emphasis has been on developing universal morphologic characterization schemes, which have an implied time dependence associated with the ordering of the model states. Many investigators have attempted to characterize bar changes using models which predict the behavior of morphology under varying beach and surf zone conditions (e.g. Sonu, 1973; Sonu and James, 1973; Chappell and Eliot, 1979; Short, 1979; Wright et al, 1979; Goldsmith, et al., 1982; Wright and Short, 1984). Other studies have concentrated on the response and behavior of periodically surveyed shore-normal transects (e.g. Aubrey, 1979, 1980; Sallenger, et al., 1985; Birkemeier, 1985; Howd and Birkemeier, 1987).

Despite these extensive research efforts little is known about time scales associated with the evolution of large scale three-dimensional morphology in response to changing wave conditions. This is due primarily to three difficulties associated with field methods: (1) sampling large scale bar forms at a rate sufficient to follow migration of the bar; (2) sampling with measurement accuracy necessary to quantitatively characterize longshore bar variability over large distances; (3) sampling techniques with logistic simplicity to allow for long term monitoring necessary to address morphologic stability under a wide range of environmental conditions.

The objective of this thesis is to address the temporal stability and spatial variability of nearshore sand bars. Particular emphasis is placed on morphologic changes associated with storm events, when the bar is evolving most rapidly. Chapter I presents a new remote sensing surveying method which eliminates most of the problems associated with previous

sampling approaches. This technique is based on the preferential dissipation of incident wind waves over the shallows of the bar. Video records of surf zone wave breaking are averaged over a ten minute period (created digitally with an image processing system, analogous to a traditional photographic time exposure), and used for visual and quantitative approximations of bar shape and position. In Chapter 2, the technique is used to examine the variability of a naturally occurring sand bar system over a two year period. For each daily time exposure image, visual assessment of overall bar morphology is made, as well as quantitative estimates of offshore bar position as a function of longshore distance. For each analysis, comparisons are made with incident wave parameters, and response time scales estimated.

Chapter I has been published in the Journal of Geophysical Research (1989, 94: 995-1011), with R. A. Holman as co-author. Chapter 2 will be submitted for publication in the same journal.

CHAPTER I

Quantification of Sand Bar Morphology: A Video Technique Based on Wave Dissipation

ABSTRACT

A technique is presented to remotely measure the scales and morphology of natural sand bars based on the preferential dissipation of wind waves and swell over the crests of the bar. Photographic or video images are recorded and statistical uncertainties associated with incident wave height modulations removed by averaging (time exposures). Ground-truth testing of the technique was carried out as part of the SUPERDUCK experiment in October, 1986. The time exposures generally provided a good mapping of underlying morphology, allowing detection of the bar and determination of cross-shore and longshore length scales. However, during high waves persistent surface foam obscures the relationship of image intensity to local dissipation (modelled theoretically by dissipation of a random wave field) and an enhancement technique of image differencing must be done to remove the bias. Errors in the estimate of bar crest distance from the shoreline are generally less than 35% but this value depends on the geometry of the particular bar. Logistic simplicity and quantitative capabilities make this technique very attractive.

INTRODUCTION

Offshore sand bars are common features of the world's coastlines. The accumulations of sediment into large scale features makes them an important, as well as interesting, sediment transport region. They are also very dynamic. While annual cycles in sediment deposition are observed on most coastlines (with offshore transport tending to form bars during higher energy wave conditions in winter months), significant morphological changes also occur on a much shorter time scale, especially in response to storms.

The physical processes that contribute to the dynamics of barred beaches are clearly not as simple as for plane beaches. Yet the new information available from studying these more complicated environments may provide valuable clues into the nature of the fluid-sediment interaction. In particular, cross-shore and longshore length scales of bars may potentially be related to fluid parameters if appropriate dynamical models are available. The literature contains a number of models for bar generation by fluid motions. It has been hypothesized that linear bars are formed at the breaker location of plunging incident waves (Keulegan, 1948; Shepard, 1950; Miller, 1976), or under nodes or antinodes of waves standing against the shoreline (Carter et al., 1973; Lau and Travis, 1973; Short, 1975; Bowen, 1980). Hypotheses exist for the formation of three-dimensional crescentic (Bowen and Inman, 1971), welded, and apparently aperiodic sand bars, based, for example, on the interaction of phase-locked edge waves (Holman and Bowen, 1982). Yet, surprisingly, these models are largely untested under natural conditions.

There are several reasons why field tests have not been accomplished. Proper measurement of the low frequency "surf beat", invoked by several of the models, requires sophisticated analysis techniques to resolve particular trapped (edge waves) and leaky modes. Though this technique requires a more extensive array of instrumentation than originally thought, it is now feasible (Huntley, et al. 1981; Oltman-Shay and Guza, 1987).

Measuring the morphology over large enough spatial scales and short enough time scales remains a major difficulty, exacerbated by the scientific emphasis on storm periods when bar evolution is occurring most rapidly. Traditionally, bar measurements are made using *in situ* field techniques that, due to hostile conditions in the surf zone environment, are not always easily applied. Also, the large scale of most bar forms require extensive surveying both cross-shore and alongshore, typically on the order of many hundreds of meters. Non-stationarity may lead to errors if the bar moves significantly during the surveying period. Hastening the surveying process can eliminate bar stationarity problems, but not without the inevitable loss in spatial resolution and the potential introduction of spatial aliasing.

We have developed a remote sensing technique that allows the visualization and subsequent quantification of nearshore morphology based on the patterns of incident wave breaking. The premise of the technique is that more waves break over the shallows of the bar than surrounding areas. The sharp contrast between breaking and non-breaking regions may be imaged photographically; however, instead of using an instantaneous "snapshot" we employ a long time exposure, thereby averaging out fluctuations due to incident wave modulations and giving a statistically stable image of the wave breaking pattern. Figure 1 illustrates the technique. The breaking wave pattern in Figure 1a suggests the presence of a sand bar, but the poor spatial coverage provided by breaking crests and the statistical uncertainty associated with natural modulations in wave height render the details of the bar morphology uncertain. In Figure 1b the breaking pattern has been averaged over a ten minute period in a time exposure. This image yields a much clearer view of the bar. Spatial coverage is both extensive and of high resolution. Non-stationarity problems are avoided since the sampling interval (ten minutes), is substantially



Figure I - 1. (a) Oblique snap-shot of wave breaking on October 10, 1986 at low tide during the SUPERDUCK experiment. (b) A ten-minute time exposure from the same date and tide. The white band at the shoreline is the dissipation maximum corresponding to the shore break, while the band offshore indicates the presence of a sand bar.

less than the observed time scales of appreciable bar movement (Sallenger et al., 1984). Finally, the logistics of the remote measurement technique are not constrained by high energy surf zone conditions, and can be utilized wherever an adequate vantage point is accessible.

There has been some work on this problem as early as the 1940's using aerial photography (e.g. Wiegel, 1947; Lundall, 1948; Harris and Umbach, 1972), however with large uncertainties resulting from the small number of infrequent observations and limited knowledge of the precise connection between instantaneous visual wave breaking patterns and underlying topography. Our approach will greatly improve these estimates and allow for quantitative evaluation of the technique.

Our discussion of the technique will start with the theoretical background. To understand the relationship between the light intensity patterns observed in time exposure images and the underlying morphology we make a working assumption that light intensity will vary as the dissipation of the incident waves. Modelling of dissipation over arbitrary topography using the random wave model of Thornton and Guza (1983) then gives guidance to the expected performance of the technique (while measured light intensity profiles turn out to be very similar to calculated profiles of dissipation, lending support to our assumption, we do not actually test this hypothesis by measuring wave dissipation). Following the theory is a section on the photogrammetry involved in the transformation of oblique images. The theoretical resolution and accuracy of the technique is then discussed, followed by a description of our field methods and laboratory digitization techniques using a computerized image processor. Finally, we will discuss field tests based on field data from the 1986 SUPERDUCK experiment (Crowson et al., 1988).

THEORY

The patterns of light intensity that are recorded in the time exposure photographs are a result of the bubbles and foam of breaking waves. To relate this visible signal to the fluid motions (and hence the underlying bar morphology) we must make some assumption about the mechanism of bubble formation. For the purposes of this paper we will hypothesize that the light intensity recorded on the film, $I(x, y)$, is simply proportional to the local incident wave energy dissipation $\epsilon(x, y)$,

$$\langle I(x, y) \rangle \propto \langle \epsilon(x, y) \rangle \quad (1)$$

where the angled brackets indicate time-averaged. Since models of dissipation over a barred profile suggest a strong dependence of local dissipation on underlying morphology, dissipation may serve as a proxy measure of the nearshore topography.

We will approach the problem through the energy flux balance,

$$\frac{\partial}{\partial x} (Ec_g) = \frac{\partial}{\partial x} \left[\left(\frac{1}{8} \rho g H_{rms}^2 \right) c_g \right] = \langle \epsilon \rangle \quad (2)$$

where ρ is density, g is the acceleration due to gravity, E is the wave energy density, and c_g is the group velocity.

The simplest representation of waves shoaling on a beach assumes that the incident energy is narrow-banded and can be represented by a single frequency, f , and wave height, H_{rms} . Outside the surf zone, dissipation is through bottom friction. This is small compared to the dissipation due to surf zone breaking (Thornton and Guza, 1983) and provides no surface signal for imaging. Thus we take wave energy flux, Ec_g , to be conserved outside the breaker line. Inside the surf zone, wave height is assumed depth-

limited, similar to solitary wave theory (McCowan, 1891) or monochromatic lab results (Galvin and Eagleson, 1965) and supported by field tests (Thornton and Guza, 1982),

$$H_{\text{rms}}(x) = \gamma h(x) \quad , \quad x < x_b \quad (3)$$

where x_b is the position of the breaker line and h is the still water depth. Thus wave energy flux is strictly a function of depth, and local dissipation is simply determined from the flux gradient (equation 2). Dissipation over an arbitrary beach profile can easily be calculated using (2) and (3).

This monochromatic representation of the wave field, while simple, has several distinct disadvantages. First, if taken strictly, wave heights should actually increase as waves propagate from the bar crest into the deeper water of the trough. However, this non-physical result can be simply avoided if, as a wave is numerically shoaled, the criterion for whether it is breaking is based on a "local" wave height, calculated by inviscid shoaling from the point immediately offshore. The second problem with the monochromatic model (more severe for our application) is that the maximum dissipation will generally be at the initial breakpoint. This is, again, a non-physical result, as well as an unfortunate one for our technique since we are interested in using the intensity signal to determine the location of the bar crest, not the break point. However, this problem, which also occurs in the theory of longshore currents (Thornton and Guza, 1986), can be corrected by considering a random wave model where wave energy is considered composed of a distribution of waves with heights that are described statistically (Thornton and Guza, 1983). For the remainder of the paper we will focus on the random wave model.

Random Wave Model

Models for the shoaling and breaking of random wave fields have been published by a number of authors (Collins, 1970; Battjes, 1972; Kuo and Kuo, 1974; Goda, 1975;

Battjes and Janssen, 1978; Thornton and Guza, 1983). These models consider the wave energy to be composed of a distribution of waves of varying height. The analysis is then carried out statistically, representing the waves in terms of probability distributions whose bulk properties may be found by integration. Many of these models invoke depth-limited breaking to determine dissipation (equation 2). However, the latter two (Battjes and Janssen, 1978, and Thornton and Guza, 1983) specify dissipation and use (2) in the opposite direction to find wave height. We will follow the analysis of Thornton and Guza, 1983, hereafter TG83.

Using the extensive data set from the Nearshore Sediment Transport Study (NSTS), TG83 showed that the wave heights, H , of a random incident wave field were well described by a Rayleigh probability distribution,

$$p(H) = \frac{2H}{H_{rms}^2} \exp\left[-\left(\frac{H}{H_{rms}}\right)^2\right] \quad (4)$$

which is an implied function of local depth, and hence of cross-shore distance.

Surprisingly, this result was found to be valid throughout the entire nearshore region including the surf zone where the underlying assumptions of linearity are clearly violated. As the wave field shoals, some portion of the waves begin to break, modifying the distribution. The form of this modification is the main distinguishing feature of the above-listed random wave models. TG83 are unique in that their model for the shoaling of the wave height distribution is based on field data from a barred beach (Soldier's Beach, California) wherein the wave height time series were augmented with a record of which waves were actually breaking. They express the probability distribution of breaking waves, $p_b(H)$, as a weighting of the distribution of all waves,

$$p_b(H) = W(H) p(H) \quad (5)$$

where, from the data, they determine the best form of the weighting function to be

$$W(H) = \left(\frac{H_{rms}}{\gamma h} \right)^2 \left\{ 1 - \exp \left(- \left(\frac{H}{\gamma h} \right)^2 \right) \right\} \quad (6)$$

They then model the dissipation of a breaking wave based on a periodic bore model (Stoker, 1957; Hwang and Divoky, 1970),

$$\varepsilon = \frac{f}{4} \rho g \frac{(BH)^3}{h} \quad (7)$$

where B is an empirical breaker coefficient, roughly representing the fraction of the bore face that is covered with foam. The mean dissipation, $\langle \varepsilon \rangle$, is then the integral through the breaking wave height distribution,

$$\langle \varepsilon \rangle = \frac{3\sqrt{\pi}}{16} \rho g B^3 f \frac{H_{rms}^5}{\gamma^2 h^3} \left[1 - \frac{1}{\left(1 + \left(\frac{H_{rms}}{\gamma h} \right)^2 \right)^{5/2}} \right] \quad (8)$$

Application of the Model

Numerical implementation of the random wave model was carried out to determine the behavior of dissipation over various profiles, and to provide a comparison for field tests, to be discussed later in the paper. The energy flux balance, equation 2, forms the basis for the model. TG83 note that in testing a variety of numerical schemes, the simplest forward stepping technique was found to be sufficiently accurate. We will use this same algorithm,

$$Ec_g \Big|_2 = Ec_g \Big|_1 + \langle \epsilon \rangle \Big|_1 \Delta x \quad (9)$$

Starting from the deepest grid point (assuming a wave height that has been linearly shoaled from deep water), the wave energy flux is stepped landward. For the random wave model, the flux at any shoreward point, labelled 2, is calculated using the flux and dissipation (equation 8) found at the next seaward point, labelled 1. Note that the shallow water assumption is valid for all cases examined. Values used for B and γ are 1.54 and 0.42 respectively, taken as representative of field data (Thornton and Guza, 1983).

Examples

Theoretical dissipation profiles have been calculated for three beach profiles. The first, a plane beach, is the simplest beach profile and provides a good illustration of the behavior of wave dissipation over unperturbed topography. The second, Torrey Pines beach (the site of the NSTS results) was used first to check the model results against TG83 (an error check of the programming) and secondly to show the sensitivity of dissipation to minor perturbations in an otherwise simple profile. Finally, a barred profile from the SUPERDUCK experiment was used to show the ability of dissipation (and hence the time exposure technique) to highlight the bar crest location. The latter case was also used to provide an understanding of the ground truth studies, conducted during SUPERDUCK, that will be discussed later.

Figure 2 shows the behavior of the random wave model on a plane beach profile, shown in the top panel. The model shows a single broad dissipation maximum offshore, resulting from the distribution of wave heights with some dissipation arising offshore due to the more energetic waves while most waves break near a finite break point. There is a dissipation maximum (albeit broad) despite the fact that the beach profile is plane. The area under the curve must equal the deep water energy flux.

Figure 3 shows the model results for Torrey Pines beach on 10/20/78, during the NSTS experiment. This day was chosen as one of the two data runs analyzed in TG83 against which we could check the functioning of our model. Again, the beach profile is shown in the top panel, with associated H_{rms} and $\langle \epsilon \rangle$ curves for a random wave model shown in the lower panel. Since the distribution of dissipation is dependent on local water depth, peaks of dissipation will reflect positive changes of slope ("bumps" in the perturbation profile). The model indeed yields a well-defined dissipation peak over the large offshore bump located at $x=200$ m. Thus, it appears that the imaging of dissipation may prove useful in determining the horizontal length scales of perturbations (sand bars, terraces) in the bathymetry.

Figure 4 shows wave shoaling and dissipation for a barred beach profile (actually a linear storm bar which formed during the SUPERDUCK experiment). A second perturbation 375 m offshore is the residual of a semi-permanent second linear bar. Three features are apparent in the dissipation curves. Offshore, the presence of the second bar (perturbation) is indicated by the random wave curve by a small dissipation peak, shoreward of which dissipation is lower but not zero. This is similar to the results for the low-tide terrace on Torrey Pines Beach. The well-developed inner bar is clearly highlighted by the dissipation curve. However, the location of maximum dissipation is displaced seaward from the measured bar crest (location of minimum depth) by 20 m, a result of weighting the dissipation toward the larger waves. Continuing landward, the trough is indicated by a region of essentially zero dissipation. This contrast between the large dissipation over the bar and zero over the trough distinguishes (at least qualitatively) the signal due to sand bar morphology from that of a terrace or more minor perturbation. Finally, we see a narrow dissipation maximum near the shoreline, a feature that also shows up in the field tests discussed later. While the presence of this "shorebreak" maximum is reasonable, the details of its location may be poorly reproduced since our dissipation model

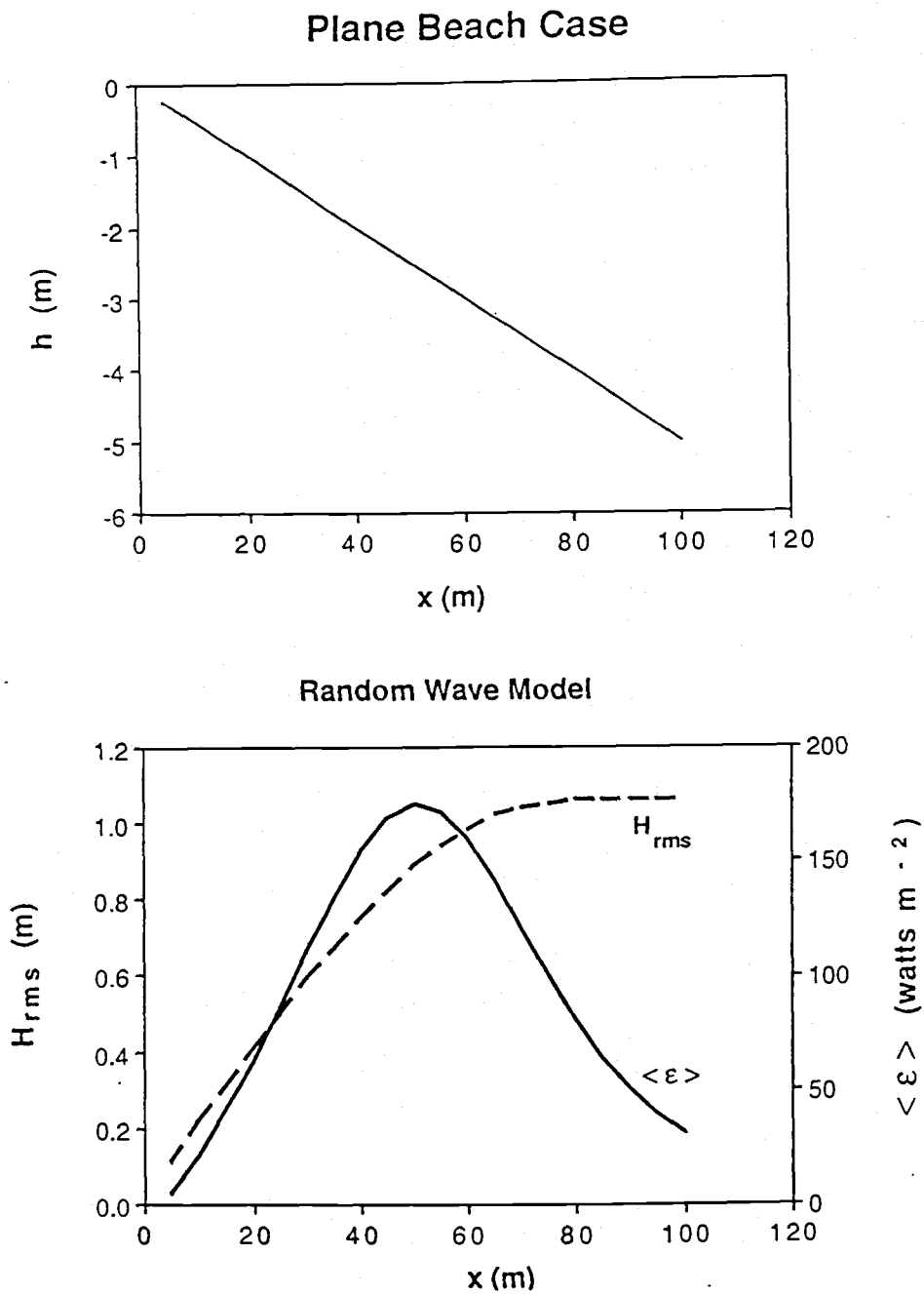


Figure I - 2. Model results as waves are shoaled over a plane beach profile (top panel). The behavior of H_{rms} and $\langle \epsilon \rangle$, plotted against offshore distance, is shown for the random wave model in the bottom panel.

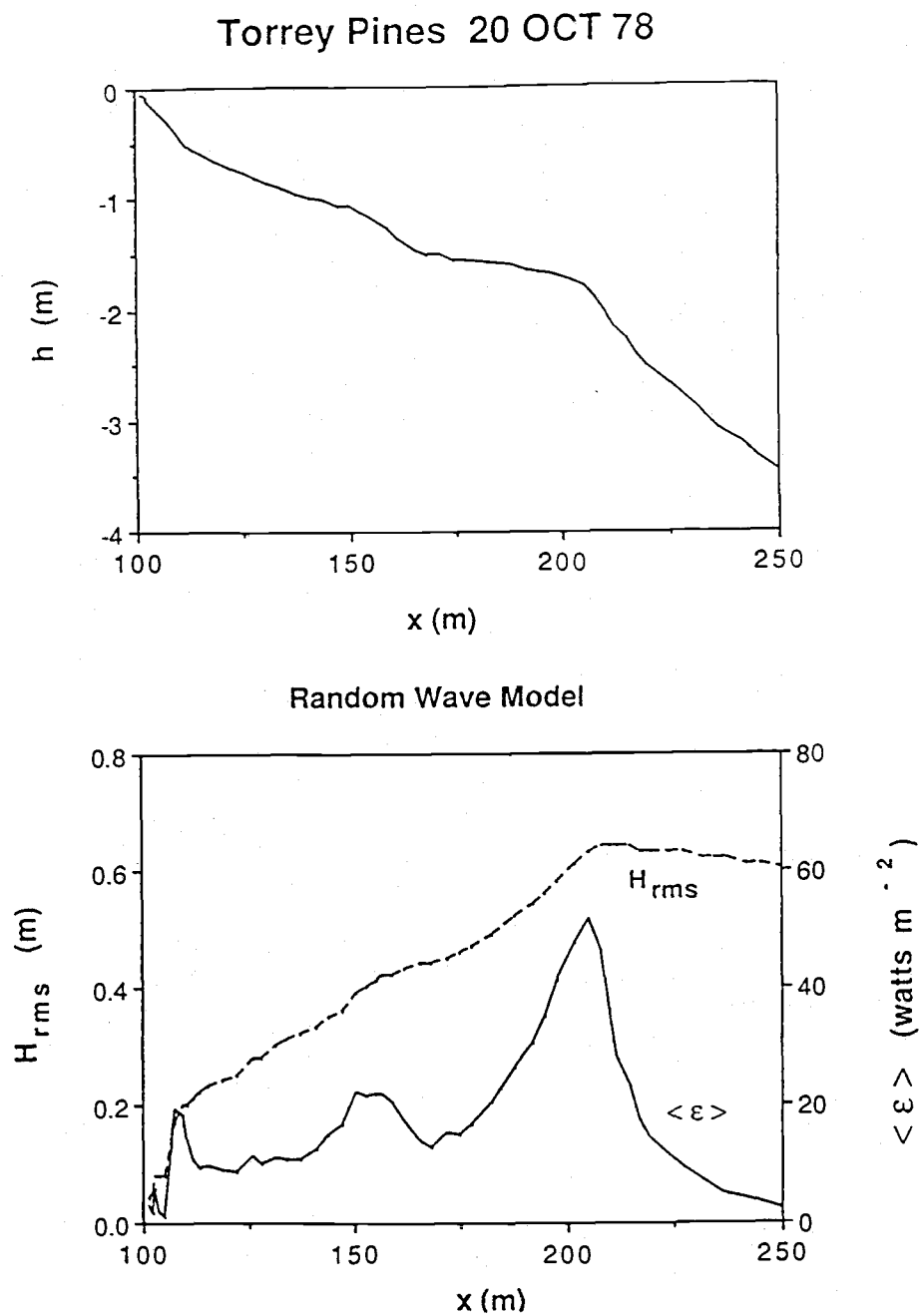


Figure I - 3. Model test results for wave shoaling and dissipation over a surveyed profile (top panel) from Torrey Pines beach on October 20, 1978. The cross-shore behavior of H_{rms} and $\langle \epsilon \rangle$ are shown for the random wave model in the lower panel.

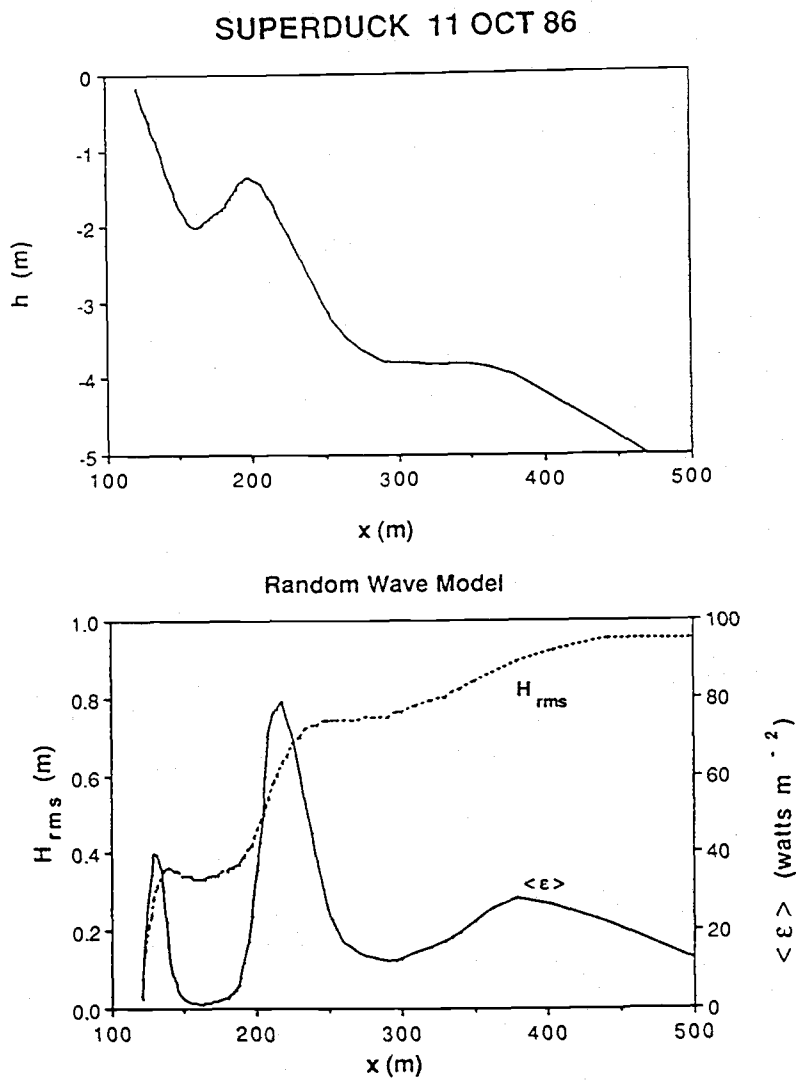


Figure I - 4. Model results for wave shoaling and dissipation over a barred beach profile (top panel) from SUPERDUCK on October 11, 1986. The cross-shore behavior of H_{rms} and $\langle \epsilon \rangle$ are shown for the random wave model in the lower panel.

artificially forces wave height to zero at the shoreline (we allow no standing wave component).

The influence of deep-water significant wave height, H_0 , on the random wave model is shown in Figure 5. For any offshore position, it appears that an increase in H_0 will result in an increase in local rms wave height, H_{rms} , up to a maximum value which depends on depth. Further increases in H_0 have no effect and the local wave field is said to saturate. This behavior shows the merging of the dissipation-based model of shoaling used here with earlier depth-limited models for depths that are "shallow" with respect to the wave height, a point that was also made theoretically in TG83.

Variation of wave period, T , will affect the model in two ways. The deep water energy flux (hence area under the dissipation curve) depends linearly on T . Also, the dissipation (equation 8) is inversely proportional to T . The net result is that dissipation profiles for different wave periods have different magnitudes but the same structure, including location and shape of peaks.

The saturation behavior of dissipation is beneficial to our objective of locating sand bar features since the location of the offshore dissipation maximum is only weakly sensitive to offshore wave parameters. This is quantified in Figure 6 which shows the fractional error in locating the bar crest (difference between the location of the offshore dissipation maximum and the measured bar crest position, Δx , divided by the offshore distance to the bar crest at mean tide, x_c) versus the non-dimensional wave height,

$$H_c^* = \left(\frac{H_0}{\gamma h_c} \right) \left(\frac{k_c}{2k_0} \right)^{\frac{1}{2}} \quad (10)$$

The variables h_c and k_c refer to the depth and local wavenumber at the bar crest, and k_0 is the deep-water wavenumber. H_c^* is derived by shoaling the deep water energy flux to the bar crest, if wave breaking were not allowed (note that the second term in equation 10 is the

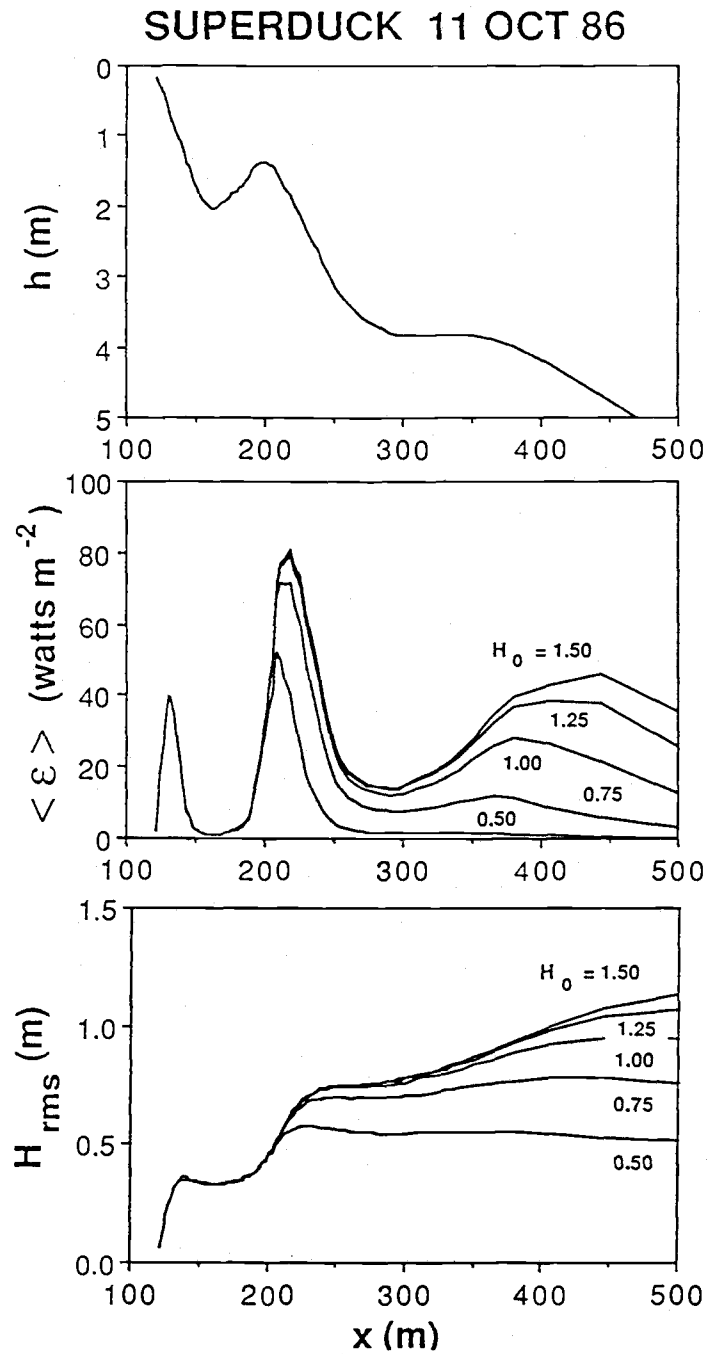


Figure I - 5. Influence of deep water rms wave height, H_0 , over a barred beach profile (top panel) from SUPERDUCK on October 11, 1986. The effect of increasing H_0 on dissipation, $\langle \epsilon \rangle$, and local wave height, H_{rms} , at offshore locations are shown in the middle and lower panels, respectively.

shoaling coefficient). Figure 6 shows that the fractional error in locating the bar crest varies from 0% for small waves that just break over the bar ($H_C^* = 0.5-1.0$) to about 35% for a saturated wave field.

The above analysis suggests that if the visible intensity signal recorded in time exposure photographs does depend on incident wave dissipation, then the time exposure technique should work. Best results will occur for waves which just break over the bar, but even for larger waves the error in bar location identification will reach a maximum value, 35% for the above case. If the results are to be used to test bar generation models based on standing wave motions, wherein the bar location, x_c , scales as

$$\chi_c \equiv \frac{\sigma^2 x_c}{g\beta} \quad (11)$$

where β is the effective beach slope and $\sigma = 2\pi f$ is the radian frequency, then errors of less than 18% will occur in the predicted frequency, f , of the standing wave. It should be noted that this value is just from one sample geometry and would be different for different beach profiles. For instance, the value of x_c does not enter into the dimensional error, Δx , so that for bars that are farther offshore the error would be smaller, and visa-versa. Similarly, for larger h_c (such as for higher tides), H_C^* would be smaller, and for higher tides x_c would be larger. Both would tend to yield smaller relative errors. Again, the opposite is also true, so that for lower tides and smaller h_c , estimates will tend to be worse.

Theoretical Error vs. Non-dimensional Wave Height

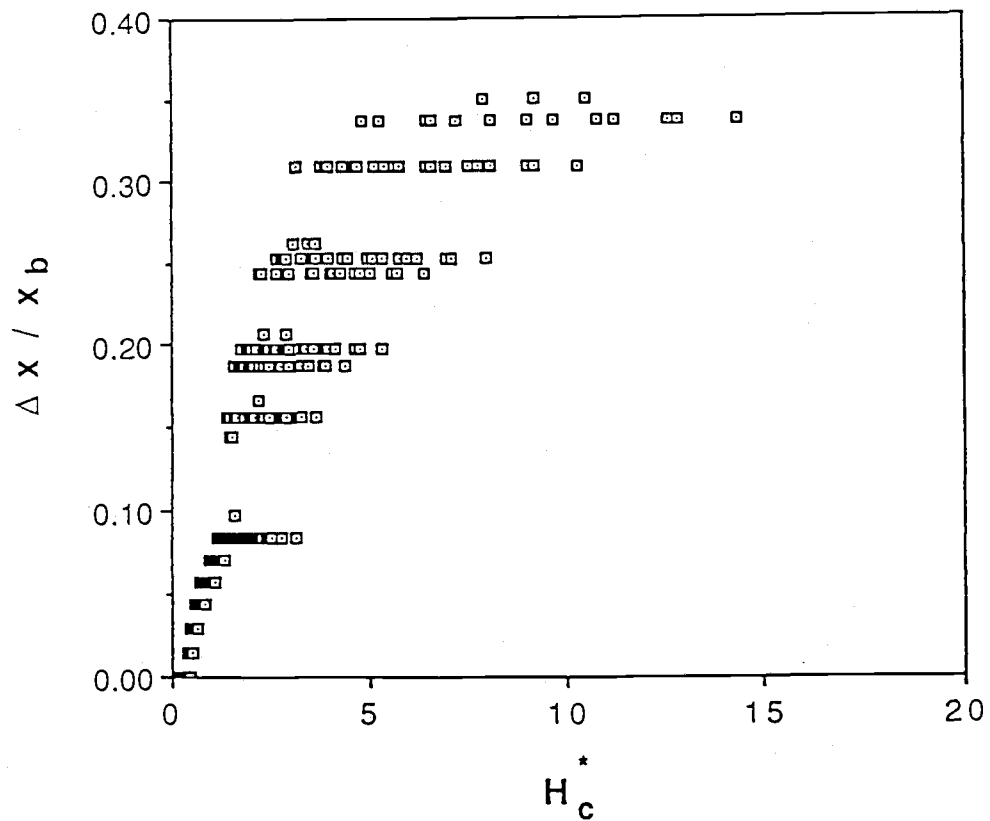


Figure I - 6. Fractional error in locating the bar crest from theoretical dissipation maxima plotted against non-dimensional wave height, H_c^* .

PHOTOGRAMMETRY

We wish to use oblique images to quantify the offshore and longshore length scales of the sand bar (and potentially other variables). Although photogrammetric equations for transforming images have been developed (e.g. Okamoto, 1982), the necessary equations will be derived here for completeness.

The location of any object in the image is a function of the spatial orientation of the camera in relation to ground topography, and can be determined by a simple analysis of the geometry. We will outline the equations that define the transformation between image coordinates and ground coordinates. When transforming from ground to image coordinates the equations are fully defined. However, since the image is two-dimensional while the ground is three-dimensional, the opposite process (called rectification) is underdetermined. This is overcome by assuming one dimension to be known. For example, in rectifying images of waves the vertical coordinate is assumed to be at sea level; errors of the order of the wave amplitude are assumed negligible compared to the height of the camera.

The geometry and labeling conventions used in the rectification process are shown in Figure 7. Image coordinates will be denoted with small letters, (x,y) , and ground coordinates will be denoted with capital letters, (X,Y) . The optic center of the camera is located at point O , a distance Z_c above the $x-y$ (ground) plane. The camera nadir line intersects the ground at the nadir, N . The image points lie in the focal plane, which for our purposes will be considered the 1:1 positive, consistent with traditional photogrammetry conventions. The focal plane is separated from O by the focal length, f_c , determined by the camera lens. The optic axis intersects the center of the focal plane at point p , called the principal point, and forms an angle τ (the camera tilt) with the vertical nadir line. The principal line passes through the principal point and bisects the focal plane. The principal point is also the origin for the image coordinate system with the principal line as the y -axis.

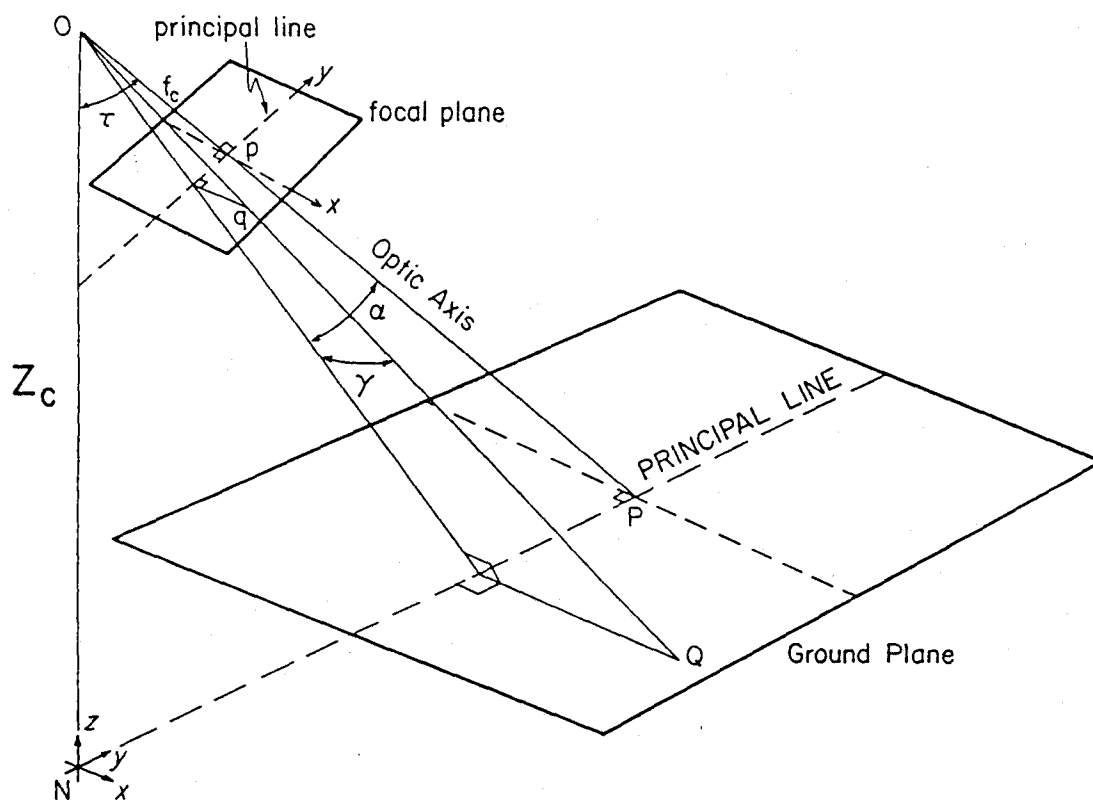


Figure I - 7. Geometry and labeling conventions used for photogrammetry.

The nadir point acts as the origin for the camera coordinate system with the principal line in the ground plane defining the positive Y-axis.

The ground location of any point, Q, is determined from its image coordinates (x_q, y_q) by

$$X_Q = Z_c \sec(\tau + \alpha) \tan \gamma$$

and (12)

$$Y_Q = Z_c \tan(\tau + \alpha)$$

where the angles α and γ are defined as

$$\alpha = \tan^{-1} \left(\frac{y_q}{f_c} \right)$$

and (13)

$$\gamma = \tan^{-1} \left(\frac{x_q}{\sqrt{y_q^2 + f_c^2}} \right)$$

Transformation in the opposite direction, from ground to image points, is done by simply inverting and combining (12) and (13) to yield

$$y_q = f_c \tan \left(\tan^{-1} \left(\frac{Y_Q}{Z_c} \right) - \tau \right)$$

and (14)

$$x_q = \left(\frac{y_q^2 + f_c^2}{Z_c^2 + Y_Q^2} \right)^{1/2} X_Q$$

Several complications arise in applying these relationships in the field. First, these equations are a function of the camera tilt and focal length. Field measurement of tilt may be awkward and inaccurate, and the focal length of a zoom lens may be hard to estimate. Second, we do not generally work from a 1:1 positive, but instead either read distances on a photographic enlargement or count picture elements (pixels) on a television screen. In doing so we will have altered the apparent focal length of the image by an unknown amount. We can solve for the "magnified" focal length analytically using

$$f'_c = \frac{x_e}{\tan\left(\frac{\delta}{2}\right)} \quad (15)$$

where x_e is the measured distance from the principal point to the right hand edge of the enlarged image, and δ is the horizontal field of view of the lens. Unfortunately, for most cases, δ itself is not accurately known. Third, the direction of aim of a camera in the field is generally chosen to give the best view. Thus, the ground coordinate system defined by the principal line may not be particularly convenient. The transformed ground points can be easily rotated into a more traditional coordinate system, for example with the x-axis directed offshore, if the angle, ϕ , between the two coordinate systems is known. Unfortunately, accurate estimation of ϕ in the field is again difficult.

The unknowns, f'_c , τ , and ϕ , can be determined quite accurately by making use of targets at known locations in the image. By knowing both the ground and image coordinates of particular points, equations (12), (13) and (14) can be solved iteratively to calculate the unknowns. If one known point and the horizon are used, the solution will be unique. If two or more known points are used, the problem is over-determined and can be solved by minimizing an appropriate error term. Using this technique in analyzing the images discussed later in the paper, we find typical errors in the estimates of τ , ϕ and f'_c to

be less than 0.25° , 0.5° , and 0.5% respectively, roughly consistent with theoretical expectations discussed below.

THEORETICAL RESOLUTION AND ACCURACY

The photogrammetric measurements outlined in the last section are based on estimates of one distance (the camera height) and two angles (vertical and azimuthal). The precision of the technique then relies on the precision of each of these estimates.

While there may be errors associated with estimating camera height above some surface, there is no inherent limitation on that measurement. On the contrary, there is a discrete resolution associated with our estimates of angle. For image quantification we use an image processing system (described later) which breaks the image into a 512 x 512 array of pixels. Since we can resolve to no better than $\pm 1/2$ pixel, we find a fundamental limit on angular resolution to be $\Delta\alpha = \Delta\gamma = \delta/1024$ (assuming $\tan \delta/2 \approx \delta/2$). For our typical wide angle lens, $\delta = 40^\circ$, so $\Delta\alpha = 0.04^\circ = 7 \times 10^{-4}$ radians.

From equation (12) we see that the precision of estimates in Y_Q is given by

$$\frac{\Delta Y_Q}{Y_Q} = \frac{\Delta H_c}{H_c} + \frac{2\Delta(\tau+\alpha)}{\sin 2(\tau+\alpha)} \approx \frac{2\Delta(\tau+\alpha)}{\sin 2(\tau+\alpha)} \approx \frac{1.4 \times 10^{-3}}{\sin 2(\tau+\alpha)} \quad (16)$$

Sensibly, resolution degrades as $(\tau + \alpha)$ approaches $\pi/2$, or as the point of view approaches the horizon. If we take the maximum useful vertical angle to be 85° (5° from the horizon), the resolution in Y will be 0.8%. Note that the fractional errors also increase as the view approaches nadir. However, this is simply a result of normalizing by Y_Q , which goes to zero at the nadir; absolute errors will actually be a minimum.

The error in X estimates (normalized by Y_Q , roughly representing the distance from the camera) is given by

$$\frac{\Delta X_Q}{Y_Q} = \left(\frac{\Delta H_c}{H_c} \right) \frac{\tan \gamma}{\sin(\tau + \alpha)} + \frac{\tan \gamma \Delta(\tau + \alpha)}{\cos(\tau + \alpha)} + \frac{1}{\sin(\tau + \alpha)} \frac{\Delta \gamma}{\cos^2 \gamma} \quad (17)$$

For typical camera views, $\sin(\tau + \alpha) \approx 1$, hence the theoretical resolution is again limited by angular resolution through the last two terms. Using representative values, we find a worst case resolution of 0.3%, a smaller value than for Y , partly due to the choice of normalization. Since the camera coordinate system is not usually aligned with the survey system, we chose a conservative estimate that spatial resolution in either axis will be on the order of 0.8% of the distance from the camera.

While fundamental limits on precision depend, for our system, simply on the angular size of the pixels, the absolute accuracy of our measurement depends on cumulative errors from a number of estimates. If the location of the camera is well known, the error in the first term of (16) and (17) results largely from errors in determining sea level (assuming that the ocean surface is being imaged). For the data discussed later, this will be on the order ± 0.25 m with a camera height of 40 m, so that the relative error contribution is 0.65%. This error could be substantially larger for lower camera heights. Estimation of the vertical and horizontal angles actually incorporates parameters such as τ , f and ϕ , each of which has associated errors. If we assume that the parameters themselves were estimated based on the location of two known points (as outlined in the previous discussion), then they will collectively incorporate the error of four separate angle measures, $4\Delta\alpha$. Including the error associated with estimating the angle of interest, the total angular error could be $5\Delta\alpha = 0.20^\circ = 3.5 \times 10^{-3}$ radians. For a maximum vertical angle of 85° , and including the error for camera height, the theoretical worst case accuracy should be

$$\frac{\Delta X_Q}{Y_Q} < \frac{\Delta Y_Q}{Y_Q} \approx 0.65\% + (5 * 0.8\%) < 5\% \quad (18)$$

As shown, the accuracy and resolution of the system depend on the angular field of view, δ , and the vertical angle, $(\tau + \alpha)$. The value of δ used here is for a wide angle lens

and gives a worst case result. Clearly, a telephoto lens, zoomed in on the subject at hand, will yield improved estimates. The vertical angle becomes critical as $(\tau + \alpha)$ approaches the horizon. While 85° is a reasonable value for a maximum angle, a better approach to experimental design would be to determine the required resolution and camera geometry, then solve for the maximum vertical angle for which this resolution is achievable.

FIELD TECHNIQUES

The time exposure technique for estimating the incident wave dissipation distribution and hence large scale nearshore morphology was tested as part of the DUCK85 and SUPERDUCK experiments in September 1985 and October 1986, respectively, at the Army Corps of Engineers Field Research Facility (FRF) in Duck, N.C. The DUCK85 experiment (Mason, et al., 1987) was used to perform initial testing primarily with standard 35 mm cameras and simple photographic time exposure techniques. The images acquired were projected onto an x-y digitizer table and the location of the intensity maximum determined visually (Holman and Lippmann, 1987). Results from that experiment were encouraging, but indicated a need for further quantification and for more sophisticated digitization methods.

During SUPERDUCK the use of video imagery was implemented as an improvement to the photographic technique. A Panasonic black-and-white television camera was mounted on top of a 40 m high tower erected on the dune crest. Figure 8 is a map of the field site during the October portion of the SUPERDUCK experiment showing the location of the study area, referred to as the minigrid, in relation to the FRF tower and the ground coverage associated with the camera.

Hourly video records of twenty minute length were acquired from October 6-16. Time exposures were created digitally by mathematically averaging successive video frames over a ten minute period using an Imaging Technology image processing system in a DEC LSI 11/73 host computer (Figure 1b is an example time exposure image from October 10). Using the photogrammetry results the time exposure image can be rectified to produce a map view with known scaling. The rectification process involves mapping the oblique image intensities, pixel by pixel, onto the scaled grid. From the rectified view, cross-shore intensity profiles at prescribed longshore distances are easily found. Figure 9 is the

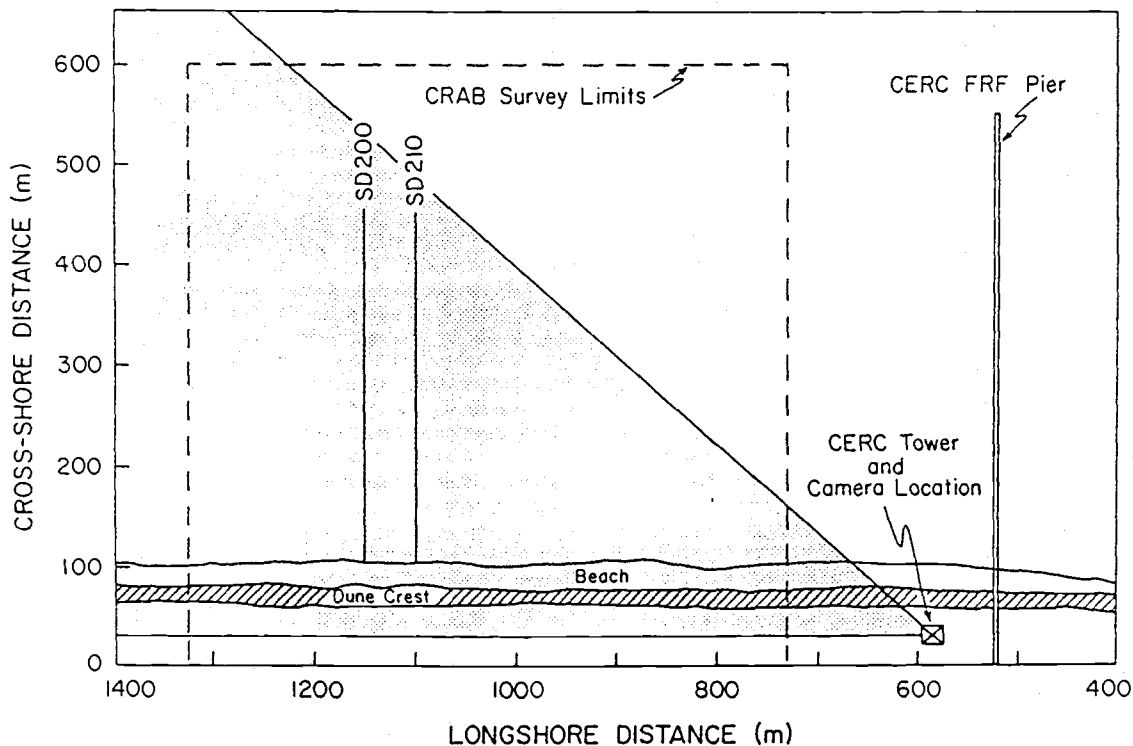


Figure I - 8. Map of the field site during the October portion of SUPERDUCK. The stippled area indicates the ground coverage in the field of view of the camera. Cross-shore transect SD200 is the location of some example profiles in the text while SD210 is the location closest to the main instrument line in SUPERDUCK. Longshore spacing for the CRAB survey lines was 20 m (there exists an intermediate line, SD205, between the two lines indicated).

rectified image of the minigrid area outlined in Figure 1b. Figure 10 shows an example cross-shore intensity profile and the local bathymetry. Clearly, there are local maxima in the intensity distribution in the vicinity of the shoreline and the bar, which appear very similar to the model results presented earlier (Figure 4). Note that only relative magnitudes of intensity are relevant within an image; absolute magnitudes vary with ambient light and camera aperture.

Quantification of images is accomplished using an image processing system. Extracting information with this system is objective and allows for minimum handling of raw data. Furthermore, with the aid of the image processor we may digitally enhance the images to best reveal the information available. For example, though some video records do not yield high contrast raw images, the image processor allows us to increase the dynamic range of the image by stretching the contrast to as many as 256 gray shades.

Ground truth bathymetry data during SUPERDUCK were collected by the FRF staff using the CERC Coastal Research Amphibious Buggy, or CRAB (Birkemeier and Mason, 1984). Figure 8 shows the location of the intensive survey region referred to as the minigrid. The bathymetry was sampled once per day (October 6, 9-16) along preset cross-shore profile lines spaced approximately 20 m apart alongshore. Each survey went beyond the first (and most prominent) sand bar, with the exception of the 10th when adverse conditions prevented survey completion. Figure 11 shows three-dimensional oblique views of the minigrid survey for October 6, 9, 11, 13, 15, and 16 (Birkemeier, et al., 1988).

A maximum of twenty shore-normal image intensity profiles within the minigrid area were analyzed for each data run. As in Figure 10, each profile contained a maximum intensity (or peak) in the vicinity of the shoreline and the bar, provided the waves were breaking offshore. Given the large amount of data, 464 cross-shore comparisons, not all the profile plots are included. Instead most of the data is summarized in the following

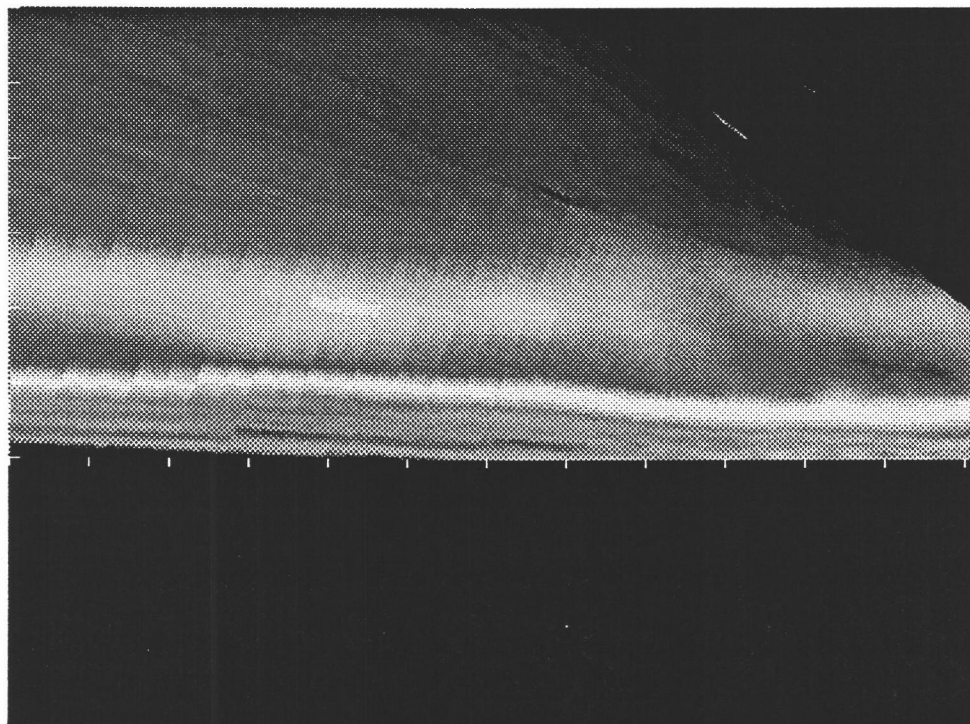


Figure I - 9. Rectified time exposure image obtained at low tide on October 16, 1986 encompassing the minigrad. The longshore and cross-shore distances are scaled equally with ticmark spacing of 50m. The thin white band indicates the shore break while the broader offshore band shows breaking over the bar. The relative size in raster width reflects the pixel resolution in the original time exposure.

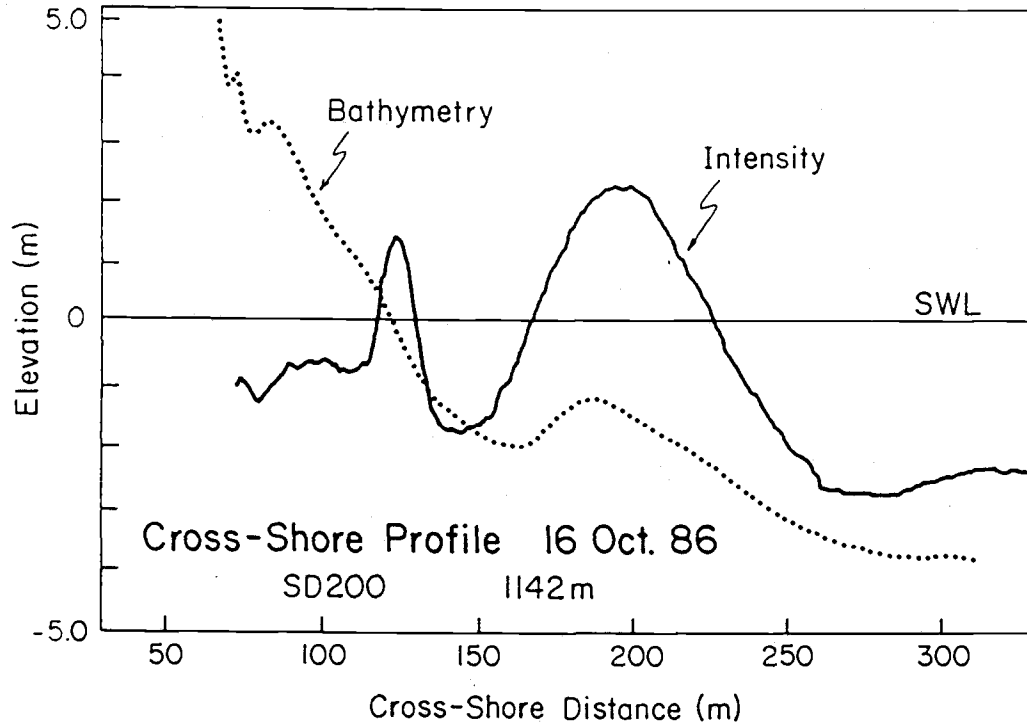


Figure I - 10. Example cross-shore intensity profile and bathymetry for October 16, 1986 during SUPERDUCK. The intensity values are non-dimensional with absolute magnitudes that are not related to the bathymetry.

SUPERDUCK BATHYMETRY

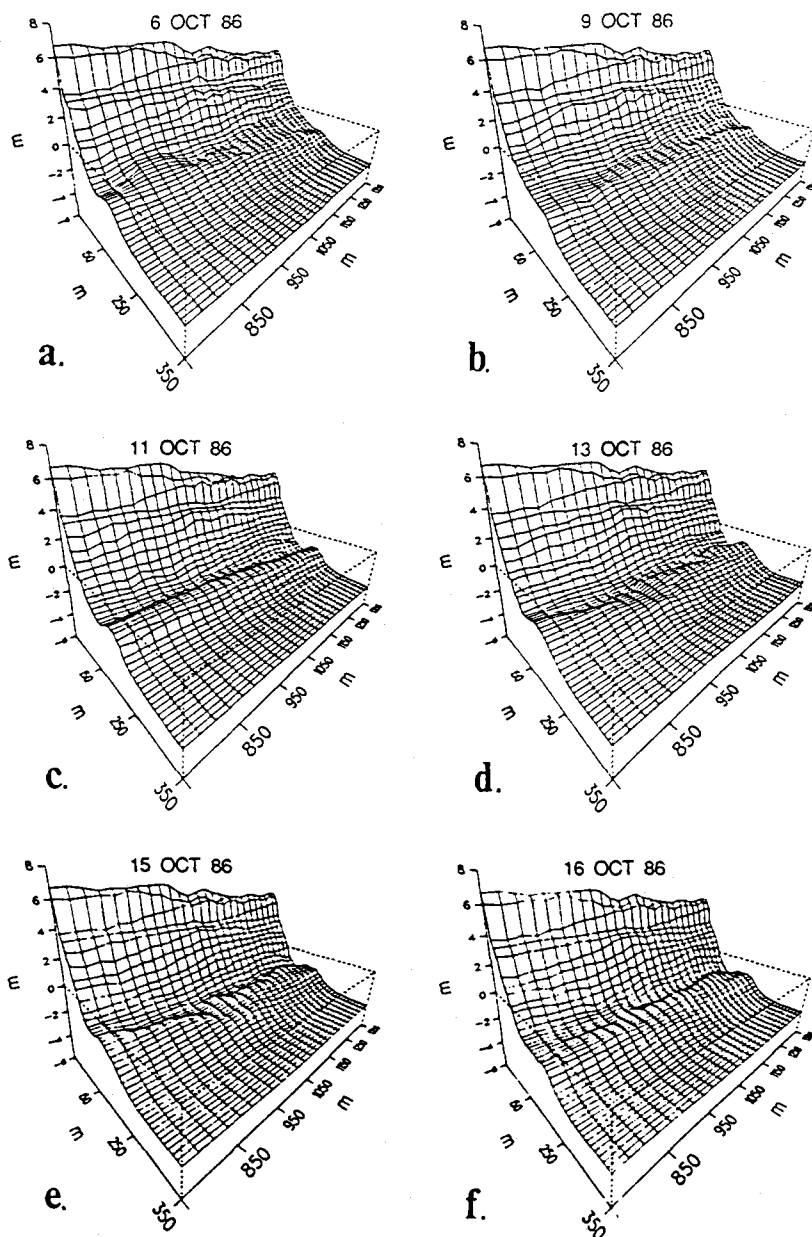


Figure I - 11. Three-dimensional oblique views of the minigrid survey during SUPERDUCK. (Courtesy Bill Birkemeier and the FRF).

analysis using two-dimensional plan-view maps indicating the surveyed bar location and digitized intensity maximum location at different stages of the tide. With this sampling scheme we are able to determine the behavior of the cross-shore intensity distribution in relation to the bathymetry under varying wave conditions, water levels, and beach state. Table 1 summarizes the sampling times, wave conditions, and video quality for each data run.

Table I - 1. Sampling time, wave conditions and video quality for morphology images discussed in the text.

Date	Tide (m)	Time	H_{rms} (m)	f (Hz)	Video Quality
06	low -0.11	1400 EST	0.82	0.1680	good
06	mid 0.25	1730 EST	0.56	0.1719	good
09	high 0.80	1130 EST	0.43	0.1641	good
09	mid 0.27	1445 EST	0.44	0.1641	good
09	low -0.27	1800 EST	0.38	0.1641	good
10	low -0.08	0600 EST	0.33	0.2656	good
10	mid 0.55	0915 EST	1.35	0.1484	poor (rain)
10	high 1.10	1230 EST	1.58	0.1406	poor (rain)
11	low 0.09	0720 EST	2.06	0.1094	good
11	mid 0.56	1040 EST	2.13	0.1563	good
11	high 1.06	1400 EST	2.06	0.1016	good
12	low 0.03	0830 EST	1.65	0.0938	excellent
12	mid 0.45	1145 EST	1.85	0.0859	excellent
12	high 0.93	1500 EST	1.77	0.0859	excellent
13	low -0.22	1000 EST	1.20	0.0820	good
13	mid 0.15	1230 EST	1.25	0.0977	good
13	high 0.73	1600 EST	1.25	0.0977	good
14	low -0.36	1100 EST	0.75	0.0977	poor (noisy)
14	mid 0.17	1400 EST	0.69	0.1055	poor (noisy)
14	high 0.70	1700 EST	0.61	0.0938	poor (noisy)
15	low -0.22	1130 EST	0.77	0.1719	good
15	mid 0.30	1445 EST	0.64	0.1719	good
15	high 0.76	1800 EST	0.54	0.1641	good
16	high 0.91	0600 EST	0.49	0.2349	good
16	mid 0.40	0915 EST	0.68	0.1992	good
16	low -0.30	1230 EST	0.72	0.2031	good

RESULTS

Time Exposures

The research objectives of the time exposure technique are threefold. The first is to infer the presence of a sand bar from an offshore intensity maximum corresponding to the maximum time-averaged incident wave dissipation. The second is to determine the cross-shore length scale of the bar from the location of the intensity maximum. The third is to detect the presence of any longshore variability in the bar and determine appropriate longshore length scales. We will examine each objective in turn.

The theoretical dissipation model suggests that best results will be obtained for small waves that just break over the bar (H_C^* values of 0.5 to 1.0). For October 6th an average value of H_C^* was approximately 0.85, and, while the bathymetry was complex, there were local regions of good bar definition (Figure 11a). Figure 12 shows the mid-tide intensity transects for the three best-defined sand bar profiles (determined from minigridd bathymetry). The intensity maxima clearly indicate the presence of the sand bar although the peak definition is somewhat subtle for the $y=1187$ transect, consistent with the subtle nature of the bar. There is excellent agreement between the locations of the intensity maxima and bar crest, well within the resolution of the image. This supports the validity of the model and the potential of the technique for imaging morphology under optimal conditions.

Figure 13 is the rectified time exposure image obtained at low tide on the 11th, a day when model performance was expected to be poorer due to the larger wave heights (average $H_C^* \approx 4.3, 2.6,$ and 2.4 for low, mid and high tide, respectively). The bathymetric survey (Figure 10c) showed the bar to be linear with no longshore variability. The intensity distribution in Figure 13 confirms this, showing a clearly linear pattern and providing a good qualitative description of the sand bar.

Simple Time Exposure 6 OCT 86

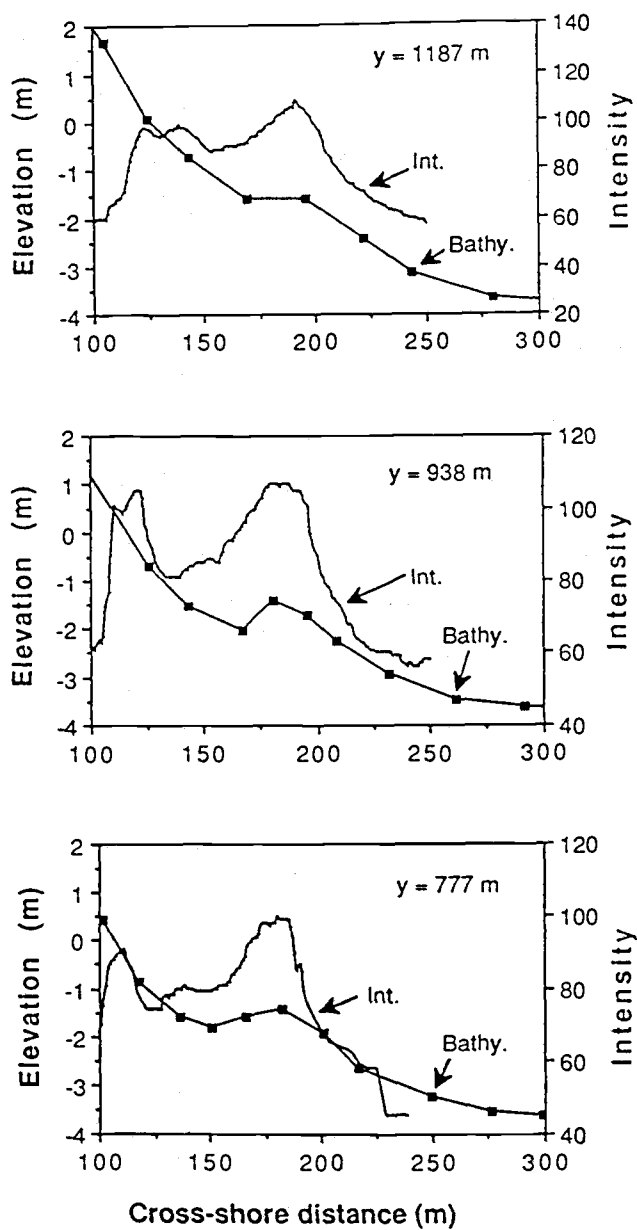


Figure I - 12. Local bathymetry and cross-shore intensity profiles from a simple time exposure obtained at mid tide on October 6, 1986. The three transects were chosen as having the best-defined bars.

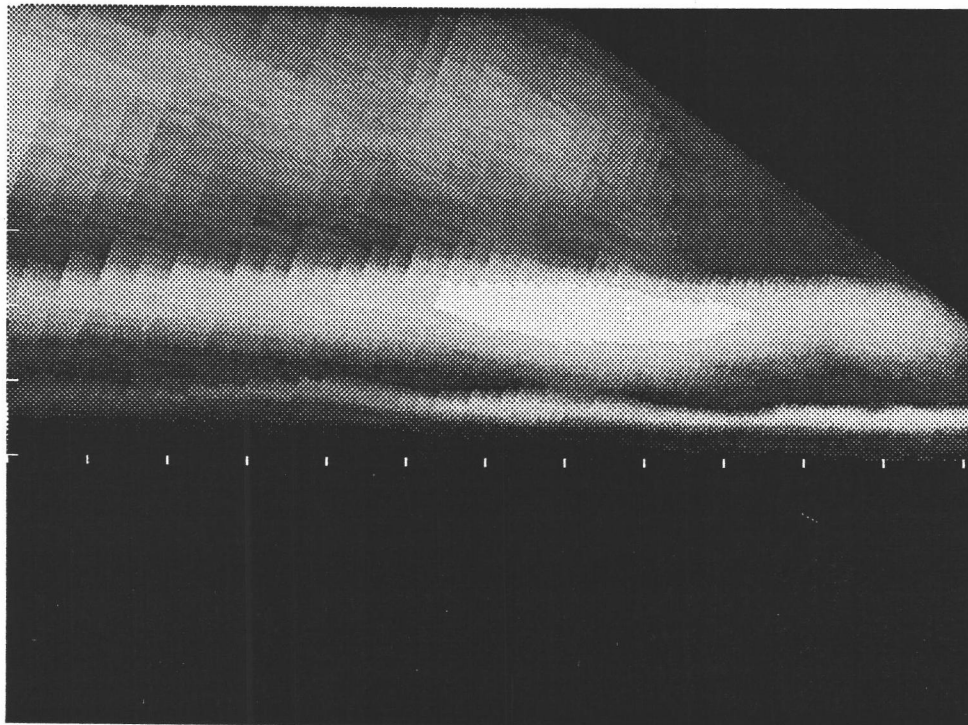


Figure I - 13. Rectified time exposure image encompassing the minigrad area obtained at low tide on October 11, 1986. The longshore and cross-shore distances are scaled equally with tickmark spacing of 50m. The thin white band indicates the shore break while the broader offshore band shows breaking over the bar. The relative size in raster width reflects the pixel resolution in the original time exposure.

While the qualitative description is good, the quantitative behavior of the technique breaks down in an unexpected way. Figure 14 shows the location of the intensity peak for low, mid, and high tide over the minigrid area. Also shown are the locations of the mean shoreline and bar crest. The latter is depicted by a central line (the best estimate of bar crest position) surrounded by a stippled area, reflecting the fact that the bar itself may not be well defined. (From Figures 12 and 17, it is clear that bar definition is typically based on three CRAB survey points with a typical spacing of 15 m and whose locations are subject to operator subjectivity. To parameterize this uncertainty we have added the stippled area whose bounds correspond to a deepening by 5% of the bar crest depth, h_c , usually 5-10 cm.)

The shape and trend of the bar in Figure 14 appears to be preserved at all stages of the tide. However, the offshore location of the intensity peaks does not fall over the bar, and in fact lies inside the crest well into the trough. This result cannot be reproduced in any way by our model and shows that our assumption that the average visual wave breaking signal represents incident wave dissipation is invalid under these conditions.

Investigation of the original video images reveals two apparent sources for the error. The finite distance required for wave reformation after passing the bar crest appears to provide a minor landward offset. Most of the error appears to stem from preferential persistence of foam in the trough region. This differential in foam persistence weights the intensity maximum shoreward from the location of maximum wave dissipation. We know of no testable physics to describe this behavior and hence allow us to remove the bias. By examining those records for which a well-defined bar is present, we find that approximately 42% of the intensity maxima were located shoreward of bar crest and that these were generally associated with high waves and strong onshore winds. This latter observation suggests a potential mechanism which would need considerable further testing, though it should be noted that moderate-to-strong onshore winds could blow spray from

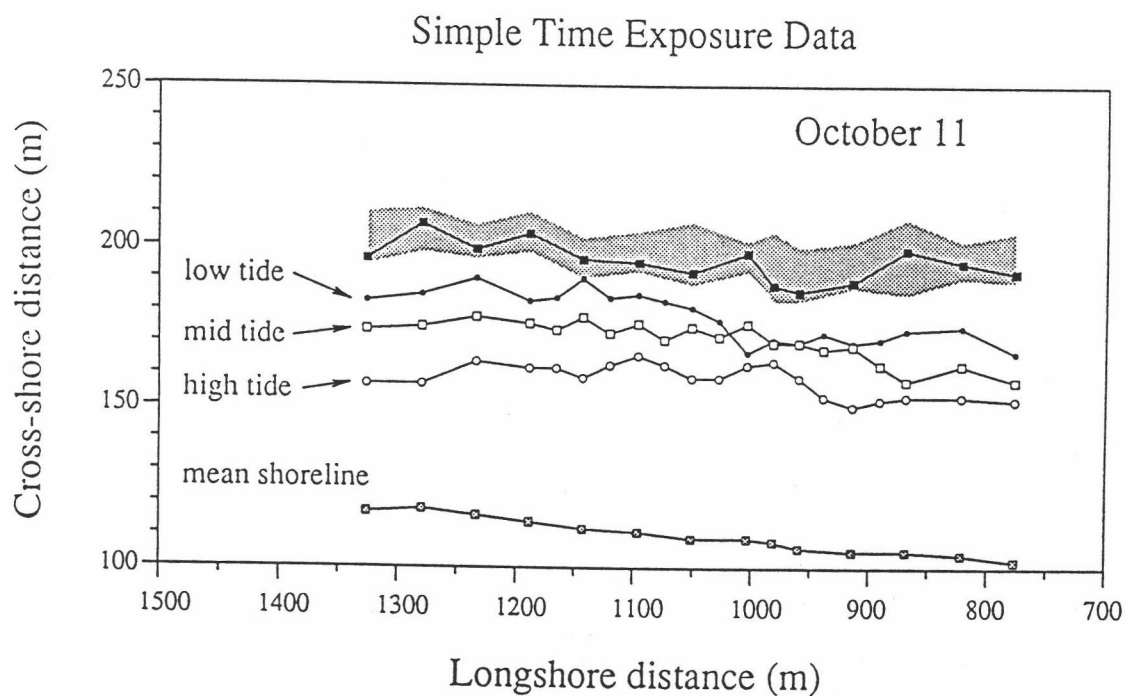


Figure I - 14. Location of the mean shoreline, measured bar crest (solid squares), and intensity maxima from simple time exposures obtained at low, mid, and high tide on October 11, 1986. The stippled area indicates the area around the crest for which the water depth is within 5% of h_c .

the active wave breaking regions (especially for plunging breakers) shoreward to cause an inshore bias in the maximum intensity location. In addition, high winds could cause whitecaps in regions of little or no incident wave breaking, also biasing the intensity distribution.

The capabilities of the technique for detecting and quantifying longshore variability are illustrated in Figure 15, a comparison of shore-parallel transects of intensity and bathymetry for October 16th, a day of lower waves ($H_C^* \approx 1.7$). The two transects differ by 10 m in offshore location and are centered about the mean bar position. The intensity and bathymetry profiles for this day and for all others tested from SUPERDUCK showed similar structure. The presence of dips in the shore-parallel bathymetry (caused possibly by topographically-trapped rip currents), originally a concern, does not appear to cause a problem since the relative "darkness" above the deeper channel is imaged in a consistent manner with the "darkness" due to reduced breaking in the same region. Several other examples of rhythmic morphology from other times of year confirm the robustness of the technique for this purpose, indicating that the time exposures can in fact be used to detect and measure dominant longshore length scales of a sand bar system (Holman and Sallenger, 1986).

Overall, the time exposure technique appears to be a very useful tool for determining the presence of a bar system as well as the presence and length scales of longshore variability. Cross-shore scales are well reproduced under certain conditions, but an observer hoping to use photographic time exposures, for example, would have to bear in mind the potential foam bias and make a qualitative assessment of the problem before quantifying any sample (residual foam is visible, so at least an assessment can be made). This problem seems to reduce the effectiveness of the time exposures. However, if an image processing system is available, more powerful techniques are available to improve

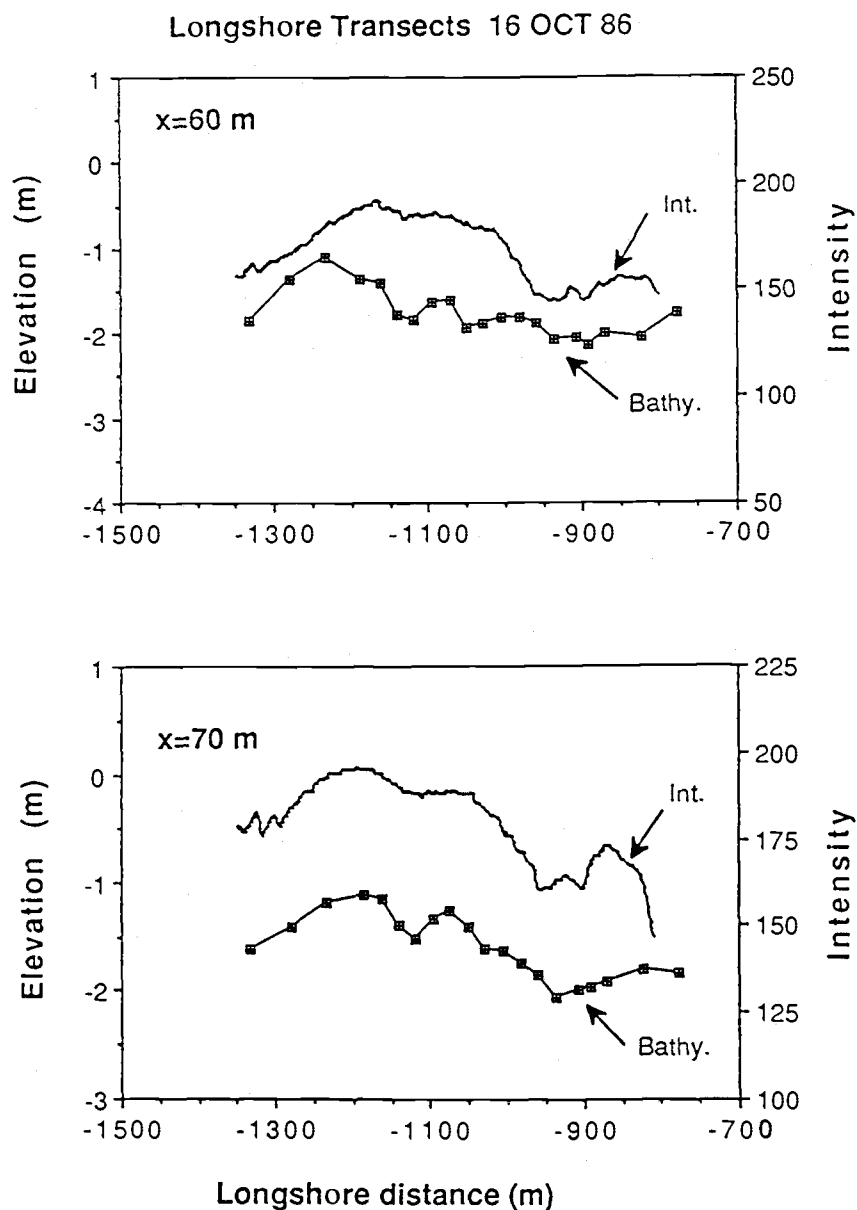


Figure I - 15. Shore-parallel transects centered over the mean bar distance, 60 m (upper panel) and 70 m (lower panel) offshore, from a simple time exposure obtained at low tide on October 16, 1986. Variations of intensity correspond to the underlying bathymetry.

the situation. We have developed a modification to the technique, called differencing time exposure, that eliminates this problem.

Differencing Time Exposures

One way to altogether avoid the dynamics of residual foam accumulation is to eliminate unwanted, persistent signals that do not pertain to active breaking (thus energy dissipation). This elimination can be accomplished by subtracting video frames, separated in time by a given interval (commonly 0.5 - 1.0 seconds), to yield a difference image. Regions of little or no contrast change, such as areas of persistent foam, will show zero difference. Areas of active breaking will show large intensity changes, hence large difference signals. A time exposure can be made by averaging a set of these difference images over a suitable period, again ten minutes for our case. Figure 16 is an example differencing time exposure image from October 11. The offshore breaking pattern is indicated again by the high intensity band offshore.

The differencing technique requires the selection of two free parameters to yield an optimal image. The first is the time interval between images to be subtracted. The second is a threshold value below which contrast differences are considered negligible (and are mapped to zero). This threshold serves the double purpose of eliminating minor values of difference that result from camera shake or the inevitable video noise, as well as eliminating the negative values of difference (since time averaging allowing both positive and negative differences must always be zero). While resulting image quality is influenced by the particular values of these parameters, the conclusions about sand bar morphology (intensity peak locations) are not overly sensitive. Fixed values have been used throughout this paper to eliminate selective bias.

We start our examination of the differencing time exposure technique by again looking at the limiting case where waves just begin to break over well-defined bar crests.

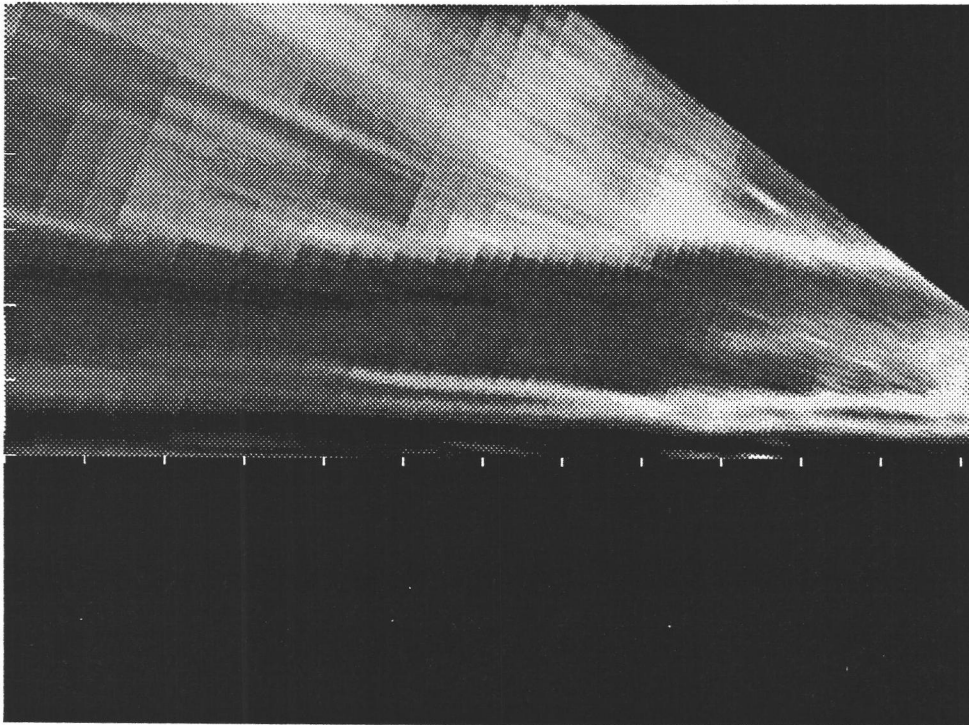


Figure I - 16. Rectified differencing time exposure obtained at low tide on October 12, 1986. The bright white band offshore indicates the presence of a sand bar, whereas the shoreline is indicated by a relative darkness within the shorebreak region. The longshore and cross-shore distances are scaled equally with ticmark spacing of 50m.

Figure 17 is a bar location map for October 9th indicating the estimated bar location and intensity maxima at low ($H_C^* = 0.8$) and mid tide ($H_C^* = 0.6$) for the differencing algorithm ($H_C^* = 0.45$ at high tide and no waves were breaking offshore). At mid tide the intensity maximum location falls within the survey error of the position of the bar crest, indicating a good estimate at all longshore locations. Cross-shore profiles corresponding to several regions with well-defined bar crests (indicated in Figure 17) are shown in Figure 18. Not surprisingly the offshore intensity maximum shows excellent agreement with the bar crest location. Furthermore, the intensity maximum has moved offshore at lower water level, consistent with the results of the dissipation model (Figure 6; equation 10).

Figure 19 shows the results of the differencing technique for October 11 when the bar was linear but the simple time exposure results were their worst. The improvement is immediately evident; at high tide ($H_C^* = 2.4$) the intensity locations lie quite near the crest within the range of bar estimate for most of the data. At lower tide levels the intensity moved offshore consistent with greater dissipation offshore. For low tide ($H_C^* = 4.3$) the mean value of $\Delta x/x_C \approx 39\%$, somewhat above the same range for the model calculations (Figure 6) but not unreasonable.

Figure 20 shows the performance of the technique for October 16th when the bathymetry was quite variable in the longshore. At high tide ($H_C^* \approx 0.4$), the waves were barely breaking over the bar and the intensity maximum provided an excellent mapping of even this complicated bar morphology. However, for low tide ($H_C^* \approx 1.7$), the differencing time exposure maximum is further offshore and corresponds to the location of the more continuous slope break at about 1.75 m depth. The H_C^* value for the slope break was approximately 1.0, large enough to allow significant breaking there. This may explain the "selection" by the technique of the straighter slope break instead of the complicated and more poorly defined bar crest.

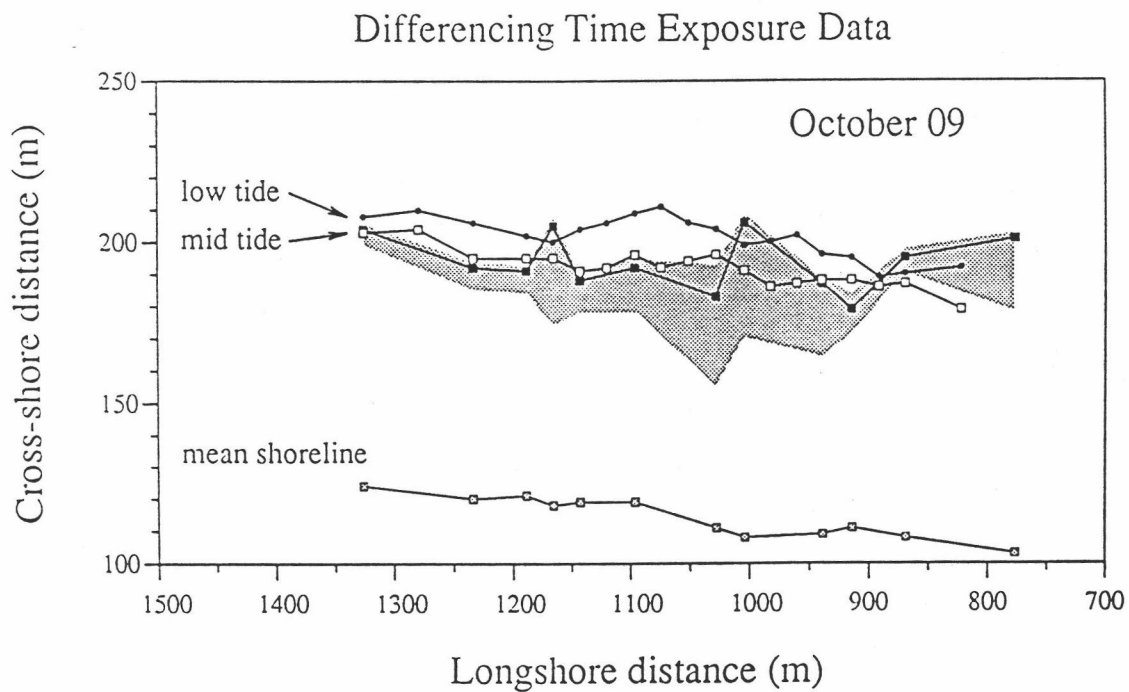


Figure I - 17. Location of mean shoreline, measured bar crest (solid squares), and intensity maxima from differenced time exposures obtained at low and mid tide on October 9, 1986. The stippled area indicates the area around the crest for which the water depth is within 5% of h_c .

Differencing Time Exposure 09 OCT 86

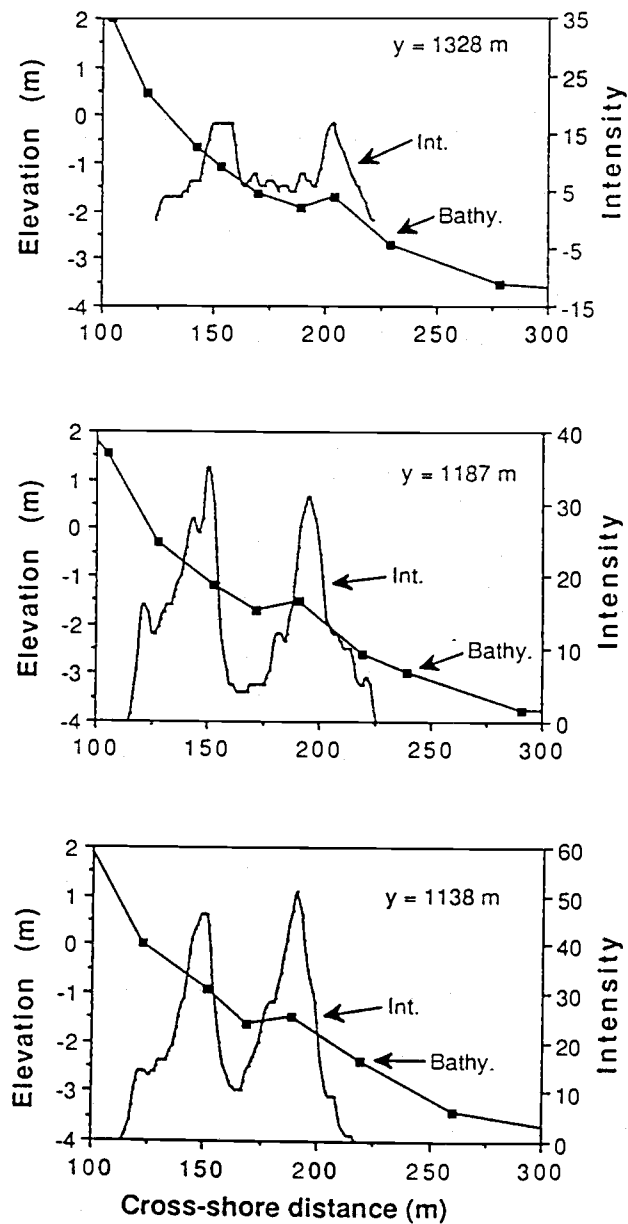


Figure I - 18. Local bathymetry and cross-shore intensity profiles from a differenced time exposure obtained at mid tide on October 9, 1986 for the three best-defined sand bar locations.

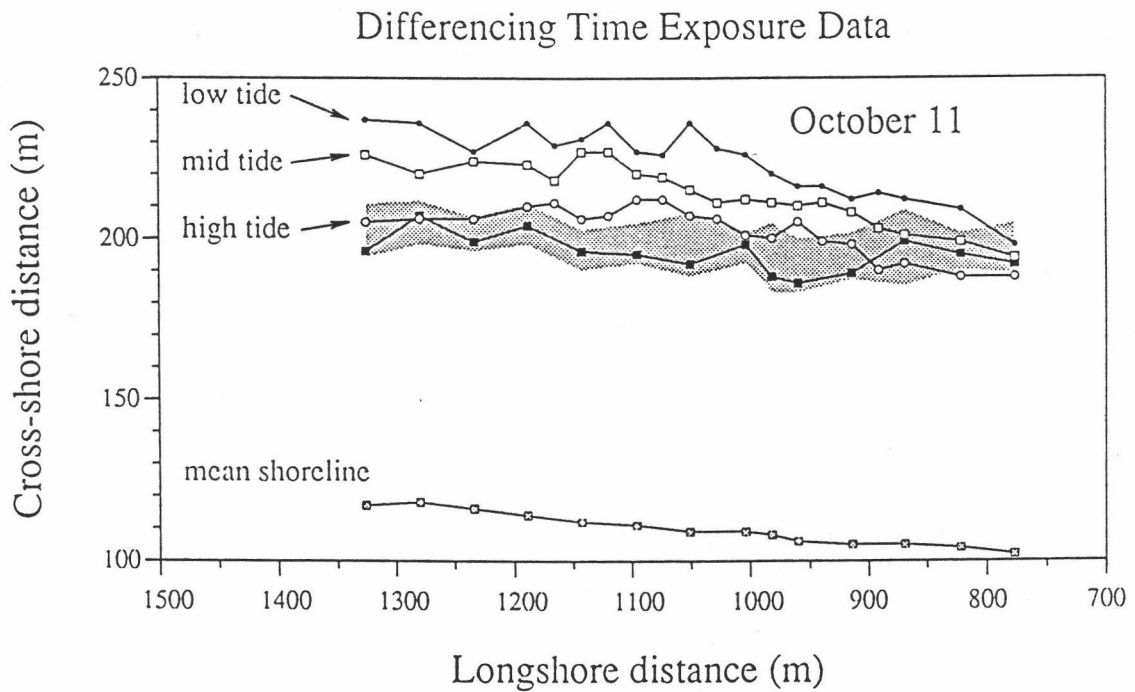


Figure I - 19. Location of mean shoreline, measured bar crest (solid squares), and intensity maxima from differenced time exposures obtained at low, mid, and high tide on October 11, 1986. The stippled area indicates the area around the crest for which the water depth is within 5% of h_c .

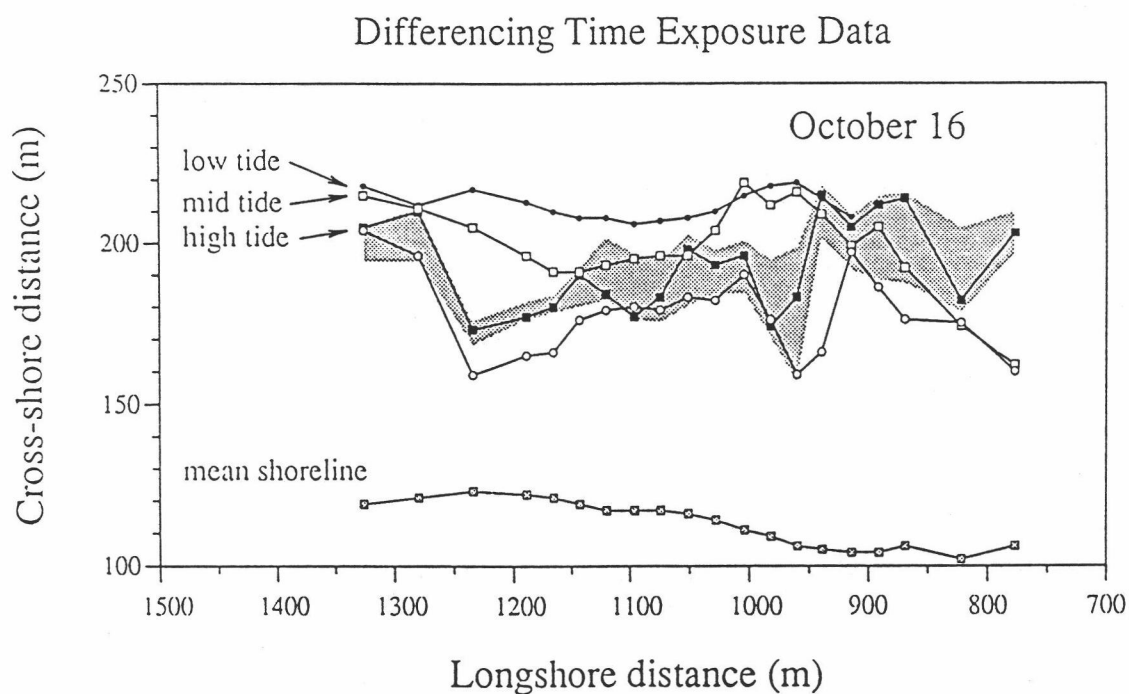


Figure I - 20. Location of mean shoreline, measured bar crest, and intensity maxima from differenced time exposures obtained at low, mid, and high tide on October 16, 1986. The stippled area indicates the area around the crest for which the water depth is within 5% of h_c .

The above discussion supports the hypothesis that our time exposure technique (modified by a differencing algorithm) is representative of energy dissipation of incident wave breaking. Continuing the comparison, we attempt to characterize the discrepancies in bar location, Δx , as a function of non-dimensional wave height, H_C^* . The Δx values arising in the differencing technique for October 9, 11-16 are normalized by the mean distance to the bar crest (different along each profile for each day) and plotted against H_C^* in Figure 21. The results, while noisy, are not inconsistent with the model behavior shown in Figure 6.

Shoreline Agreement

A further feature in time exposures is the representation of a shore break which shows up as higher intensity values along the beach face. The cross-shore profiles shown in Figures 12 and 18 have well-defined peaks in the vicinity of the shoreline. This intensity maxima for all cross-shore profiles (from simple time exposures) are compared quantitatively with the calculated shoreline location in Figure 22. The calculated shoreline location was determined as the intersection of the linearly interpolated profile and the still water level at the time of the survey. The correlation is very good ($r = 0.92$), however, the slope of the line through the data is slightly greater than unity, potentially a result of set-up or other swash dynamics. For individual days the agreement is excellent, for example on the 12th when image quality was best the intercept is -2.0 and the slope 1.02 ($r = 0.97$).

The persistence of foam near the mean run-up location generates an unusual result for the differencing technique. Since foam intensity appears fairly constant, the contrast difference will always be low, hence the mean shoreline for the differencing image often shows an intensity minimum that corresponds to the location of the maximum for the simple time exposure. Shoreline location appears best done with the simple time exposure.

Differencing Time Exposure Data

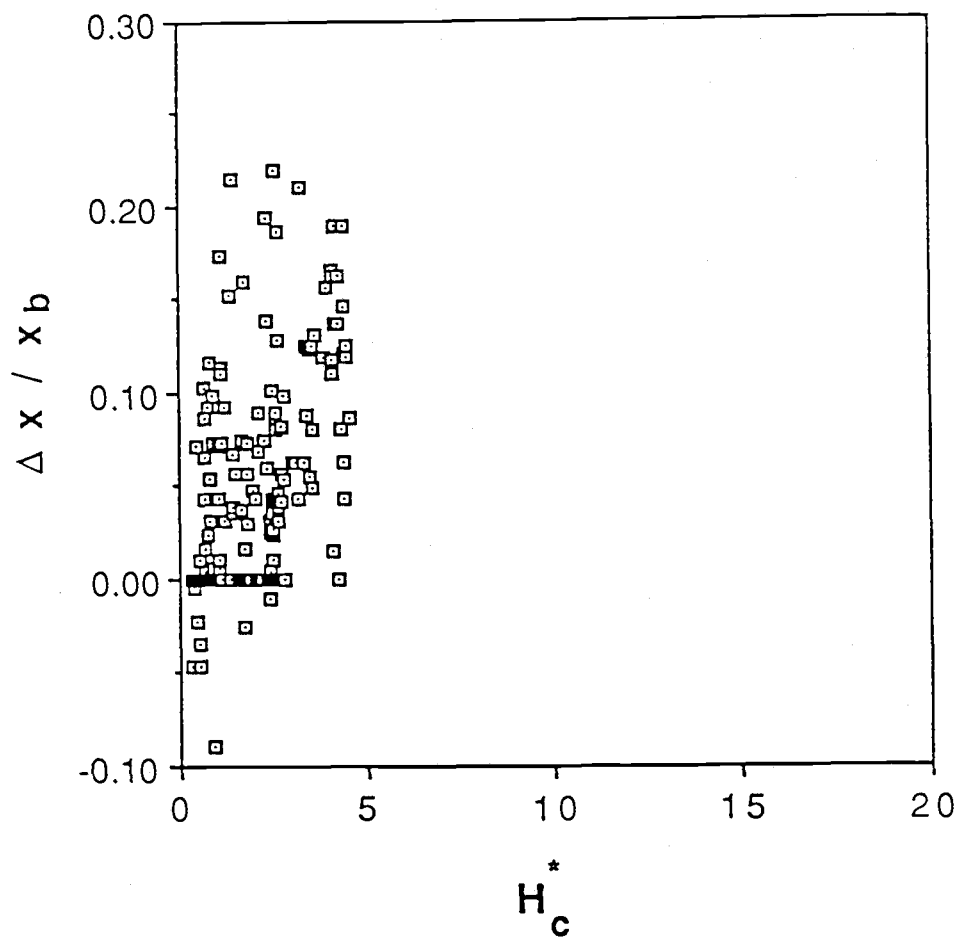


Figure I - 21. Results from differencing time exposures on October 9, 11-13, 15-16 showing the fractional error in locating the bar crest plotted against non-dimensional wave height, H_c^* . Negative $\Delta x / x_{bar}$ values indicate a landward offset in intensity bar location estimate.

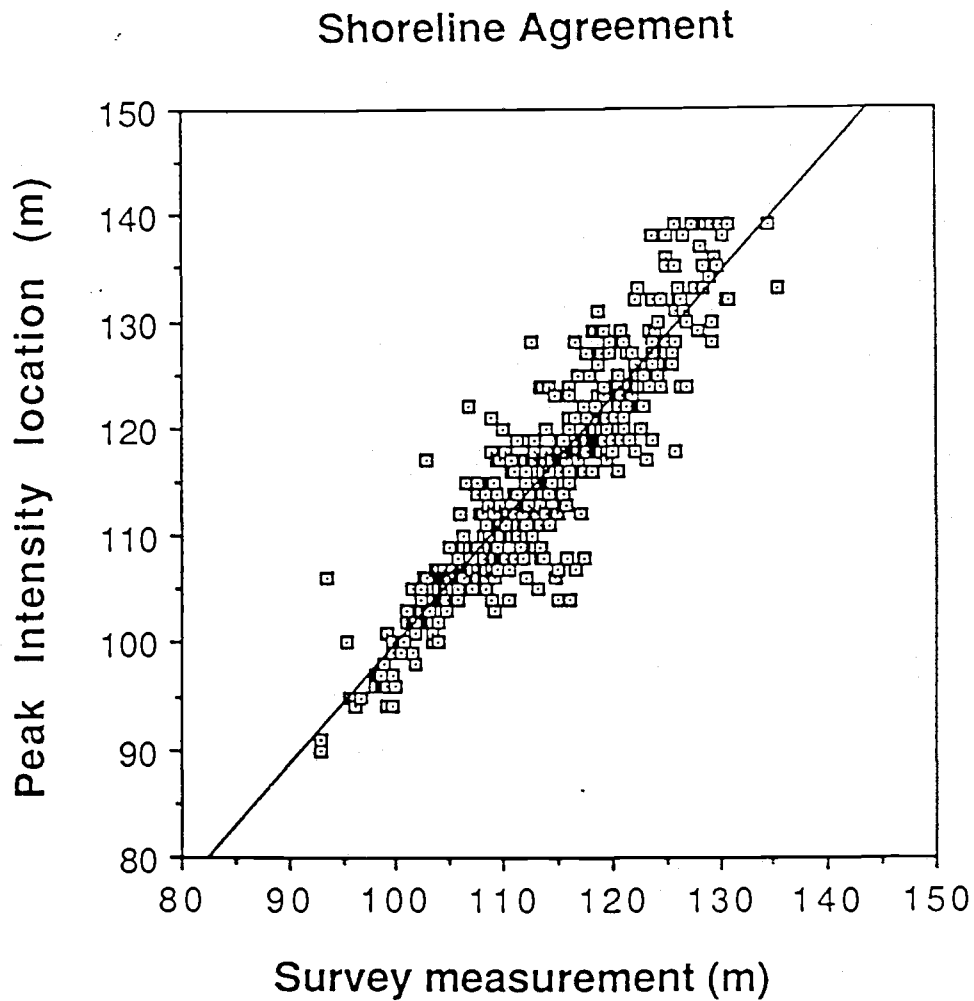


Figure I - 22. All shoreline intensity maxima locations from simple time exposures obtained at low, mid, and high tide on October 6, 9-16 plotted against measured shoreline location. The regression line is given by $y = -14.8 + 1.15x$ ($r = 0.92$).

DISCUSSION

Both the simple time exposure and the differencing time exposure techniques seem to provide a valuable tool for studying nearshore morphology. Both detect the presence of a bar system and allow measurement of any dominant longshore length scales of rhythmicity. Both can be used to estimate cross-shore length scales, a necessary prerequisite for testing bar generation models. The results from the differencing technique are quite similar to the model which is based on sound physics, so relative errors are better understood and, fortunately, are constrained by incident wave saturation. The simple time exposure technique may be biased by problems associated with residual foam accumulation, so that, for non-dimensional wave heights, H_C^* , greater than about 1, estimates of bar position can be subject to error for which we have little understanding. Nonetheless, our results show that the simple time exposure will generally yield good bar position estimates. This is due to a fortuitous case of compensating errors; dissipation of larger waves tends to give errors in the offshore direction while foam tends to compensate toward the onshore. Unfortunately, we have only a qualitative understanding of the process. When residual foam is apparent, the technique will work best at low tide when H_C^* is low, and will generally be worse for higher tides (higher H_C^*). Correcting the offshore discrepancy between intensity maximum and bar crest locations using H_C^* would be difficult; details in the beach profile, as well as surface foam biasing, may cause errors in the location of intensity maxima which are unrelated or not easily related to the H_C^* parameter. Thus we stop short of calculating correction equations for the bias.

The relevance of H_C^* in understanding errors in the technique is reassuring from a theoretical point of view. However, it is of dubious practical value since we do not know h_c , the depth at the bar crest. Instead, a user of the technique must refer back to the qualitative wave parameterizations. Both simple and differencing techniques work well when the waves are "just breaking" over the bar. The simple technique starts to break

down when the presence of foam no longer seems directly related to the amount of local dissipation. Both of these limits are of a type that may be visually assessed prior to analysis.

The calibration of the time exposure technique discussed in this paper assumes that the appropriate measure of a sand bar location is the point of minimum depth. This may not always be true. For example, for the bar generation mechanism presented by Holman and Bowen (1982) the sand bar is treated as a perturbation to an underlying beach profile. The point of maximum perturbation will always be offshore from the point of minimum depth, on the seaward slope of the typical bar where the local slope equals a representative mean slope. Thus the errors in the time exposure technique will probably be less for this application. Holman and Bowen also point out that in their theory a low-tide terrace can be thought of as a small amplitude bar. Again, the appropriate location of the maximum perturbation would be at the slope break, just the point imaged by the time exposure technique.

CONCLUSIONS

We have developed a technique to measure the scales and morphology of natural sand bars based on the preferential dissipation of wind waves and swell over the shallows of the bar. We do not actually measure dissipation, but instead record the visual signal created by breaking incident waves, and assume that this is proportional to dissipation. The visual wave breaking patterns are imaged photographically, with statistical uncertainty reduced by the use of time exposures (essentially averaging over a length of time long compared to modulation time scales for incident wave height). Analysis of the photogrammetry shows that positional information in the resulting images can be quantified to an accuracy of 5% of the distance to the camera.

Theoretical modelling shows the sensitivity of incident wave dissipation to perturbations in bottom slope, hence the potential for using dissipation to locate bars. An important parameter is the non-dimensional wave height, $H_C^* = (H_0/\gamma h_c)(k_c/2k_0)^{1/2}$, where H_0 is the deep-water rms wave height, h_c and k_c are the depth and wavenumber at the bar crest, k_0 is the deep water wavenumber, and γ is a breaker constant, taken as 0.42 for this study. For $H_C^* = 0.5 - 1.0$ the waves are just breaking and the dissipation maximum corresponds well to the bar crest position. Larger H_C^* result in weighting the dissipation maximum farther offshore up to a maximum location beyond which the local wave field is saturated. The maximum discrepancies based on a reasonable example are 35% of the true bar crest distance.

Ground truth testing, conducted during SUPERDUCK, confirm the capabilities of the time exposure technique for detecting the presence of a sand bar system as well as detecting longshore variability and rhythmicity and quantifying lengthscales. Cross-shore scale estimates are good for small H_C^* , but for higher waves persistent foam biases the intensity shoreward in ways for which we have no theory. The use of video differencing (the subtraction of consecutive frames) removes residual foam from the image and results

from differencing time exposures appear consistent with our theoretical dissipation modelling. Relative errors may be assessed using H_C^* , but adjustment corrections may not be reliably made using this parameter due to unknown profile characteristics and a breakdown in understanding the physical behavior of surface foam accumulation.

ACKNOWLEDGEMENTS

We would like to thank the entire FRF staff for their tireless efforts during SUPERDUCK, particularly Curt Mason (who made it all happen), Bill Birkemeier, and Ronbo. COL Grum was instrumental in approval and construction of the FRF tower. Much credit and personal thanks is owed to Paul O'Neill whose engineering skills and programming contributions made this work possible. Funding for the development of the image processing system and time exposure technique was provided by the Office of Naval Research, Coastal Sciences Program, under contract N00014-84-0218. The ground truth study during SUPERDUCK was funded by the US Army Corps of Engineers, Coastal Engineering Research Center under the Barrier Island Sedimentation work unit (thanks, Suzette). The analysis was carried out while the authors were on temporary leave at Dalhousie University and we thank them for their hospitality. Finally, thanks to Marcia for the care packages.

CHAPTER II

The Stability and Spatial Variability of Sand Bar Morphology

ABSTRACT

The spatial variability and temporal stability of nearshore sand bar morphology are quantified using a unique data set spanning two years. The data consists of daily time exposure images of incident wave breaking which may be used to infer bar morphology (Lippmann and Holman, 1989). The morphology in each image is classified into an eight state morphologic scheme in which bars are uniquely defined by four criteria. The most frequent morphology is the longshore-periodic (rhythmic) bar, observed in 68% of the data. Linear bars occur under highest wave conditions ($\bar{H}_s = 1.78\text{m}$) and are unstable (mean residence time ≈ 2 days). Shore-attached rhythmic bars are the most stable (mean residence time ≈ 11 days) and generally form 5-16 days following peak wave events. Non-rhythmic, three-dimensional bars are very transient (mean residence time ≈ 3 days). 87% of transitions to lower bar types (defined in text) occurred sequentially (one state at a time) under declining wave conditions. Transitions to higher states occur under rising wave energy and were spread more evenly between single (49.5%) and multiple step jumps, with more substantial changes in morphology resulting from larger wave increases.

Time exposure images were also digitized to yield quantitative estimates of bar crest location as a function of longshore distance. Principal component analysis was used to decompose bar position into two-dimensional (linear) and three-dimensional (longshore variable) components. Cross-shore (linear) bar position ranges $\pm 50\text{m}$ about the two-year mean (27m standard deviation) and dominates bar variability (74.6%). Three-dimensional bar structure accounts for $\sim 14\%$ of the variance (12m standard deviation). Changes in incident wave height precede cross-shore bar migration by less than one day. Changes in longshore variability are inversely correlated to changing wave conditions, with bar morphology becoming rapidly linear during storms (on time scales of less than one day). Evolution to significantly three-dimensional structure typically occurs over 5-7 days following peak wave events.

INTRODUCTION

The dynamics of nearshore beach topography have proved to be complex. Considering the large sediment volume associated with major bar forms, the position and variability of bars has important implications in both long-term and short-term beach stability. Therefore, quantitative investigations of morphologic bar changes will yield valuable insight to processes controlling nearshore topography.

Descriptions of natural sand bar systems have been extensively reported in the literature, with forms ranging from two-dimensional linear bars with no longshore variability to three-dimensional crescentic bars with coherent longshore periodicity. The first attempts to characterize the transition between bar forms were related to an annual cycle in wave energy (with bars located farther offshore during higher energy months). However, Sonu (1973) noted that beach cycles involving crescentic bars could be a response to a series of storms, on much shorter time scales, and that bars tended to migrate shoreward under swell conditions. Many authors have also observed that erosional sequences were associated with the growth of waves, and accretional transitions with the subsidence of waves (e.g. Sonu and James, 1973). More detailed information regarding the response to random storm events is still poorly understood.

Field studies have been designed to address the behavior of topographical beach changes under the influence of various fluid motions. Interpretations of data have followed two lines: development of models for equilibrium (static) bar formation which predict the scales of bars, and development of sequential morphologic state models which predict the shapes of bars.

Many equilibrium models have arisen from studies of beach topography that have been restricted to single profiles periodically surveyed over varying lengths of time (e.g. Sonu and van Beek, 1971; Sonu and James, 1973; Aubrey, 1979; Aubrey, et al., 1980; Aubrey and Ross, 1985; Birkemeier, 1985a; Birkemeier, et al., 1989b). These studies

focused on the cyclic behavior associated with cross-shore sediment transport, most notably characterized by the seasonal cycle in accretion and erosion. Longshore variability in on-offshore sediment transport was not addressed. In recent field studies, the DUCK85 and SUPERDUCK experiments, intensive daily three-dimensional surveys provided valuable quantitative information about bar evolution, but required enormous logistic effort (Sallenger, et al., 1985; Howd and Birkemeier, 1987a, 1987b; Mason, et al., 1987; Crowson, et al., 1988; Birkemeier, et al., 1989a).

Considerable research has also been directed toward understanding and predicting the shape and position of nearshore bars, resulting in sequential morphologic models which qualitatively predict the occurrence of beach states. Ordered sets of bar types, or classification schemes, have been presented (with varying degrees of success) that include the range of possible morphologies observed on natural beaches (Greenwood and Davidson-Arnott, 1979; Chappell and Eliot, 1979; Short, 1979; Wright, et al., 1979; Goldsmith, et al., 1982; Wright and Short, 1983; Wright and Short, 1984; Horikawa, 1985). Some of these investigators have correlated beach states with wave height and wave power, or other various surf similarity parameters, yielding a qualitative understanding of the equilibrium conditions most closely associated with each state.

Wright and Short (1984) present the most highly evolved classification scheme, summarized on the left side of Figure 1. They specify six beach states ranging from completely dissipative to completely reflective. Beach classification is based on a series of morphodynamic characteristics, the most representative of which is bar morphology. They use a morphodynamic data base spanning more than six years, consisting of visual surf zone observations from a number of environmentally different beaches. Wright, et al. (1985) and Wright, et al. (1986) use this model to form empirical correlations between beach state and various parameters, most notably a weighted, running mean of Dean's parameter $\Omega = H/(wT)$, where H and T are wave height and period, and w is the sediment fall velocity at the bar crest (Dean, 1973). Though the scheme appears to encompass

(reasonably well) the entire range of possible beach states, not all of the classification definitions are unique. The most notable ambiguities are related to the longshore structures of the bar.

Most previous long term studies, like Wright and Short (1985) were based primarily on visual observations in which three-dimensional bar characteristics were inferred from patterns of incident wave breaking. This method is not limited by longshore coverage, but usually yields only limited information on bar position and length scales. Only very large scale structures can be identified; more subtle features of the bar are not resolvable with confidence. As a result, little quantifiable evidence has been presented regarding the stability of bars and time scales associated with large scale morphologic change (e.g. Goldsmith, et al., 1982).

The impetus for this study was to quantify, in a robust manner, the temporal stability and spatial variability of sand bar morphology. Of particular interest is the evolution of three-dimensional morphology in relation to high energy storm events. Morphology data were collected over a two year period using a time exposure video technique (Lippmann and Holman, 1989). The analyses presented follow two distinct lines. First, bar samples are classified into an eight-state model based on four classification criteria. Secondly, time series of bar crest position are decomposed into two-dimensional (linear) and three-dimensional components using empirical orthogonal functions. For both analyses, comparisons are made with incident wave parameters, and response time scales are estimated.

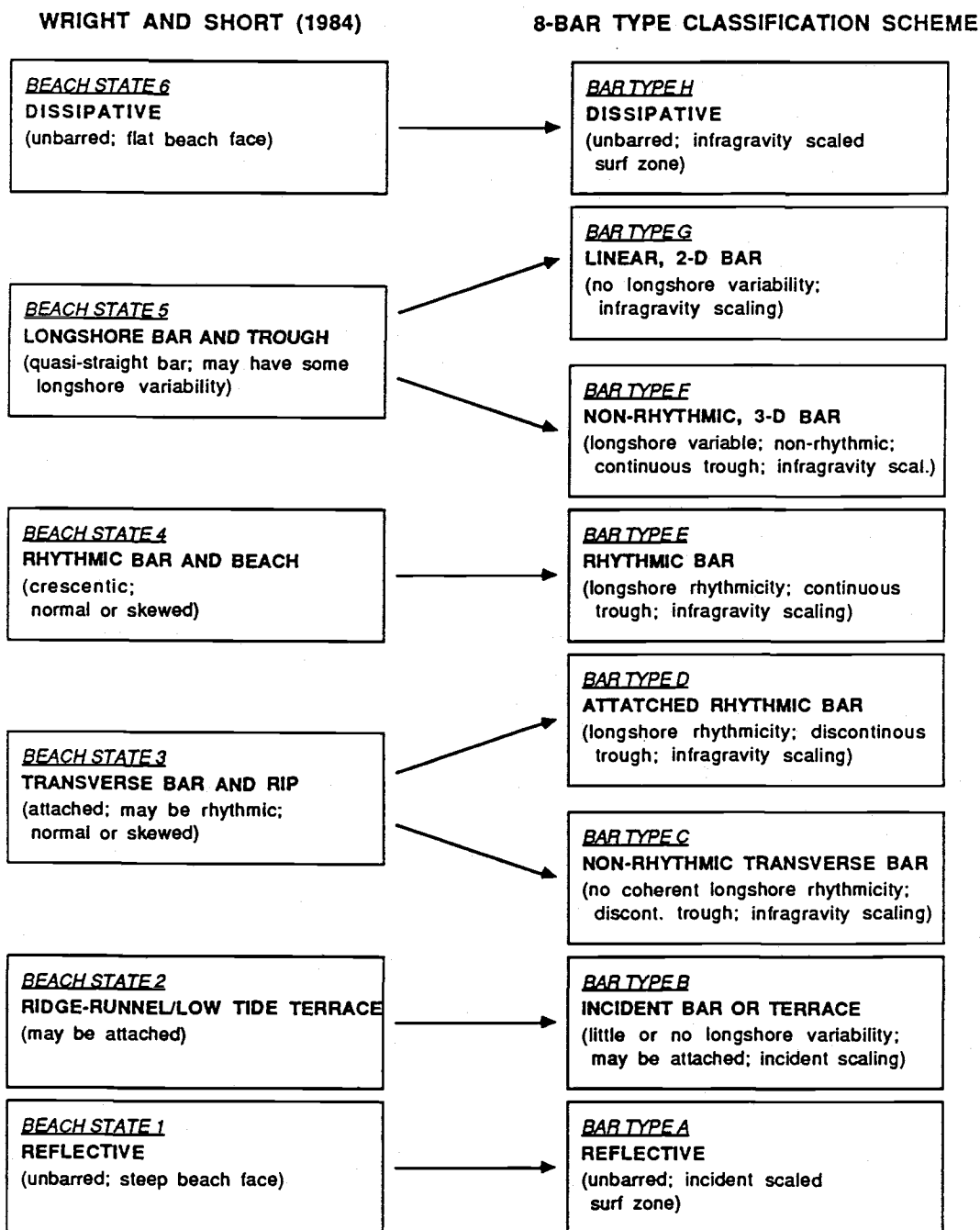


Figure II - 1. Six state classification scheme of Wright and Short, 1984, shown on the left side, and our eight state classification scheme, shown on the right side. Comparisons between the two models are indicated with arrows between similar morphologic states.

METHOD OF SAMPLING MORPHOLOGY

The method for sampling bar morphology must satisfy two criteria. First, the shape of the bar must be easily identified so that classification distinctions can be made. Second, the position of the bar crest must be accurately measured over a range of longshore distances.

In this study, we exploit a recently developed remote sensing technique, time-averaged imaging of incident wave breaking, which rapidly estimates the location of the bar crest over large longshore distances. The technique is not constrained by high energy surf zone conditions, and therefore may be employed when more traditional sampling methods must be abandoned. The technique is presented fully in Lippmann and Holman (1989; henceforth LH89), and is only summarized here.

The technique is based on the preferential breaking of incident waves over the shallows of a bar, similar to past visual observational methods. The sharp contrast in light intensity between breaking and non-breaking regions may be imaged photographically; however, instead of using an instantaneous "snapshot", we employ a long time exposure (typically ten minutes), thereby averaging out fluctuations due to incident wave modulations and giving a statistically stable image of the incident wave breaking pattern (Figures 3a-f). Peaks in cross-shore intensity indicate the presence of a sand bar, while the shoreline is indicated by an intensity maximum at the water's edge. Clearly, the technique is only valid if waves are breaking over the bar.

Time exposure images are created from video recordings of the surf zone by digitally averaging individual frames over a ten minute period using an image processing system. Pixel (picture elements) locations may be transformed into corresponding ground coordinates using photogrammetric relationships (LH89). Shore normal transects of light intensity may then be found, in which intensity maxima occur at the shoreline (a result of the shore break) and in the vicinity of the bar crest.

Calibration studies have shown that the location of the shoreline and longshore variability in bar form are both accurately measured using conventional time exposures (LH89). However, because of an accumulation of persistent foam near the shoreward edge of the bar crest, cross-shore estimates of bar crest locations may be displaced landward. To remove this bias an image differencing technique is employed. Persistent foam, not associated with actively breaking waves and bores, is removed by subtracting successive video frames and averaging the difference images. The result, called a differencing time exposure, proves better for locating the actual position and longshore variability of the bar crest. The differencing procedure, although fairly robust, requires good video quality and incorporates two free parameters: the time interval between successive frames and a threshold (intensity) noise level. Best results were found when these values were set respectively at 1 second and ~6% of the maximum range of intensity.

Experimental errors result from two sources. The first is simply related to the photographic resolution of the image. For this study, at worst resolution, errors were always less than 2.0% of the distance to the camera (less than +/-1m in the cross-shore, and +/-2.5m in the longshore). A greater error arises from the location of maximum wave dissipation, in which the estimated bar crest positions are weighted offshore from the true bar crest location by a small amount that varies with the tide. Percentage errors are generally on the order of less than 5-10% of the cross-shore distance to the crest (with theoretical worst-case errors of less than 35%; LH89). For this study the average error is estimated to be less than 15m seaward of the crest, and does show a tidal dependence.

METHODS OF CHARACTERIZING MORPHOLOGY

Sequential Classification Scheme

We choose to define bar types based on four characteristics of their morphologic shape, called classification criteria, and are defined as follows:

- (1) Existence or absence of a bar. Existence implies the realization of a discernable trough region where little or no incident wave breaking occurs (imaged as a darker region between the lighter breaking pattern over the bar and the shore break).
- (2) Dominant bar scaling: incident vs. infragravity. Bar scaling is considered incident if the dominant cross-shore and longshore length scales of the bar are roughly equal to the local incident wave length scales (typically on the order of 10m). Bar scaling is considered infragravity if the dominant length scales are much longer. In the absence of an obvious bar, the width of the surf zone is used as a proxy measure to define representative length scales.
- (3) Longshore variability: linear (no variability), rhythmic, or non-rhythmic. Longshore rhythmicity is indicative of crescentic bars, welded bars, or regularly spaced rip channels.
- (4) Trough: continuous or discontinuous. The trough is considered discontinuous when the bar is attached to the shoreline, indicated by regions of continuous breaking from the bar to the shoreline.

This set of classification criteria form a system of binary (one is actually tertiary) decisions leading to unique bar definitions, illustrated by a flow chart (Figure 2) and look-up table (Table 1). Use of the scheme requires a number of subjective decisions.

Rhythmicity, for instance, does not require perfect periodicity, but implies that the structure is more regular than chaotic. Similarly, trough continuity is generally understood unless the bar is obviously attached at numerous locations alongshore. Note that in this model we

Table II - 1. Classification criteria used to describe bar morphology. Each corresponding bar type uniquely defined in this manner is shown in the last column.

BAR	SCALING	LONGSHORE VARIABILITY	TROUGH	BAR TYPE
absent - 0 present - 1	incident - 0 infragravity - 1	absent - 0 non-rhythmic - 1 rhythmic - 2	discontinuous - 0 continuous - 1	
0	1	N/A	N/A	H
1	1	0	1	G
1	1	1	1	F
1	1	2	1	E
1	1	2	0	D
1	1	1	0	C
1	0	0,1,2	0,1	B
0	0	N/A	N/A	A

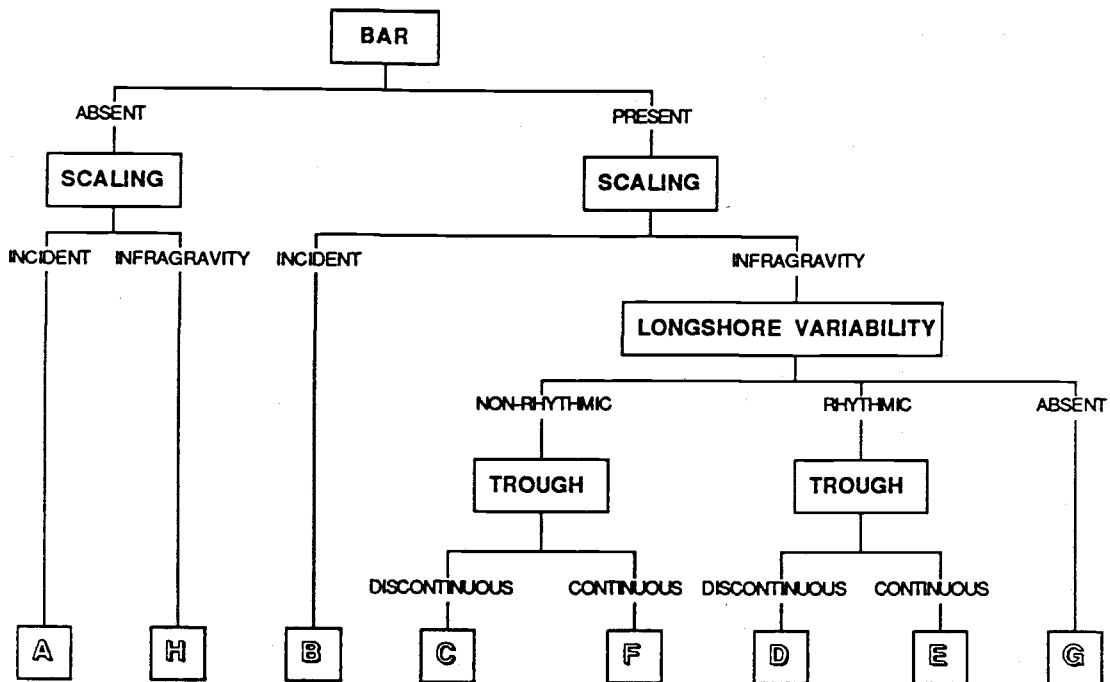


Figure II - 2. Classification criteria arranged in a workable flow chart. Morphologic classifications are based on one tertiary and three binary decisions. Each individual morphologic bar type (from the right hand side of Figure 1) is uniquely defined in this manner.

do not attempt to distinguish between incident scaled bars with varying degrees of longshore rhythmicity (since they were never observed). Also, criteria are used to describe characteristics of only the inner bar with no regard to the possible presence of multiple bars. Clearly, the last two criteria are not applicable for fully dissipative and reflective beaches.

The resulting model encompasses eight morphologically different bar types (shown on the right hand side of Figure 1). Bar types at the top of the scheme will be referred to as higher bar types; those at the bottom are considered lower bar types. This model is easily compared with Wright and Short's (1984) six state model (shown on the left hand side of Figure 1). Our definitions break up two states in Wright and Short's model. Their *Longshore Bar and Trough*, is divided into two bar types, one representing linear bars with no longshore variability (*Bar Type G*), and the other representing bars with non-rhythmic longshore variability (*Bar Type F*). Their *Transverse Bar and Rip* state is also divided into two bar types, each attached to the shoreline and with longshore variability distinguished by the presence (*Bar Type D*) or absence (*Bar Type C*) of dominant periodicity. The other bar types remain essentially the same.

This scheme has several distinct advantages. Mathematically, the set is complete and unique. It spans the complete set of all possible large scale bar states, ranging from fully dissipative to fully reflective. Furthermore, each state is uniquely defined by basic morphologic descriptions. Finally, the distinguishing criteria (particularly scaling and longshore variability) can be directly related to the testing of bar generation models, for example the scale of infragravity models or the existence of standing wave patterns.

Example time exposure images which best represent the observed morphologies (*Bar Types B-G*) are shown in Figure 3a-f. The two extreme morphologic bar types (*Bar Types A and H*), though prevalent at other field sites, were never identified at the field site and so no examples are presented. These examples are made from conventional ten-minute time exposures which yield the best view of the bar. When using these images to classify

Figure II - 3. Example time exposures which best represent the six observed morphologies at the field site. a) *Bar Type B*; August 9, 1987 b) *Bar Type C*; January 10, 1988 c) *Bar Type D*; October 17, 1987 d) *Bar Type E*; January 25, 1987 e) *Bar Type F*; March 6, 1987 f) *Bar Type G*; December 25, 1986.



Figure II - 3. [continued] (a) Bar Type B; August 9, 1987



Figure II - 3. [continued] (b) Bar Type C; January 10, 1988



Figure II - 3. [continued] (c) Bar Type D; October 17, 1987



Figure II - 3. [continued] (d) Bar Type E; January 25, 1987



Figure II - 3. [continued] (e) Bar Type F; March 6, 1987



Figure II - 3. [continued] (f) Bar Type G; December 25, 1986

bars, one must keep in mind the possibility of residual foam accumulation causing a landward bias in the position of the bar, which might alter decisions involving cross-shore scaling and trough continuity (discussed further in LH89).

The classification procedure was tested by nine individuals (with varying degrees of familiarity with nearshore processes) using a subset of 60 selected images covering the range of observed bar types. Figure 4 shows the variability of classifying each morphologic bar sample into the different classes. Tabulations for each individual showed that an average of 75% (+/-8%) of the classified samples agreed with the consensus bar type. Non-rhythmic bars were the most difficult to classify, with the most troublesome classification criteria involving the continuity of the trough and the determination of longshore rhythmicity. In general, our sampling method and classification scheme was found to be fairly robust for uniquely identifying each bar sample.

Longshore Structure of Bar Crest Position

The second method of describing sand bar morphology was to analyze the behavior of the bar crest position, $x_c'(y,t)$. The data used in this analysis is in the form of digitized x_c' locations (from daily differencing time exposure images) at numerous longshore locations. This signal can be objectively separated into two components, one representing the two-dimensional (linear) movement and the other representing the three-dimensional (longshore variable) behavior.

We accomplish this by restructuring the data using standard principal component, or EOF, analysis (Priesendorfer, et al., 1981). The mean corrected data, $x_c(y,t)$, are decomposed into orthogonal spatial factors, $e_j(y)$, and corresponding amplitude time series, $a_j(t)$, such that

$$x_c(y,t) \approx \sum_{j=1}^p a_j(t)e_j(y) = A(t)e_1(y) + \sum_{j=2}^p a_j(t)e_j(y) \quad (1)$$

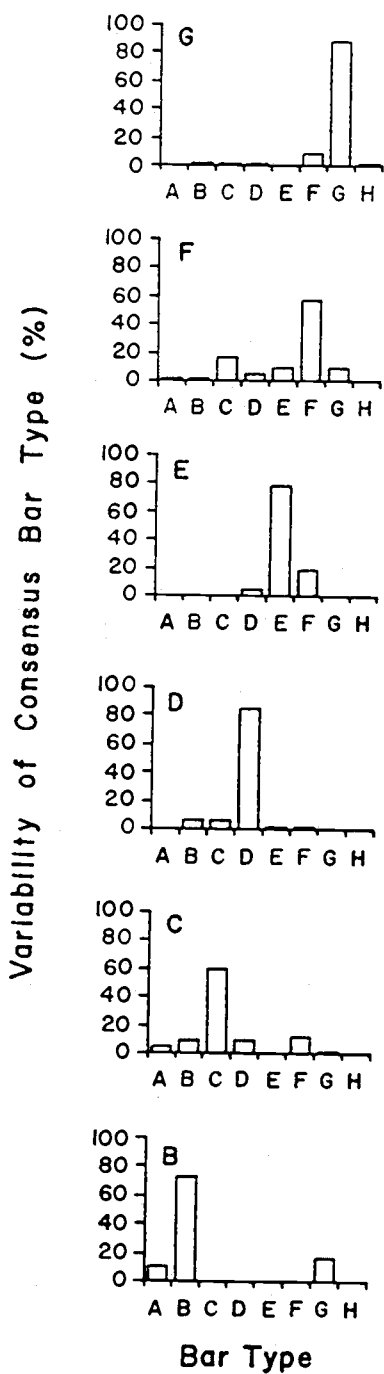


Figure II - 4. Results from morphological classification tests showing the tendency to classify bar types in states other than the consensus state. The highest percentage of classified bar types defines the consensus bar type, also indicated by the bold letters in the upper left corner of each graph.

where t is time and y is longshore position. A linear spatial factor, $e_1(y)$, represents the linear deviation of the sample mean bar position, $\bar{x}_c(t)$, from the data mean, $\bar{x}_c(y)$ (described later), and so $A(t)$ represents a quantified measure of the mean cross-shore bar movement. The remaining spatial factors are representative of three-dimensional structure and have a collective variance that quantifies the degree of longshore variability of the bar crest. Note that the series has been truncated at "p" significant factors to reduce noise in the analysis.

FIELD TECHNIQUES AND DATA COLLECTION

The data were collected as part of a long term monitoring program at the Army Corps of Engineers CERC Field Research Facility (FRF) on the Outer Banks of North Carolina near the village of Duck (Birkemeier, et al., 1985b). The area of interest ranges from dune crest to 200m offshore, begins approximately 180m north of the long FRF research pier and extends 660m alongshore to the north. Miller, et al. (1983) showed that this region is outside the area affected by the pier pilings.

The beach at Duck is characterized by a persistent, very dynamic inner bar, approximately 30-120m offshore, and a more stable outer (storm) bar approximately 300-400m offshore. The beach foreshore is predominantly steep, $\tan\beta \approx 0.08$ (1:12.5), and the shoreline is very stable, consisting of a mixture of medium quartz sand (mean grain size ≈ 1 mm) and carbonate shell debris (up to 20%). Offshore, the bottom slope approaches $\tan\beta \approx 0.0061$ (1:164) near the 8m depth contour, and the median grain size decreases to ~ 0.1 mm. The wave climate is variable throughout the year, with higher wave conditions dominated by extratropical nor'easters during the fall, winter, and early spring months. The summer months are characterized by lower amplitude, long-period swell from the southeast, with occasional tropical hurricanes during the late summer and fall. A more complete description of the beach conditions is contained in Birkemeier, et al. (1989a).

Video data were collected using a black-and-white television camera mounted on top of a 40m high tower erected on the dune crest 63m north of the pier (Figure 5). Daily video records of fifteen minute length were acquired from October 7, 1986 through October 1, 1988. Conventional and difference time exposure images of ten-minute length were created digitally using an image processing system. Each conventional time exposure was classified several times according to the previously presented scheme. In addition, thirty-four shore normal intensity profiles spaced 20m apart alongshore were digitized from the images and analyzed to give estimates of shoreline and bar crest position.

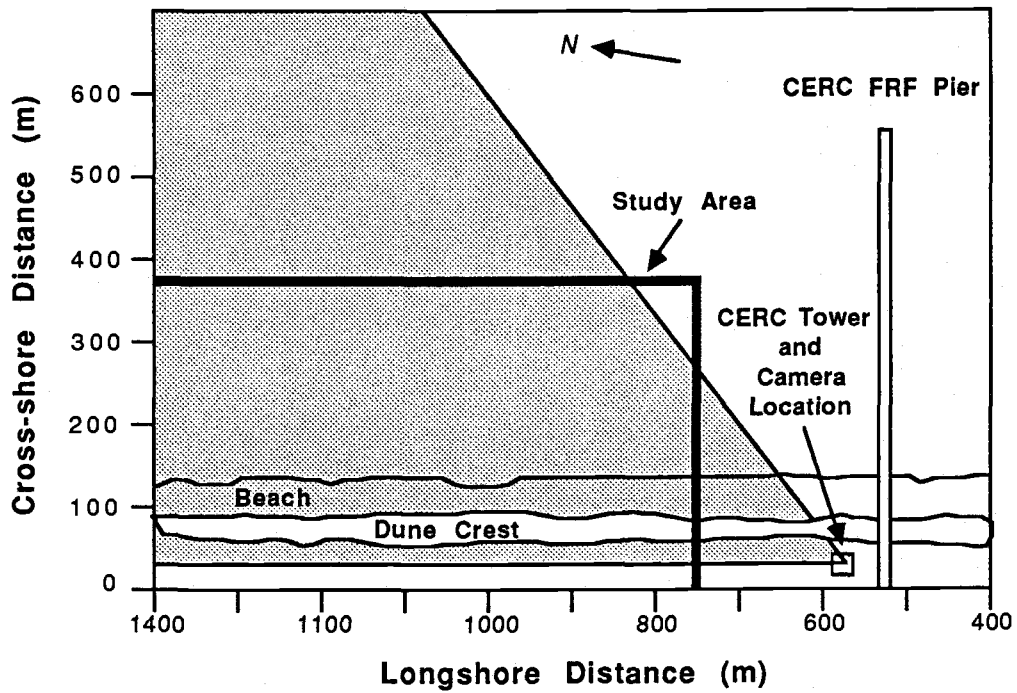


Figure II - 5. Map of the field site for the two year data record. The position of the camera in relation to the FRF pier and the study area is indicated. Longshore and cross-shore distances are relative to the FRF coordinate system. The stippled area indicates the ground coverage in the field of view of the camera.

Gaps exist in the time series of bar morphology for three reasons. First, occasionally the waves were too small to break on the inner bar; secondly, adverse environmental conditions such as snow and fog prevented the use of photographic imagery; and thirdly, recording occasionally failed (including a three week period from April 13-May 4, 1987). Marginal records were not included for the morphological analysis if image quality was too poor to allow a clear view of the bar. Records were also eliminated from the EOF analysis if at least 50% of the 34 longshore estimates of x_c were unsatisfactory. Occasional missing estimates were interpolated in the following manner:

$$x_c(y_i, t_j) = x_c(y_i, t_{j-1}) + (\bar{x}_c(t_j) - \bar{x}_c(t_{j-1})) \quad (2)$$

where over-bar denotes the longshore mean. That is, the interpolated value at a location is just the previous value at that location plus the change in the mean bar position over the time between adjacent samples. Inspection showed the method to work reasonably well with minimal introduction of systematic errors. A total of 523 days (72.2% of the total record) were used for the classification analysis, and 476 days (65.7%) were used in the EOF analysis.

Ancillary measures used in this study include 20 minute averages at six hour intervals of significant wave height, H_s , and peak incident wave period, T , collected by the FRF staff using a waverider buoy located 6km offshore. Missing data values were augmented using a Baylor wave gage located at the end of the pier.

RESULTS

Morphologic Stability

From the daily estimates of morphology, the probability of occurrence of each bar type, P_i , was found. Also, the number of transitions, N_i (the number of first occurrences of a given morphology), and the mean residence time, $\langle\tau_i\rangle$, within each state were tabulated. These measures are related in the following way:

$$P_i = \frac{N_i \tau_i}{\sum_k N_k \tau_k} \quad (3)$$

For the transition calculations, gaps in the data of less than five days (occurring on 5 occasions) were ignored. Results are shown in Table 2 and Figure 6.

Residence times, demonstrated by their means, $\langle\tau_i\rangle$, and standard deviations, s (Table 2 and Figure 6), may be interpreted as a measure of bar stability. Figure 6 shows high bar states are short-lived, with lower bar types remaining for progressively longer durations (with the exception of *Bar Type C*). Thus, the linear state (*Bar Type G*), as well as non-rhythmic bars (*Bar Types C and F*), may be considered relatively unstable ($\langle\tau_G\rangle \approx 2$ days; $\langle\tau_C\rangle \approx \langle\tau_F\rangle \approx 3$ days), while rhythmic states seem much more stable ($\langle\tau_D\rangle \approx 11$ days; $\langle\tau_E\rangle \approx 5$ days) with stability increasing as bars become attached to, or in general, move closer to the shoreline. However, there is also a large amount of variability in τ_i , indicated by the high standard deviations in comparison to the means. Further analysis (later in this section) shows that most upward transitions (based on the scheme presented in Figure 1) occurred very rapidly, whereas transitions down were more often gradual, especially for the lowest bar types.

The most common bars observed were attached rhythmic bars, *Bar Type D* ($P_D = 43.6\%$); higher bar types (*E-G*) were seen on progressively fewer occasions. Even though *Bar Types E and F* occurred more often ($N_E = 30$; $N_F = 29$) than *Bar Type D* ($N_D = 22$),

Table II - 2. Total percent of observations, P_i , number of transitions to each bar type, N_i , and average residence times, $\langle\tau_i\rangle$, for each bar type.

	P_i (%)	N_i (days)	$\langle\tau_i\rangle$ (days)
H	-	-	-
G	6.7	19	2.05
F	13.8	29	2.94
E	24.0	30	4.66
D	43.6	22	11.09
C	3.3	6	3.17
B	8.6	3	18.00
A	-	-	-

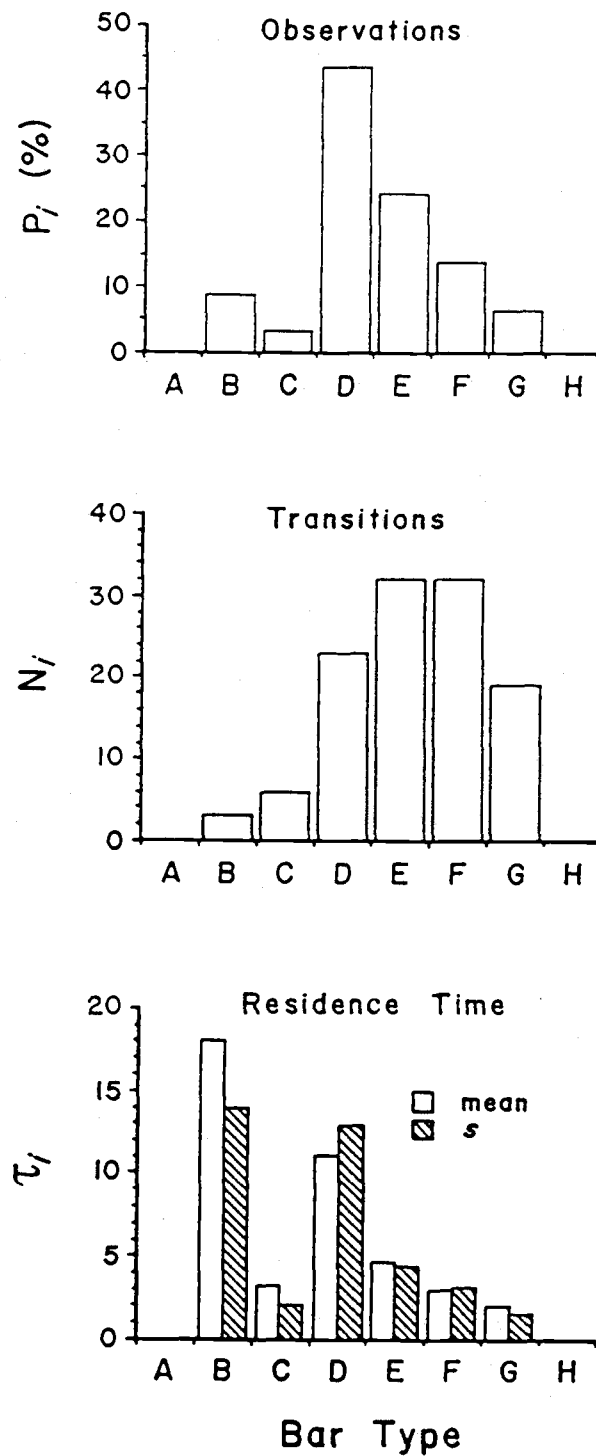


Figure II - 6. Histograms of probability of bar occurrence (%), P_i (upper panel), total number of transitions, N_i , to each state (middle panel), and mean, τ_i , and standard deviations, s , of mean residence times for each state (lower panel).

they were observed less often ($P_E = 24\%$; $P_F = 13.8\%$), a consequence of their shorter residence times. The lower bar types, *B* and *C*, were rare ($N_B = 3$; $N_C = 6$). The linear bar, *Type G*, though relatively uncommon ($P_G = 6.7\%$), did occur on many different occasions as morphology changed ($N_G = 19$). Incident scaled features were never observed in bars with longshore variability, and only occurred in the form of quasi-straight ridge-and-runnel or low tide terrace bars, *Bar Type B*. The differences in N_i and P_i are attributed to the relative stability of the individual morphologic forms.

The sequence of transition between the various bar types is also investigated (Table 3). If the present bar morphology is in state j , then the ij^{th} element in the table represents the percentage of transition from state j to state i . Transitions to lower bar types (below the main diagonal) usually occur sequentially, with 86.6% of downward transitions being single step. On the other hand, transitions to higher bar types (above the main diagonal) often occur in jumps (only 49.5% being single step). All bar types are observed to jump, at least on some occasions, to the highest state, *Bar Type G*.

The average wave conditions corresponding to the occurrence of each state were also found. Mean statistics were calculated for significant wave height, \bar{H}_s , incident wave power, $\bar{P}_0 = \rho g H_s^2 T^2 / 32\pi$ (proposed as important in parameterizing morphologic change by Short, 1979), offshore wave steepness, \bar{H}_0/L_0 (the wave part of the Irribaren surf similarity number, $\xi_0 = \beta / (H_0/L_0)^{0.5}$, proposed by Hunt, 1959), and finally \bar{H}_s/T (the wave part of Dean's parameter mentioned earlier). Surprisingly, when compared to our morphologic bar types we find that all these parameters behave in a similar manner (Figure 7). In general, higher bar types are associated with higher values of all wave parameters, similar to observations reported by previous authors (Short, 1979; Goldsmith, et al., 1982; Wright and Short, 1985; and others). The middle bar types, *C*, *D*, and *E*, occur under similar, intermediate wave conditions. No single measure shows superiority over any other for this particular field site; therefore, for simplicity, we will focus further discussion on wave height dependence.

Table II - 3. Percent transitions between morphologic bar types. Initial states are along the top and resulting states are listed on the left. The total number of transitions to each state, N_i , are shown at the bottom of each column.

		FROM							
		A	B	C	D	E	F	G	H
T O	H	+
	G	.	33	17	26	23	14	+	.
	F	.	.	33	23	23	+	84	.
	E	.	.	.	23	+	83	5	.
	D	.	67	50	+	47	.	11	.
	C	.	.	+	14	7	3	.	.
	B	.	+	.	14
	A	+
N_i		0	3	6	22	30	29	19	0

Linear bars are associated with the highest waves ($\bar{H}_s = 1.75\text{m}$), predominating at the peak of high energy storm events. Bars with longshore variability are associated with lower wave energy ($\bar{H}_s = 0.9\text{-}1.27\text{m}$), whereas quasi-linear incident scaled bars occur under the lowest mean wave conditions ($\bar{H}_s = 0.58\text{m}$).

Relationships between wave parameters and changes in morphology are also illustrated with transition tables. The average wave parameters associated with each transition were calculated at the first occurrence of a new bar type. The changes in wave parameters were calculated as the first occurrence value minus the mean value for the preceding state prior to the transition. Table 4 shows \bar{H}_s and $\Delta\bar{H}_s$ for the transitions. Down transitions are generally associated with lower \bar{H}_s and decreasing wave energy (negative $\Delta\bar{H}_s$), and thus are representative of accretional sequences. Up transitions to higher bar types are associated with larger waves and increasing wave energy (positive $\Delta\bar{H}_s$), indicative of erosional sequences, with jumps in morphology associated with higher waves (average $\bar{H}_s \approx 2\text{m}$) and larger increases ($\Delta\bar{H}_s \approx +1\text{m}$). Associations with other wave parameters yield similar results (Appendix A), but best results are indicated by simply \bar{H}_s .

The linear bar, *Type G*, requires largest wave energy to maintain its form, with small declines in energy resulting in the development of longshore variability, with this bar type evolving almost exclusively (84%) into the next lowest state, *Bar Type F*. Transitions between rhythmic bars appear to occur under small or minimal wave changes, illuminated by the commonly observed sequence in which unattached rhythmic bars (*Bar Type E*) migrate onshore under constant or declining wave conditions, maintaining its longshore form, and eventually attaching to the shoreline (becoming *Bar Type D*, also noted previously by other authors, e.g. Sonu, 1973). However, we observe opposite transitions in which *Type D* bars transform into *Type E* bars (i.e. with the formation of a trough) under declining wave conditions ($\Delta\bar{H}_s = -0.11\text{m}$). In general, the transitional behavior of

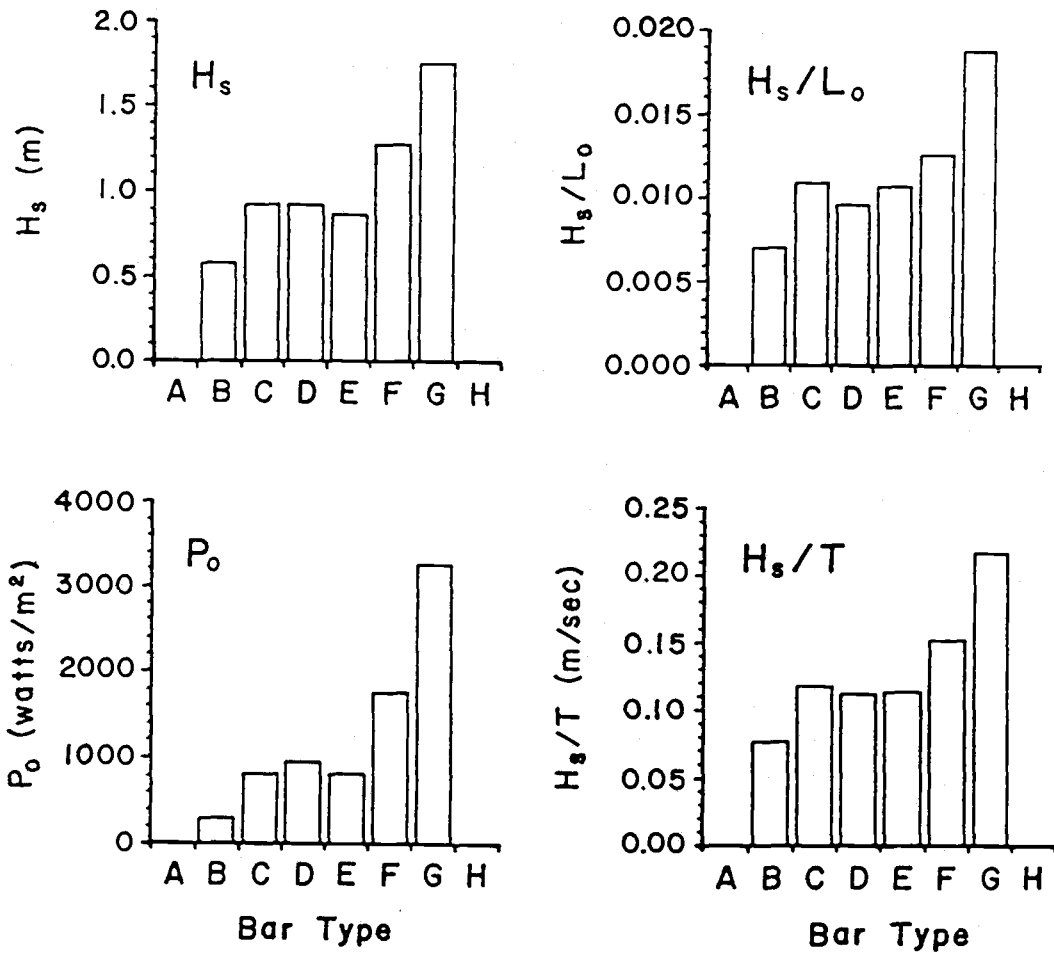


Figure II - 7. Histograms of \bar{H}_s , \bar{P}_0 , \bar{H}_0/L_0 , and \bar{H}_s/T for each bar type.

Table 4. \overline{H}_s (bold) and $\Delta\overline{H}_s$ for each transition. Initial states are along the top and resulting states are listed on the left. Statistics computed from less than 3 transitions are indicated with an asterisk.

		FROM							
		A	B	C	D	E	F	G	H
T O D E F G H	H	+
	G	.	1.69* +1.11	2.07* +1.50	1.95 +0.98	1.98 +1.10	1.02 +0.13	+	.
	F	↑	.	1.90* +0.92	1.45 +0.41	1.52 +0.76	+	1.39 -0.27	.
	E	.	.	.	1.03 -0.11	+	1.02 -0.37	0.82* -1.22	.
	D	.	1.09* +0.51	1.18 +0.25	+	1.15 +0.17	.	1.62* -0.79	↓
	C	.	.	+	1.01 +0.23	2.66* +0.54	0.71 +0.02	.	.
	B	.	+	.	0.52 +0.03
	A	+

*Computed from less than 3 transitions.

lowest bar types, usually occurring under relatively mild conditions, do not follow obvious trends with respect to changing wave energy.

Longshore Structure in Bar Crest Position

The mean shoreline, $\bar{x}_s(y)$, and mean bar crest position, $\bar{x}_c(y)$, for the two years of data are shown in Figure 8. $\bar{x}_c(y)$ is reasonably straight and parallel to $\bar{x}_s(y)$, and is located approximately 85m offshore. A small (~10%) offshore increase in $\bar{x}_c(y)$ farther away from the camera is an artifact of the image differencing method (LH89). This trend is removed with the mean and does not affect the following results. The standard deviation, s , is nearly constant alongshore indicating that $x_c(y)$ is homogeneous over the length of the sample area.

Figure 9 shows the decomposition of the mean-corrected bar crest data into the first five orthogonal EOF's ($e_j(y)$, eq. 2). Higher EOF's were considered to be insignificant, associated with sampling errors. EOF 1 is approximately linear, representing the mean cross-shore location of the bar, hence $A(t)$ represents the time-dependence of the two-dimensional morphologic component. The two-year variability in bar position is dominated by cross-shore bar migration (74.6% variance associated with EOF 1), with a range of mean on-offshore bar movement of +/-50m about $\bar{x}_c(y)$ ($s = 27m$).

The $A(t)$ time series reveals a predominant long period signal representative of the well known seasonal cycle in on-offshore sediment movement. There is also variability on a much shorter time scale. Though the range associated with this cycle ($s = 19m$) is less than the annual cycle, its variability characterizes the short term changes in bar position.

The next four EOF's represent longshore variability in bar crest position. These factors appear somewhat sinusoidal, a result of orthogonality constraints required in the analysis. Therefore, no attempt is made to correlate dominant wavelengths with length scales of observed rhythmic bars. Instead, we sum the factors (eq. 3) and then calculate the longshore variance associated with each sample. The resulting variance time series,

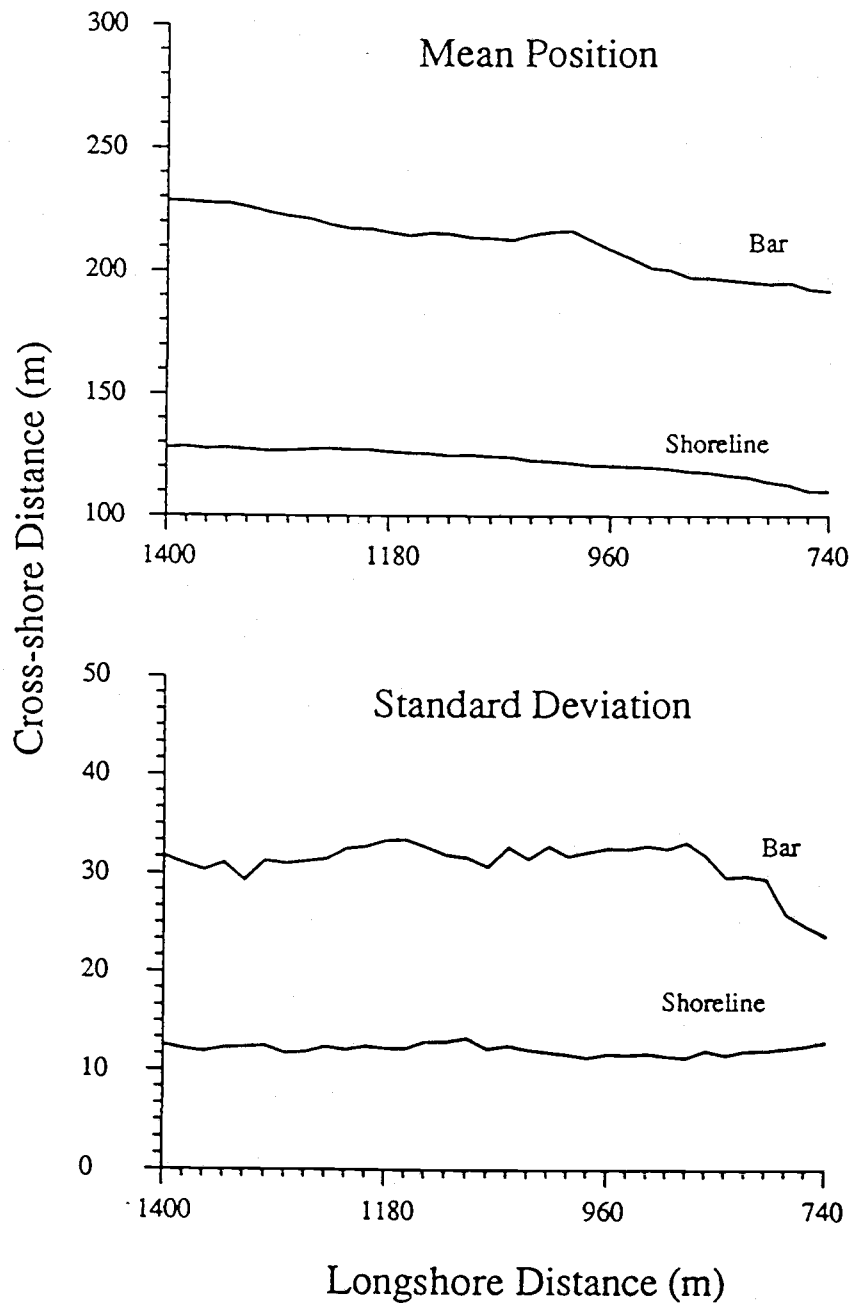


Figure II - 8. Two year mean shoreline and bar crest position for differencing time exposure data (upper panel) and the corresponding standard deviations alongshore (lower panel). The longshore and cross-shore distances are relative to the FRF coordinate system shown in Figure 5.

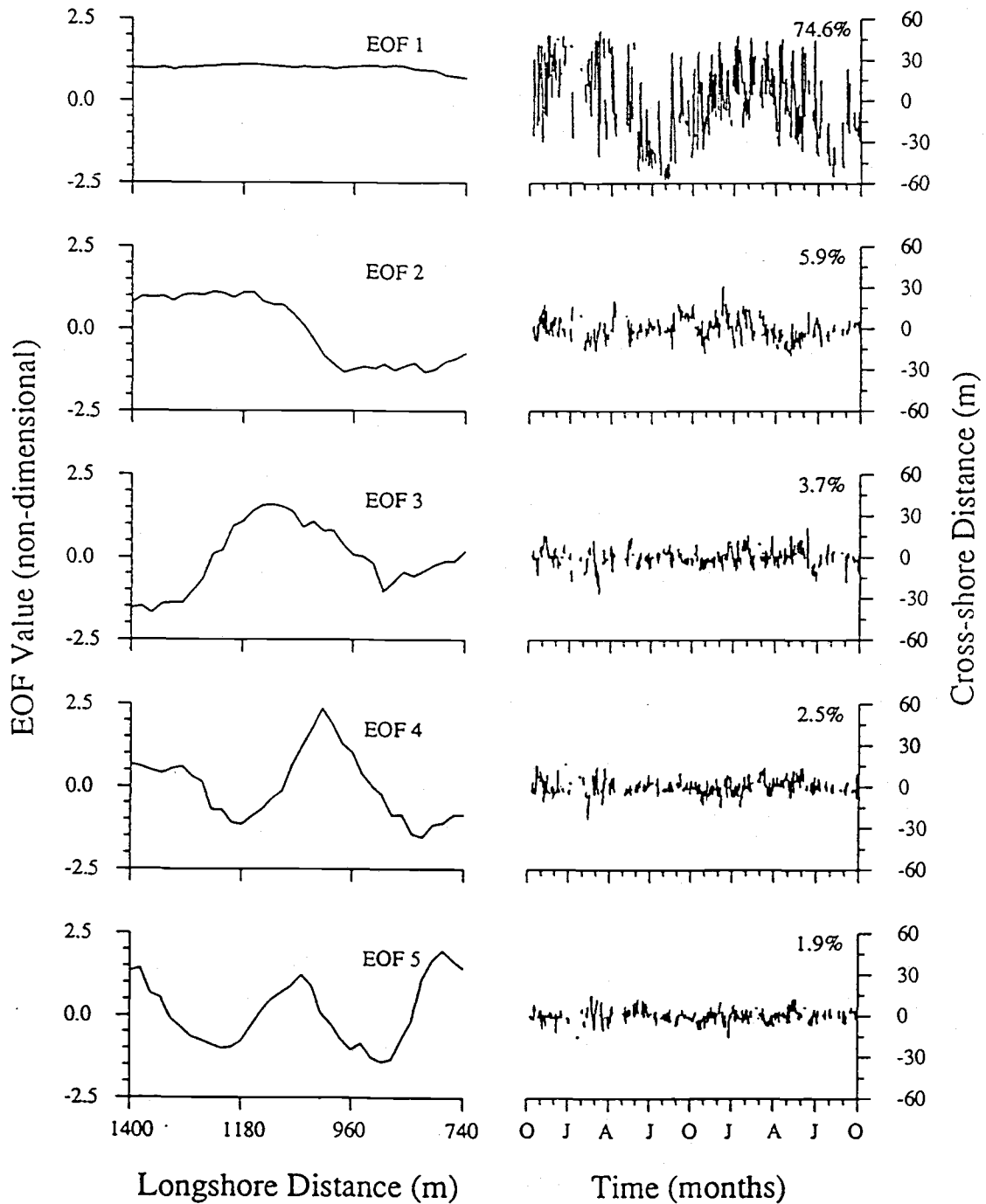


Figure II - 9. The first five EOF's from the decomposition of the differencing bar crest data. Spatial factors are shown on the left side, where the longshore distance is relative to the FRF coordinate system and the EOF values are non-dimensional. Corresponding amplitude time series are shown on the right side, along with relative variance contributions. The time scale (along the bottom) is in months, and the cross-shore distances are in meters and are relative to the two year mean (Figure 8).

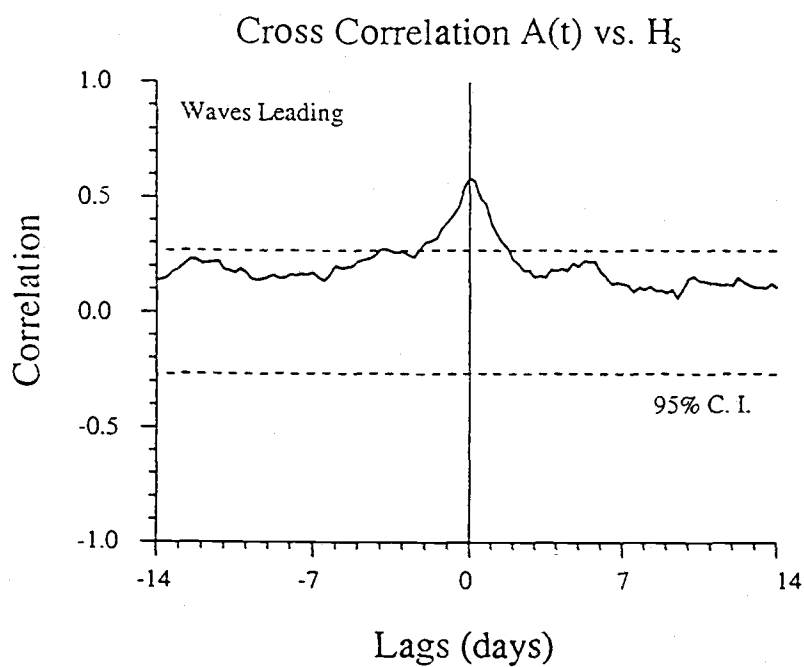
henceforth $V(t)$, represents the evolution of longshore variability associated with the three-dimensional component in bar position (although it does not distinguish rhythmic from non-rhythmic structure). The total percent variance associated with $V(t)$ is $\sim 14\%$ ($s = 12\text{m}$), one-fifth that of the on-offshore variance.

Cross-correlations between $A(t)$ and H_s for lags out to ± 14 days are shown in Figure 10a. The high positive correlation at zero lag ($r=0.58$, 95% significant level) indicates that the on-offshore movement of the mean bar position tends to be concurrent with incident wave energy. The consistently positive correlations at longer lags indicate that the long period seasonal cycle is influencing the correlation results. Since our interest is primarily on much shorter time scales (that associated with random storms), the seasonal cycle is removed from the time series by block-detrending with 21 day means (a time scale much shorter than the annual signal and much longer than the average storm event).

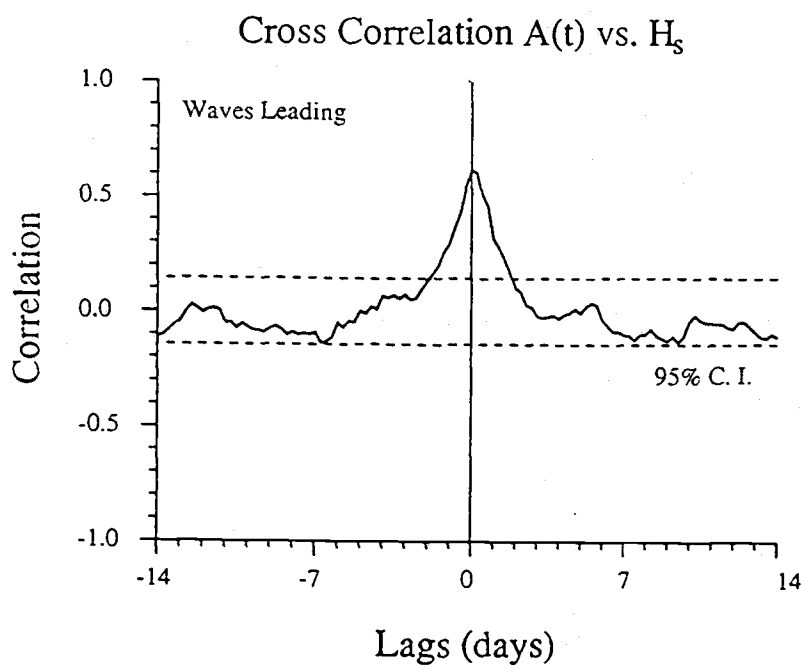
Correlations using the detrended $A(t)$ is shown in Figure 10b. Again, high positive correlations centered about zero lag exist ($r=0.62$). The decorrelation time scale indicates that previous wave events occurring more than about 2 days past do not significantly influence the position of the bar. Correlations with other parameters yielded similar results (Appendix B), but once again, best results (highest correlations) were found using H_s . All following analysis will be with time series that have the seasonal cycle removed by their 21 day means.

Response time scales are estimated using cross-correlations between $\Delta A(t)$ and ΔH_s (over a six hour period), shown in Figure 11. The positive correlations from 0 to -0.5 day lags ($r=0.30-0.37$) indicate that changes in wave height tend to precede on-offshore bar migration by less than one day, a very rapid response (note that significant correlations at zero lag indicates that changes in each time series occur concurrently). Correlations at all higher lags are observed to be insignificant ($\alpha=0.05$).

A positive correlation means either that increasing H_s precedes offshore migration or decreasing H_s precedes onshore migration. From this analysis, however, we can not



a)



b)

Figure II - 10. a) Cross correlation diagram showing A(t) vs. H_s for lags out to ± 14 days. b) Same cross-correlations only with each time series detrended with their 21 day means prior to analysis. For each the negative lags indicate H_s leading. The 95% confidence intervals (dashed lines) were calculated using the long-lag artificial skill method after Davis, 1976.

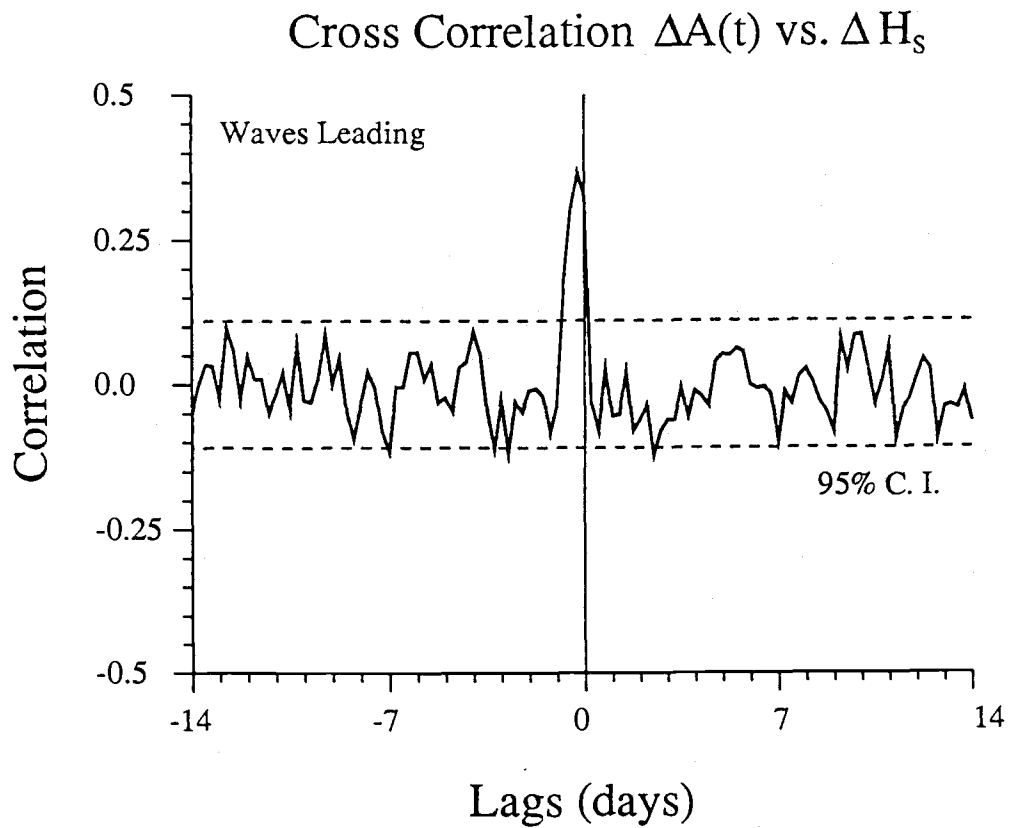
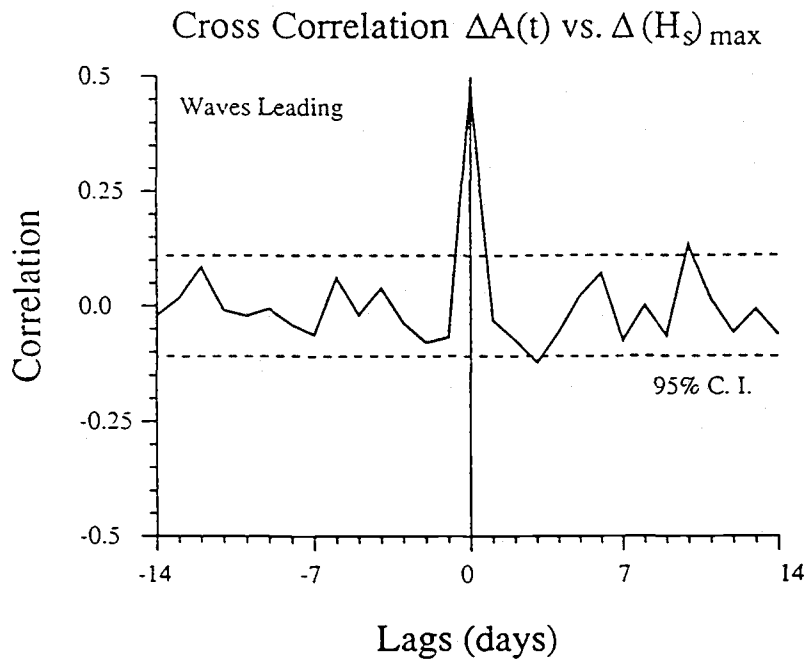


Figure II - 11. Cross correlation diagram showing $\Delta A(t)$ vs. ΔH_s for lags out to ± 14 days. The negative lags indicate ΔH_s leading. The 95% confidence intervals (dashed lines) were calculated using the long-lag artificial skill method after Davis, 1976.

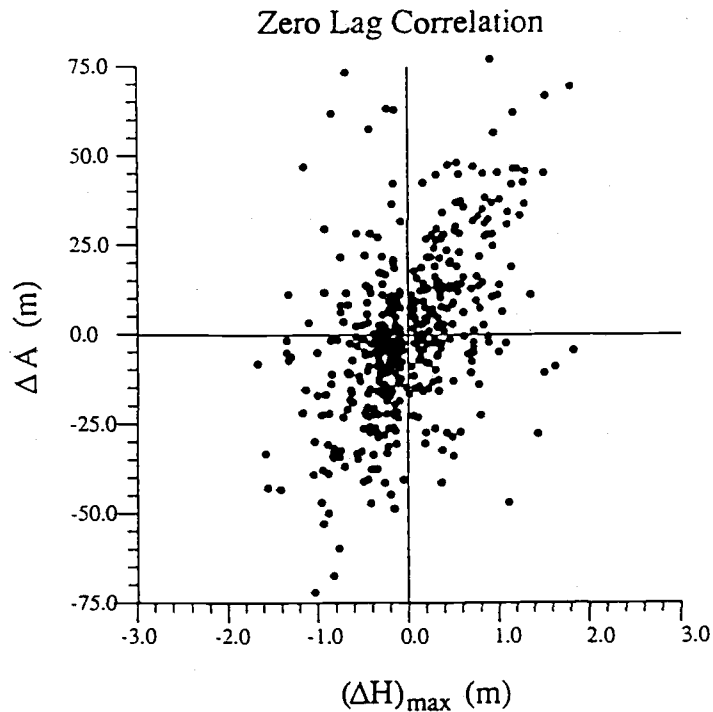
determine which movement is more important in the correlation. We test the relative contributions of increasing and decreasing wave heights by plotting $\Delta A(t)$ vs. $(\Delta H_s)_{\max}$ (Figure 12b) for the highest correlation ($r=0.48$ at zero lag, Figure 12a), where $(\Delta H_s)_{\max}$ is defined as the largest change in H_s over the preceding 24 hours. These results appear to indicate that the strong significant correlation at zero lag is not dominated by either onshore or offshore migration. However, correlation coefficients for data corresponding to positive $(\Delta H_s)_{\max}$ ($r=0.61$) is nearly twice as high as for negative $(\Delta H_s)_{\max}$ ($r=0.36$), indicating that offshore response is more well behaved than onshore response.

Associations between three-dimensional variability and incident wave conditions are investigated with cross-correlations between $V(t)$ and H_s (Figure 13). The negative correlation at zero lag ($r=-0.19$) indicates that $V(t)$ is inversely related to incident wave energy. This is consistent with results from the previous section showing that under high waves bars rapidly become linear. Positive correlations ($r=0.12-0.16$) at negative lags associated with H_s leading, indicate that large scale three-dimensional bar structure tends to evolve 5-7 days after large wave events. The negative correlations ($r=0.16-0.21$) at short positive lags (less than two days) arise from the fortuitous result that additional increases in wave energy may occur after the bar has already become linear (no longshore variability).

Interestingly, cross correlations with $\Delta V(t)$ and ΔH_s did not yield significant correlations (Figure 14), nor did analysis with other changes in wave parameters (Appendix B). This is not entirely unexpected, though, considering that evolution of three-dimensionality may involve more complicated processes.



a)



b)

Figure II - 12. a) Cross correlation diagram showing $\Delta A(t)$ vs. $(\Delta H_s)_{\max}$ for lags out to ± 14 days. The negative lags indicate $(\Delta H_s)_{\max}$ leading. The 95% confidence intervals (dashed lines) were calculated using the long-lag artificial skill method after Davis, 1976. b) Plot of $\Delta A(t)$ (abscissa) vs. $(\Delta H_s)_{\max}$ (ordinate) for the maximum correlation observed at zero lag.

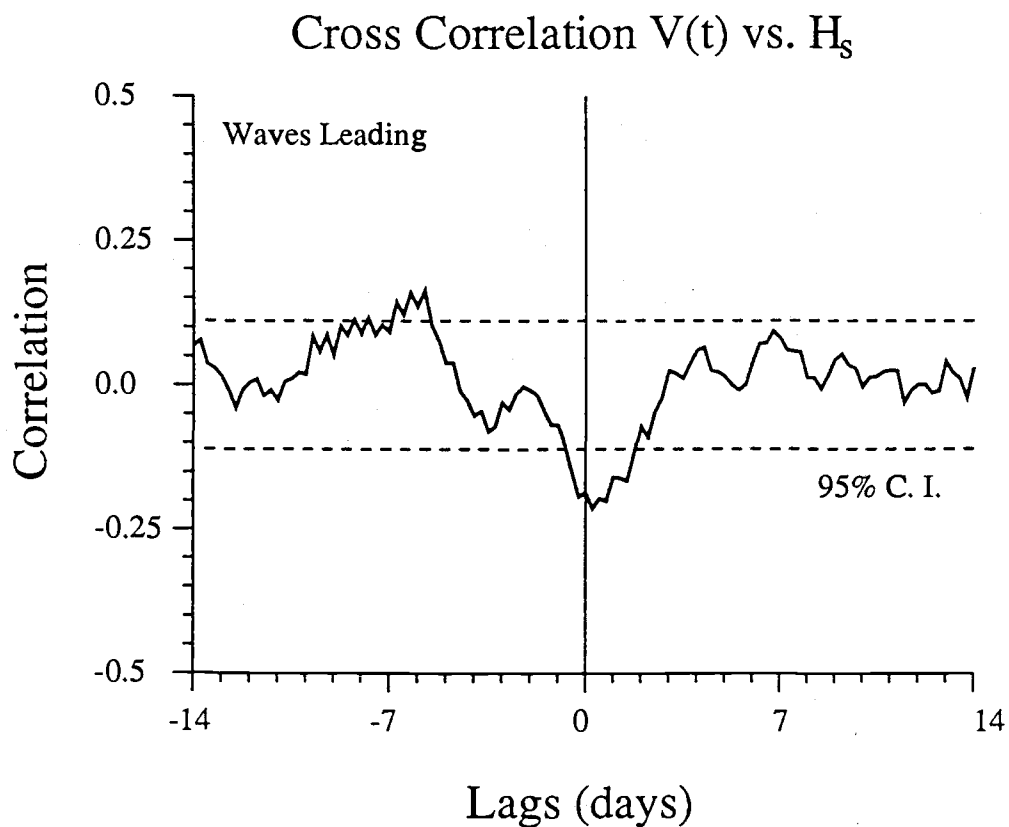


Figure II - 13. Cross correlation $V(t)$ vs. H_s for lags out to ± 14 days. The negative lags indicate H_s leading. The 95% confidence intervals (dashed lines) were calculated using the long-lag artificial skill method after Davis, 1976.

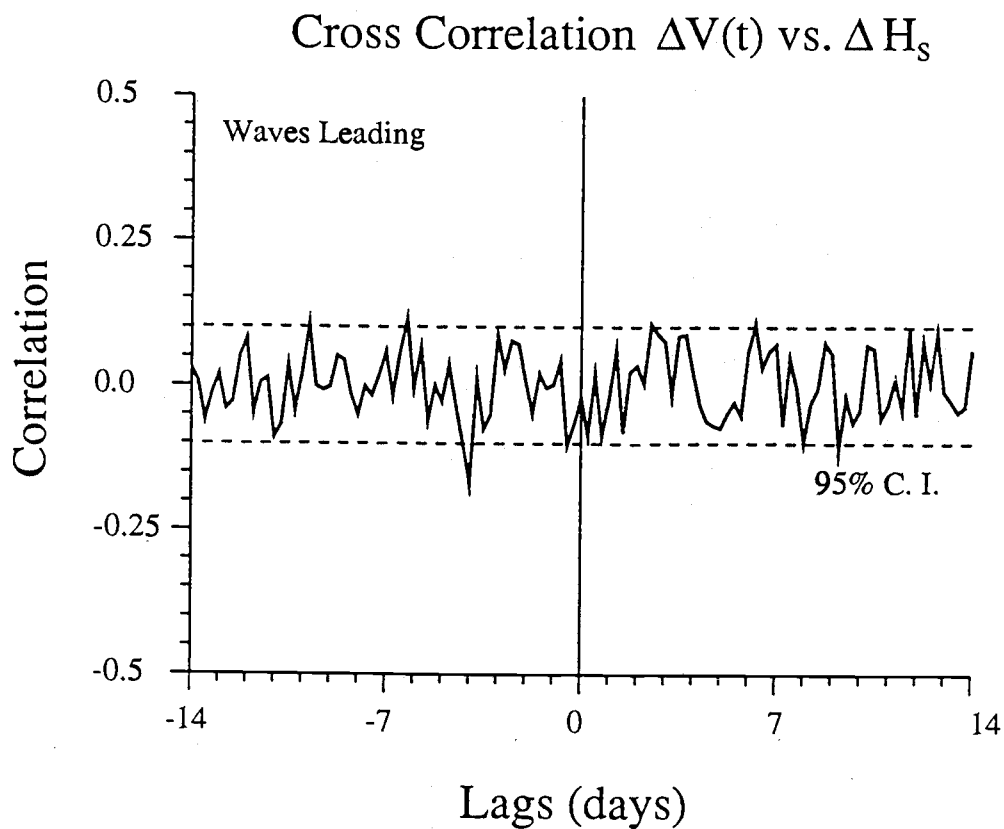


Figure II - 14. Cross correlation $\Delta V(t)$ vs. ΔH_s for lags out to ± 14 days. The negative lags indicate ΔH_s leading. The 95% confidence intervals (dashed lines) were calculated using the long-lag artificial skill method after Davis, 1976.

DISCUSSION

The bar types defined in the the classification scheme (Figure 1) are unique and encompass the range of possible morphologies from fully dissipative to fully reflective. The model is similar to the previous classification scheme of Wright and Short (1984), with the most obvious differences indicated by two new bar types which serve to more uniquely define each state by better identifying longshore variability in bar morphology. These distinctions are valuable when describing bar changes or investigating the formation of longshore variability.

The classification process is made objective by removing as much interpretive bias (associated with visual image analysis) as possible, an improvement over previous interpretive methods. This is done by defining four basic classification criteria (Table 1) which form a set of binary decisions that uniquely define each bar type (Figure 2). Some of the decisions, such as the presence of coherent longshore rhythmicity and bar scaling, may be directly related to processes influencing bar formation (beyond the scope of this paper).

Transitional sequences observed in the data indicate that the progression down the model from higher to lower bar types occurs sequentially and is associated with declining wave conditions, thus representing an accretional progression. Transitions to higher states occur sporadically under rising wave conditions, and thus represent an erosional sequence. We found, surprisingly, that morphology correlates best with simple offshore wave height. This is somewhat inconvenient, though, since non-dimensional surf similarity parameters can be more easily applied to and compared with other field sites.

The transition from a linear to a longshore variable morphology is of particular interest in addressing bar genesis. In the past, quantifying linearity in bar form has proved to be a difficult task, exacerbated by the ambiguity in defining bar morphology under adverse conditions. With our sampling technique, linear bars (as well as longshore

variable bars) are relatively easy to identify under all wave conditions (provided breaking occurs over the bar). Our observations show that linear bars (*Bar Type G*) tend to predominate (exclusively) during storms. Rapid development of three-dimensional structure follows the decline of wave energy, indicating that linear bars are unstable ($\langle\tau_G\rangle \approx 2$ days) and are only maintained under high waves.

Non-rhythmic bars are also transient ($\tau_C \approx \tau_F \approx 3$ days), irrespective of shoreline attachment points. These bars occur under a wide range of conditions, although they are usually associated with a change in wave height, suggesting that this morphology is also very unstable. Those with continuous troughs (*Bar Type F*) generally occur immediately after linear bars and prior to the formation of dominant longshore periodicity, suggesting that they fit a natural progression between differing levels of three-dimensionality. Conversely, those with shore attachments (*Bar Type C*) do not appear to fit regular sequences, suggesting that the processes controlling this morphology are unclear, although, it may be associated with the presence of sporadically placed rip currents seen in the raw video records.

The formation of longshore rhythmicity has major implications in bar evolution, and has been a primary objective of intensive short-term field studies focused on single storm events (Sallenger, et al., 1985; Howd and Birkemeier, 1987). We observe rhythmic bars (*Bar Types D and E*) to occur typically 5-16 days following the peaks of storms, though response times may be much quicker (on the order of 1-2 days). Once well-developed, they tend to be very stable under moderate waves, with residence times increasing with proximity to the shoreline ($\tau_E \approx 5$ days, $\tau_D \approx 11$ days). This is observed in bars that maintain their longshore structure when slowly migrating onshore under low waves, but rapidly degrading with onset of high waves. Rhythmic bars (most often crescentic bars) are very common at this field site, indicating that this morphology may be the preferred morphologic configuration.

The parameterization of both the mean cross-shore bar migration (two-dimensional component) and the evolution of longshore variability (three-dimensional component) is successfully accomplished due to the quantitative nature of the time exposure technique in estimating bar crest position. As an analytic method, empirical orthogonal functions work because the data mean is linear (and homogeneous alongshore) and one spatial factor (in this case the first) is linear, thus isolating the variance of the mean cross-shore movement. As before, the most interesting results are those associated with storm events, and are supportive of the previous classification results.

We find that the development of two-dimensional morphology (no longshore variability) occurs very rapidly, on the order of less than one day, following increases in wave energy. Conversely, transitions to three-dimensional morphologies occur following wave decreases. Visual assessment of morphology shows that initial formation of longshore variability may be quite rapid, commonly less than one day after the peak of high wave events. Continued periods of low wave energy generally result in the formation of large scale three-dimensionality, with time scales of 5-7 days, consistent with recent short-term field results (Sallenger, et al., 1985; Howd and Birkemeier, 1987).

A more accurate estimation of the time scale for initial formation of three-dimensionality is not possible with this data set (since our maximum morphologic resolution is one day). We find that changes in wave height do not correlate (at the 95% significance level) with the formation of longshore variability. This is expected considering the complex dynamical processes thought to be important in controlling nearshore topography. It is interesting to note, though, that coherent longshore structure observed in bars typically have very large length scales on the order of hundreds of meters, lending support to models incorporating low frequency (infragravity band) motions with similar length scales.

The results are clear in their indication that long records are invaluable in assessing the morphologic behavior of sand bars. Predictability is not likely using just incident wave

parameters, though a general understanding of transitional sequences with respect to large storm events is possible with long data records. Short-term intensive experiments investigating other fluid motions (such as edge waves) are necessary to address bar genesis. This study presents evidence that these experiments should be concentrated around storm events when three-dimensional bar morphology is rapidly evolving.

Special mention concerning errors in the time series, $A(t)$ and $V(t)$, arising from tidal fluctuations (mentioned earlier) is appropriate since this is the first instance the time exposure technique has been applied over an extended period. As expected, the time series show a systematic correlation (though not significant for 95% confidence) resulting from tidal fluctuations (aliased into a ~ 15 day period). This signal would at first appear to increase the variance of $A(t)$. However, discrepancies in offshore bar crest estimations (away from the true position) are not solely the result of the tide since the tide does not change dramatically between day-to-day samples (taken at approximately the same time). In fact, most short-term variation (order of 1-2 days) in the data is associated with changing incident wave height. Therefore, removing the insignificant systematic long-lag correlations would inevitably result in the introduction of significant tidal contamination at zero lag, the time scale of highest interest. Hence, our main concern is associated with the maximum offshore discrepancy. This magnitude was estimated by regressing $A(t)$ against the measured tidal signal (relative to MSL), and found to be 13.5m, within our estimated error for the technique (~ 15 m).

$V(t)$ also shows an apparent systematic signal associated with tidal fluctuations. We note, though, that the nature of this noise is not the same as for $A(t)$. The affect of the tide on the estimation of longshore bar variability is explained in LH89. The major point is that at lower water levels, maximum wave dissipation occurs further offshore where longshore variability of contours may be less. This could serve to reduce the estimated longshore variance in bar crest position, and would tend to have higher affects at lower water levels (LH89). However, our main interest is with changes over short time scales

(order days), much less than the tidal signal (~15 days), and so the effect on longshore variability estimation is minimized.

CONCLUSIONS

A two year dataset of daily sand bar morphology estimates has been collected on a naturally barred beach at Duck, N.C. Daily time exposure images allow improved assessment of overall morphology as well as quantitative estimates of bar crest position as a function of longshore location. Significant wave height and peak period data provided environmental control. Analyses follow two lines. First, bar samples are visually identified using four morphologic classification criteria. Secondly, using empirical orthogonal functions (EOF's), the variability in bar structure is split into two-dimensional (linear) and three-dimensional (longshore variable) components.

A new eight bar type classification scheme is presented that represents the morphologic variability of nearshore sand bars observed at the field site. Four binary (one is actually tertiary) classification criteria are chosen, each of which may be related to processes associated with models of bar generation. The classification provides a complete set of morphologic bar types in which each state is defined uniquely (every beach morphology is described by one and only one state). Calibration studies show that operator subjectivity is small.

The most common bar form is longshore-periodic (rhythmic) bars observed in 68% of the data. Analysis reveals that linear bars occur under highest wave conditions ($\bar{H}_s = 1.78\text{m}$) and are unstable (mean residence time ≈ 2 days), whereas shore-attached crescentic bars are the most stable (mean residence time ≈ 11 days) and generally form 5-16 days following peak wave events. Non-rhythmic, three-dimensional bars are very transient (mean residence time ≈ 3 days). The classification scheme shows qualitatively good correlations between bar type transitions and incident wave parameters. Furthermore, the ordering of the bar types yields a good first order approximation of accretional and erosional sequences. Transitions to progressively more stable bars generally occur sequentially (89%) under declining wave conditions, while transitions to higher states are

more sporadic (49.5% are one-step) and occur under rising wave energy, with higher jumps in state resulting from larger increases in wave energy.

Bar samples are also digitized to yield quantitative estimates of bar crest position and longshore variability. Principal component analysis was used to decompose the data into two-dimensional (linear) and three-dimensional (longshore variable) components. Cross-shore bar migration dominates bar variability (accounting for 74.6% of the variance), and rapidly responds to changing wave conditions (with time scales less than one day). Longshore bar structure accounts for ~14% of the variance, where the remaining variance is associated with errors, partly a result of tidal contamination arising from the sampling technique. Three-dimensional bar structures evolve rapidly, with changes in longshore variability inversely related to changing wave conditions. The evolution to coherent longshore periodicity occurs 5-7 days following the peak of high energy storm events.

REFERENCES

- Aubrey, D. G., Seasonal patterns of onshore/offshore sediment movement, *J. Geophys. Res.*, 84, 6347-6354, 1979.
- Aubrey, D. G., Inman, D. L. and C. D. Winant, The statistical prediction of beach changes in Southern California, *J. Geophys. Res.*, 85, 3264-3276, 1980.
- Aubrey, D. G. and R. M. Ross, The quantitative description of beach cycles, *Mar. Geol.*, 69, 155-170, 1985.
- Battjes, J.A., Set-up due to irregular waves, in *Proceedings of the 13th Conference on Coastal Engineering, 1993-2004*, American Society of Civil Engineers, New York, 1972.
- Battjes, J. A. and J. P. F. M. Janssen, Energy loss and set-up due to breaking of random waves, in *Proceedings of the 16th Conference on Coastal Engineering*, p. 569, American Society of Civil Engineers, New York, 1978.
- Birkemeier, W. A. and C. Mason, The CRAB: a unique nearshore surveying vehicle, *J. Surv. Eng.*, 110(1), 1-7, American Society of Civil Engineers, New York, 1978.
- Birkemeier, W. A., Time scales of nearshore profile change, in *Proceedings of the 19th Conference on Coastal Engineering*, pp. 1507-1521, American Society of Civil Engineers, New York, 1985a.
- Birkemeier, W. A., et. al., User's guide to CERC's Field Research Facility, Instruction Report CERC-85-1, U. S. Army Engineer Waterways Experiment Station, Vicksburg, MS, 1985b.
- Birkemeier, W. A., Baron, C. F., Leffler, M. W., Miller, H. C., Strider, J. B. and K. K. Hathaway, SUPERDUCK Nearshore Processes Experiment; Data summary, CERC Field Research Facility, Misc. Report, Waterways Exp. Station, 1989a.
- Birkemeier, W. A., P. A. Howd and J. M. Smith, Long-term Measurements of beach and nearshore changes, in progress, 1989b.
- Bowen, A. J., Simple models of nearshore sedimentation: beach profiles and longshore bars, in S.B. McCann (Editor), *Coastline of Canada, Littoral Processes and Shore Morphology*, *Geol. Surv. Can., Pap.*, 80-10, 1-11, 1980.
- Bowen, A. J. and D. L. Inman, Edge waves and crescentic bars, *J. Geophys. Res.*, 76, 8662-8671, 1971.

- Carter, T. G., Liu, P. L. and C. C. Mei, Mass transport by waves and offshore sand bedforms, *J. Waterways, Harbors, Coastal Engineering Division*, 165-184, American Society of Civil Engineers, New York, 1973.
- Chappell, J. and I. G. Eliot, Surf-beach dynamics in time and space - an Australian case study, and elements of a predictive model, *Mar. Geol.*, 32, 231-250, 1979.
- Collins J. I., Probabilities of breaking wave characteristics, in *Proceedings of the 13th Conference on Coastal Engineering*, 399-412, American Society of Civil Engineers, New York, 1970.
- Crowson, R. A., Birkemeier, W. A., Klein, H. M. and H. C. Miller, SUPERDUCK nearshore processes experiment: summary of studies, CERC Field Research Facility, Tech. Paper, U. S. Army Corps of Engineer Waterways Experiment Station, Vicksburg MS, 1988.
- Davis, R. E., Predictability of sea surface temperature and sea level pressure anomalies over the North Pacific Ocean, *J. Phys. Oceanogr.*, 6, 249-266, 1976.
- Dean, R. G., Heuristic models of sand transport in the surf zone, *in Proceedings of the Conference on Coastal Engineering Dynamics in the Surf Zone*, Sydney, N. S. W., 208-214, 1973.
- Galvin, C. J., Jr., and P. S. Eagleson, Experimental study of longshore currents on a plane beach, Tech. Memo. 10, U.S. Army Coastal Eng. Res. Center, Fort Belvoir, Va., 1965.
- Goda, Y., Irregular wave deformation in the surf zone, *Coast. Eng. Jpn.*, 18, 13-26, 1975.
- Goldsmith, V., Bowman, D. and K. Kiley, Sequential Stage development of crescentic bars: Hohaterim beach, Southeastern Mediterranean, *J. Sed. Petrol.*, 52, 233-249, 1982.
- Greenwood, B. and R. G. D. Davidson-Arnott, Marine bars and nearshore sedimentary processes, Kouchibouguac Bay, New Brunswick, Canada, *in Hails, J. R., and Carr, A., eds., Nearshore Sediment Dynamics and Sedimentation: New York, Wiley, p. 123-150, 1979.*
- Guza, R. T. and D. I. Inman, Edge waves and beach cusps, *J. Geophys. Res.*, 86, 6442-6450, 1975.
- Harris, W. D. and M. J. Umbach, Underwater mapping, *Photogrammetric Engineering*, 34, 765-772, 1972.

- Holman, R. A. and A. J. Bowen, Bars, bumps, and holes: models for the generation of complex beach topography, *J. Geophys. Res.*, 87, 457-468, 1982.
- Holman, R. A. and A. H. Sallenger, Setup and swash on a natural beach, *J. Geophys. Res.*, 90, 945-953, 1985.
- Holman, R. A. and A. H. Sallenger, Jr., High-Energy Nearshore Processes, *EOS Transact., American Geophysical Union*, 67, 1369-1371, 1986.
- Holman, R. A. and T. C. Lippmann, 1987. Remote sensing of nearshore bar systems - making morphology visible, *Proceedings of the 20th Conference on Coastal Engineering*, 929-944, American Society of Coastal Engineers, New York, 1987.
- Howd, P. A. and W. A. Birkemeier, Beach and nearshore survey data: 1981-1984, CERC, Field Research Facility, Tech. Report CERC 87-89, U. S. Army Engineer Waterways Experiment Station, Vicksburg, MS, 1987a.
- Howd, P. A. and W. A. Birkemeier, Storm induced morphology changes during DUCK85, in *Proceedings of Coastal Sediments '87*, ASCE, pp. 834-847, 1987b.
- Hunt, I. A., Design of seawalls and breakwaters, *Proc. Am Soc. Civ. Eng.*, 85, 123-152, 1959.
- Hwang, L.-S. and D. Divoky, Breaking wave set-up and decay on gentle slopes, in *Proceedings of the 12th Conference on Coastal Engineering*, 377-389, American Society of Coastal Engineers, New York, 1970.
- Huntley, D. A., Guza, R. T. and E. B. Thornton, Field observations of surf beat, 1, Progressive edge waves, *J. Geophys. Res.*, 86, 6451-6466, 1981.
- Keulegan, G. H., An Experimental study of submarine sand bars, U.S. Army Corps of Engineers, Beach Erosion Board, Tech. Memo., 3, 40 pp., 1948.
- Komar, P. D., *Beach processes and sedimentation*, Prentice-Hall, Englewood Cliffs, N. J., 1976.
- Kuo, C. T. and S. T. Kuo, Effect of wave breaking on statistical distribution of wave heights, *Proc. Civ. Eng. Oceans*, 3, 1211-1231, 1974.
- Lau, J. and B. Travis, Slowly varying Stokes waves and submarine longshore bars, *J. Geophys. Res.*, 78, 4489-4497, 1973.
- Lippmann, T. C. and R. A. Holman, Quantification of sand bar morphology: A video technique based on wave dissipation, *J. Geophys. Res.*, 94, 995-1011, 1989.

- Lundall, A. C., Underwater depth determination by aerial photography, *Photogrammetric Engineering*, 14, 454-462, 1948.
- Mason, C., Birkemeier, W. A. and P. A. Howd, Overview of DUCK85 nearshore processes experiment, in *Proceedings of the 20th Conference on Coastal Engineering*, 818-833, American Society of Coastal Engineers, New York, 1987.
- McCowan, J., On the solitary wave, *Philos. Mag., J. Sci.*, 32, 45-58, 1891.
- Miller, R. L., Role of vortices in surf zone prediction: Sedimentation and wave forces, beach and nearshore sedimentation, *Spec. Publ. 24, Soc. of Econ. Paleontol. and Minerals*, Washington, D.C., 1976.
- Okamoto, A., Wave influence in two media photogrammetry, *Photogrammetric Engineering*, 48, 1487-1499, 1982.
- Oltman-Shay, J. and R. T. Guza, Infragravity edge wave observations on two California beaches, *J. Phys. Ocean.*, 17, 644-663, 1987.
- Priesendorfer, R. W., Zwiers, F. W. and T. P. Barnett, Foundations of principal component selection rules, *SIO Report 81-4*, 200pp., 1981.
- Sallenger, A. H., Holman, R. A. and W. A. Birkemeier, Storm-induced response of a nearshore-bar system, *Mar. Geol.*, 64, 237-257, 1984.
- Shepard, F. P., Longshore bars and troughs, U.S. Army Corps of Engineers, Beach Erosion Board, *Tech. Memo*, 15, 31 pp., 1950.
- Short, A. D., Three dimensional beach-stage model, *J. Geol.*, 87, 553-571, 1975.
- Sonu, C. J., Three-dimensional beach changes, *J. Geol.*, 81, 42-64, 1973.
- Sonu, C. J. and W. R. James, A Markov model for beach profile changes, *J. Geophys. Res.*, 78, 1462-1471, 1973.
- Sonu, C. J. and J. L. van Beek, Systematic beach changes on the Outer Banks, North Carolina, *J. Geol.*, 79, 416-425, 1971.
- Stoker, J. J., *Water Waves*, Interscience, New York, 1957.
- Sunamura, T., Beach morphologies and their change, in K. Horikawa (Editor), *Nearshore Dynamics and Coastal Processes: Theory, Measurement, and Predictive Models*, University of Tokyo Press, 136-152, 1988.
- Thornton, E. B. and R. T. Guza, Energy saturation and phase speeds measured on a natural beach, *J. Geophys. Res.*, 87, 9499-9508, 1982.

- Thornton, E. B. and R. T. Guza, Transformation of wave height distribution, *J. Geophys. Res.*, 88, 5925-5938, 1983.
- Thornton, E. B. and R. T. Guza, Surf zone currents and random waves: Field data and models, *J. Phys. Ocean.*, 16, 1165-1178, 1986.
- Wiegel, R. L., Recognition of underwater obstructions from aerial photography, Wave Project Report No. HE-116-248, University of California, Berkely, 32 pp., 1947.
- Wright, L. D., Chappell, J., Thom, B. G., Bradshaw, M. P. and P. Cowell, Morphodynamics of reflective and dissipative beach and inshore systems: Southeastern Australia, *Mar. Geol.*, 32, 105-140, 1979.
- Wright, L. D. and A. D. Short, Morphodynamics of beaches and surf zones in Australia, in P. D. Komar (editor), *CRC Handbook of Coastal Processes and Erosion*, CRC Press, Boca Raton, Fla., 35-64, 1983.
- Wright, L. D. and A. D. Short, Morphodynamic variability of surf zones and beaches: a synthesis, *Mar. Geol.*, 56, 93-118, 1984.
- Wright, L. D., Short, A. D. and M. O. Green, Short-term Changes in the morphodynamic states of beaches and surf zones: an empirical predictive model, *Mar. Geol.*, 62, 339-364, 1985.
- Wright, L. D., P. Nielsen, N. C. Shi and J. H. List, Morphodynamics of a bar trough surf zone, *Marine Geology*, 70, 251-285, 1986.

APPENDICES

APPENDIX A:
TRANSITION TABLES

Table A - 1. \overline{P}_Q ($\times 10^{-3}$, bold) and $\overline{\Delta P}_0$ for each transition. Initial states are along the top and resulting states are listed on the left.

		FROM								
		A	B	C	D	E	F	G	H	
T O D	E R O S I O N ↑	H	+
	G	.	3.25* +2.98	2.82* +2.50	2.93 +2.05	4.17 +3.40	2.73 +0.02	+	.	.
	F	.	.	2.32* +1.50	1.83 +0.54	2.25 +1.74	+	2.39 -0.38	.	.
	E	.	.	.	1.49 +0.05	+	1.06 -1.03	0.76* -4.00	.	.
	D	.	0.87* +0.59	0.85 -0.06	+	1.23 +0.11	.	3.73* -2.60	.	↓ A C C R E T I O N
	C	.	.	+	0.93 +0.37	5.36* +2.21	0.49* +0.03	.	.	.
	B	.	+	.	0.23 +0.00
	A	+

*Computed from less than 3 transitions.

Table A - 2. $\overline{H_0/L_0}$ ($\times 10^2$, bold) and $\overline{\Delta H_0/L_0}$ for each transition. Initial states are along the top and resulting states are on the left.

		FROM								
		A	B	C	D	E	F	G	H	
T O D E S I O N	E R O S I O N	H	+
		G	.	0.80* -0.08	2.92* +2.53	2.64 +1.46	1.78 +0.57	1.75 +0.62	+	.
		F	.	.	2.82* +1.41	1.79 +0.98	1.83 +0.53	+	0.99 -0.82	.
		E	.	.	.	0.78 -0.37	+	1.38 +0.05	0.39* -0.65	.
		D	.	1.75* +1.14	2.61 +1.87	+	1.33 +0.42	.	0.76* -1.96	.
		C	.	.	+	1.71 +0.21	2.83* +0.24	0.47* +0.01	.	.
		B	.	+	.	0.45 -0.13
		A	+
		A C C R E T I O N								

*Computed from less than 3 transitions.

Table A - 3. $\overline{H_g/T}$ ($\times 10^{-1}$, bold) and $\overline{\Delta H_g/T}$ for each transition. Initial states are along the top and resulting states are on the left.

		FROM								
		A	B	C	D	E	F	G	H	
T O D	E R O S I O N ↑	H	+
	G	.	1.45* +0.60	3.07* +2.49	2.78 +1.52	2.29 +1.08	1.63 +0.41	+	.	.
	F	.	.	2.89* +1.48	1.91 +0.82	1.96 +0.78	+	1.42 -0.66	.	.
	E	.	.	.	1.08 -0.28	+	1.37 -0.29	0.70* -1.11	.	.
	D	.	1.71* +0.99	2.13 +1.09	+	1.45 +0.30	.	1.38* -1.60	.	↓
	C	.	.	+	1.25 +0.28	3.43* +0.55	0.72* +0.02	.	.	.
	B	.	+	.	0.61 -0.04
	A	+
									A C C R E T I O N	

*Computed from less than 3 transitions.

APPENDIX B:**CROSS-CORRELATIONS**

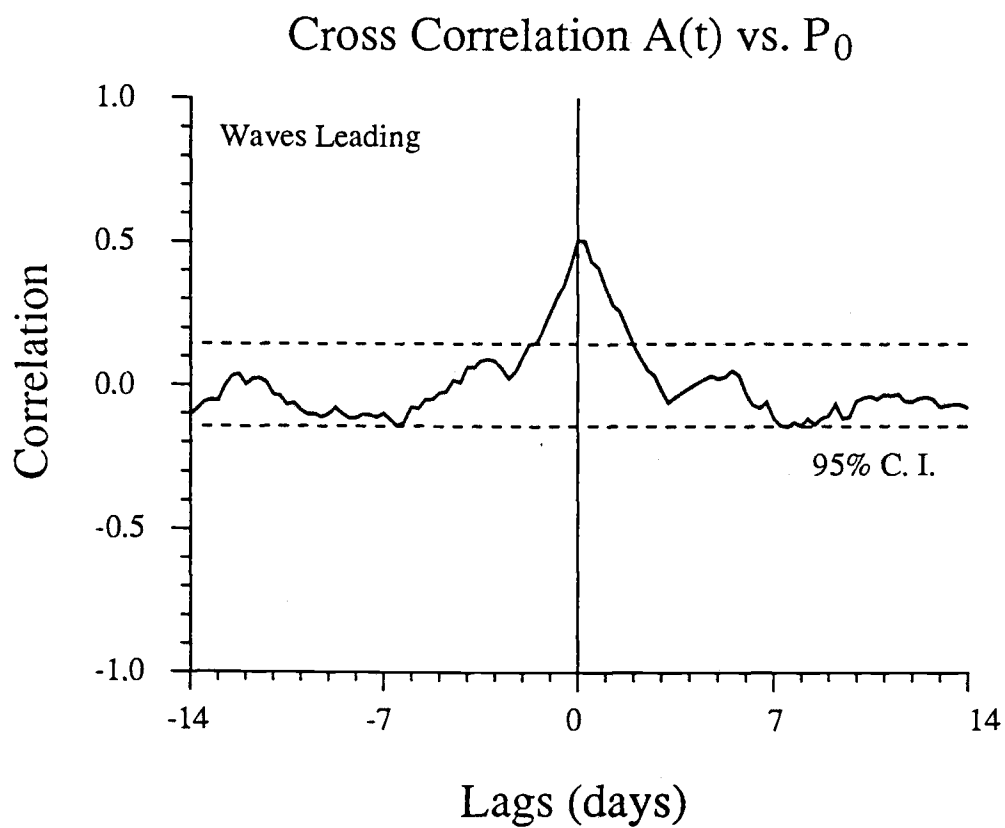


Figure B - 1. Cross correlation A(t) vs. P₀ for lags out to +/-14 days. The negative lags indicate waves leading. The 95% confidence intervals (dashed lines) were calculated using the long-lag artificial skill method after Davis, 1976.

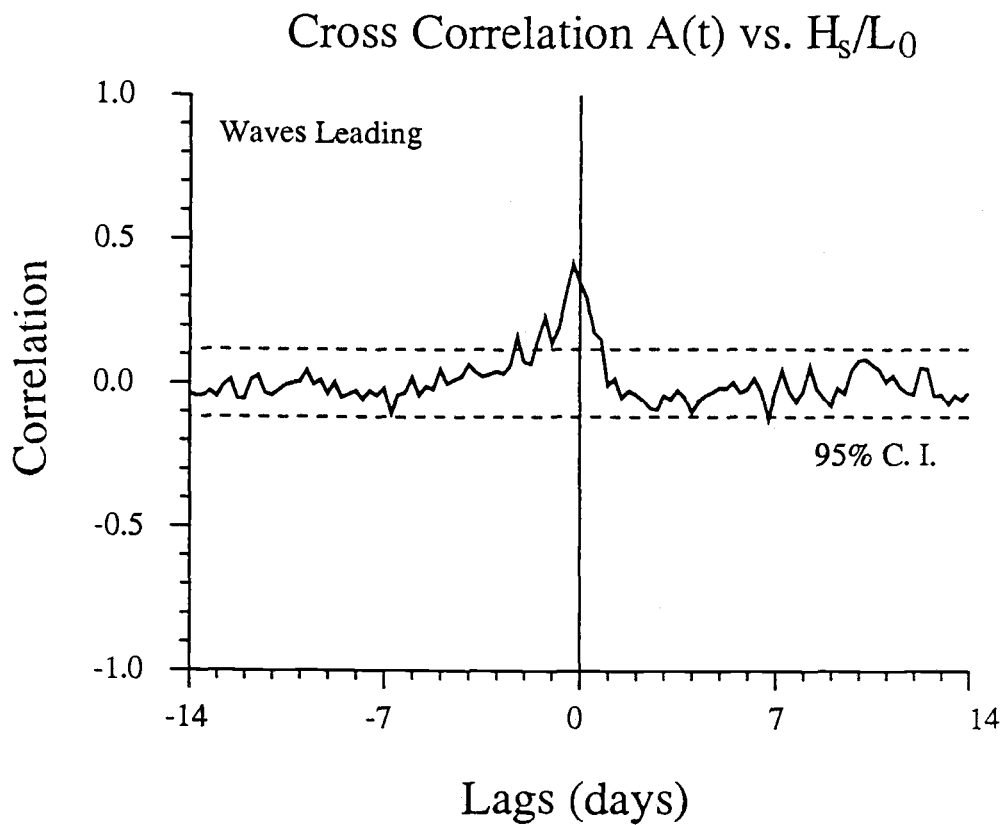


Figure B - 2. Cross correlation $A(t)$ vs. H_s/L_0 for lags out to ± 14 days. The negative lags indicate waves leading. The 95% confidence intervals (dashed lines) were calculated using the long-lag artificial skill method after Davis, 1976.

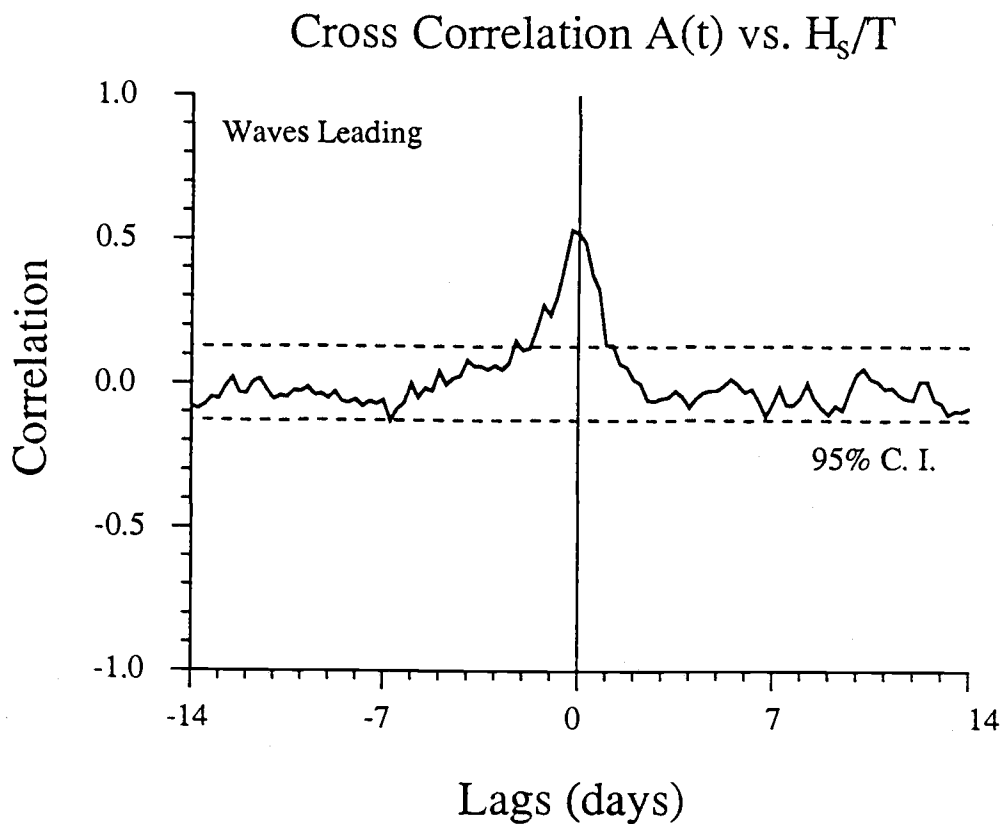


Figure B - 3. Cross correlation A(t) vs. H_s/T for lags out to +/-14 days. The negative lags indicate waves leading. The 95% confidence intervals (dashed lines) were calculated using the long-lag artificial skill method after Davis, 1976.

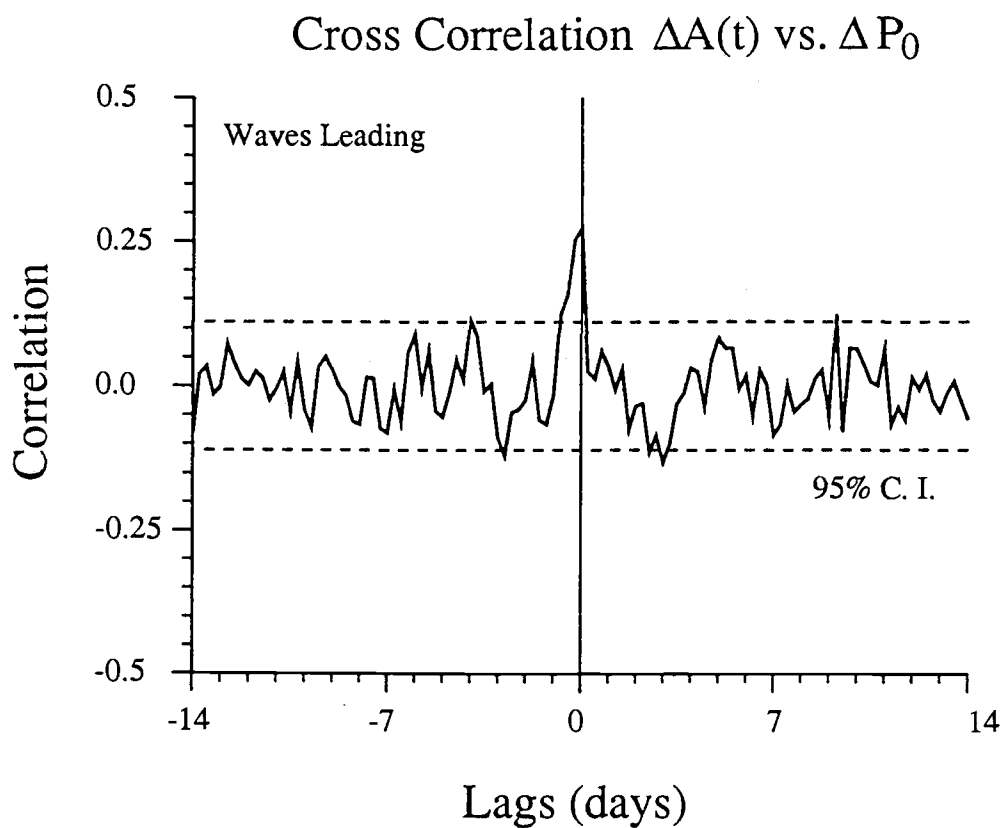


Figure B - 4. Cross correlation $\Delta A(t)$ vs. ΔP_0 for lags out to ± 14 days. The negative lags indicate waves leading. The 95% confidence intervals (dashed lines) were calculated using the long-lag artificial skill method after Davis, 1976.

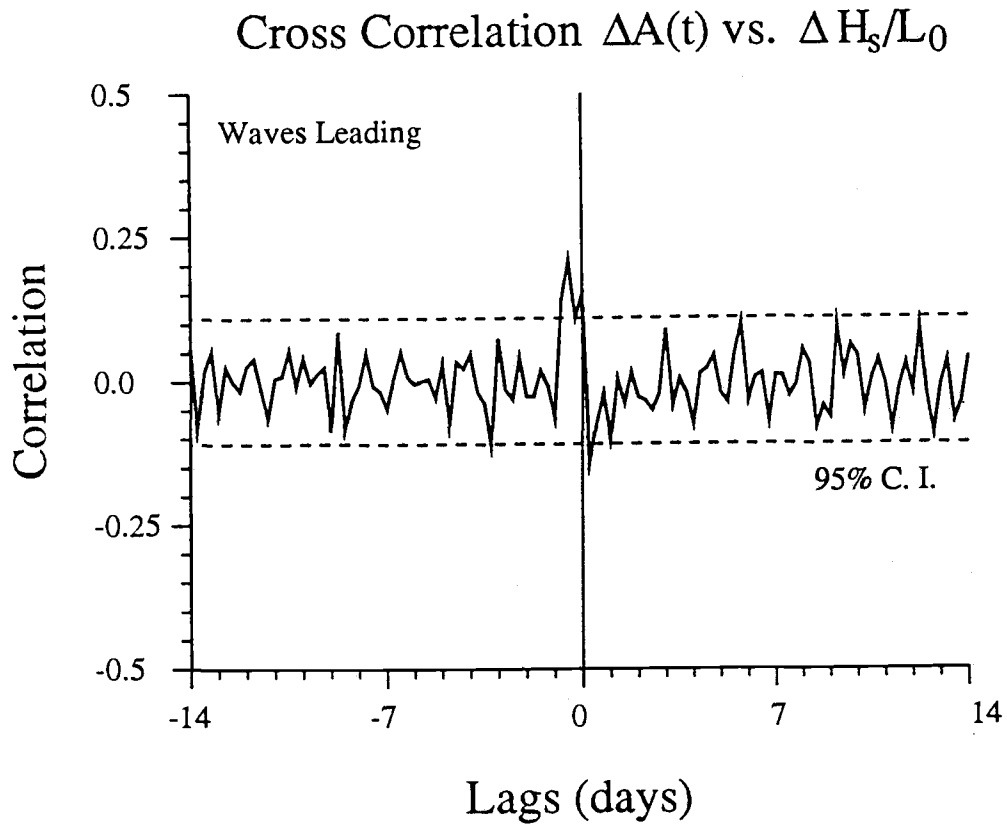


Figure B - 5. Cross correlation $\Delta A(t)$ vs. $\Delta H_s/L_0$ for lags out to ± 14 days. The negative lags indicate waves leading. The 95% confidence intervals (dashed lines) were calculated using the long-lag artificial skill method after Davis, 1976.

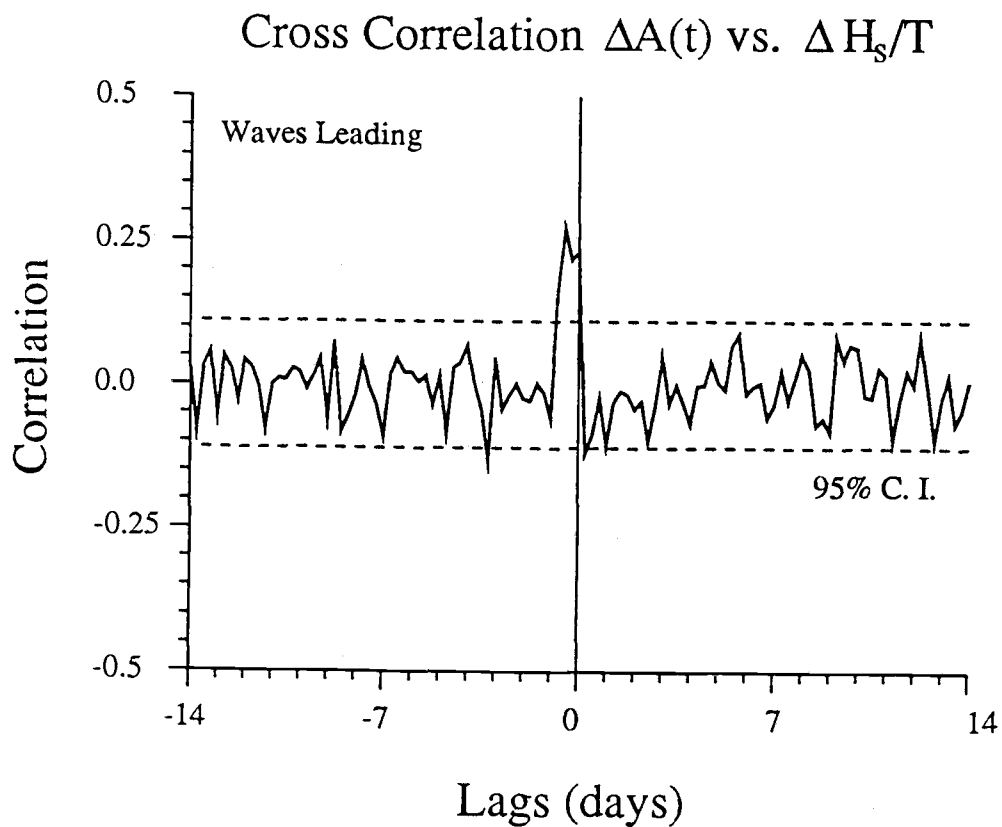


Figure B - 6. Cross correlation $\Delta A(t)$ vs. $\Delta H_s/T$ for lags out to ± 14 days. The negative lags indicate waves leading. The 95% confidence intervals (dashed lines) were calculated using the long-lag artificial skill method after Davis, 1976.

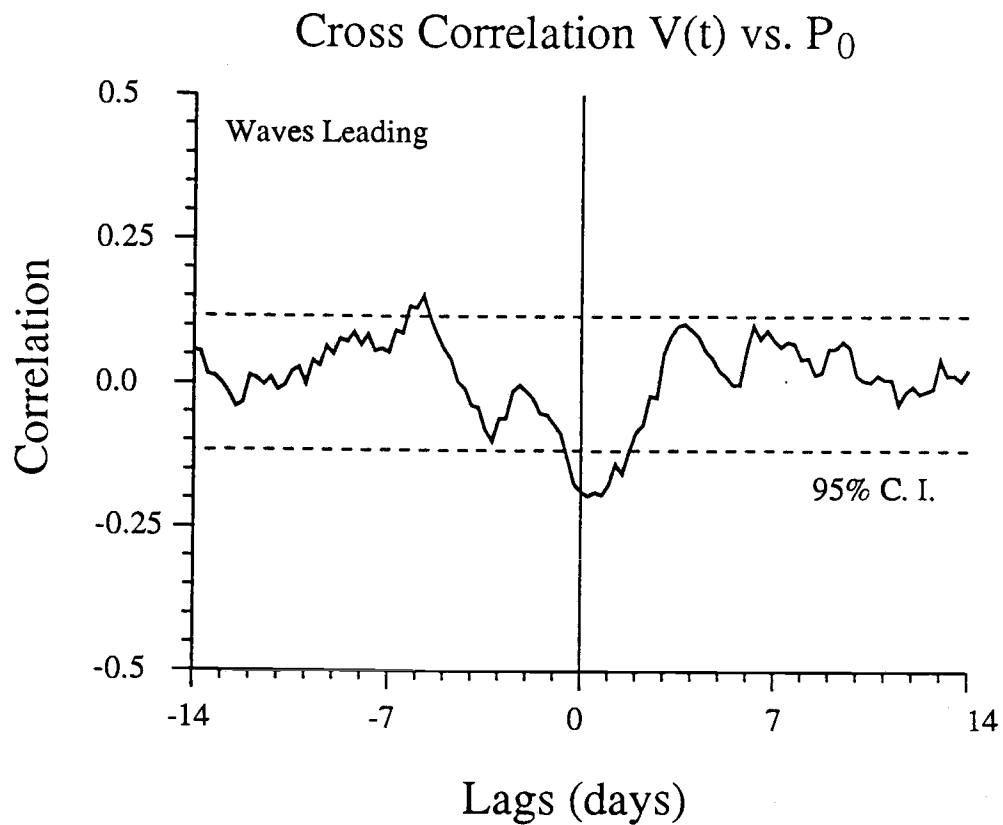


Figure B - 7. Cross correlation $V(t)$ vs. P_0 for lags out to ± 14 days. The negative lags indicate waves leading. The 95% confidence intervals (dashed lines) were calculated using the long-lag artificial skill method after Davis, 1976.

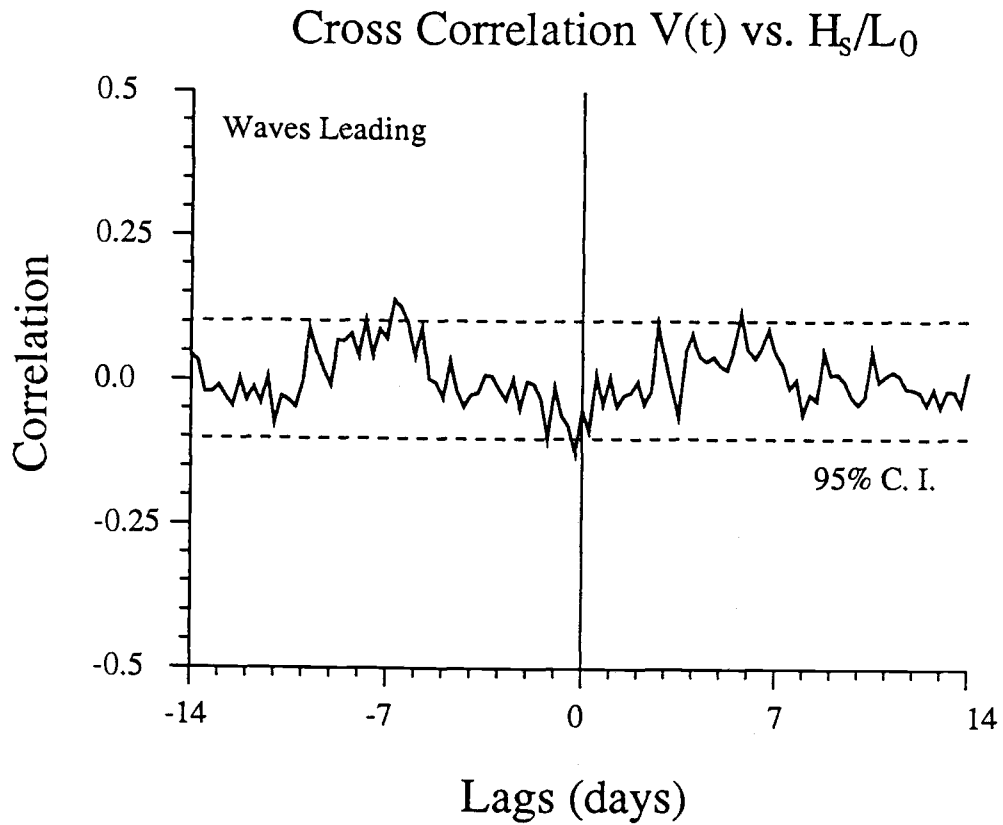


Figure B - 8. Cross correlation $V(t)$ vs. H_s/L_0 for lags out to ± 14 days. The negative lags indicate waves leading. The 95% confidence intervals (dashed lines) were calculated using the long-lag artificial skill method after Davis, 1976.

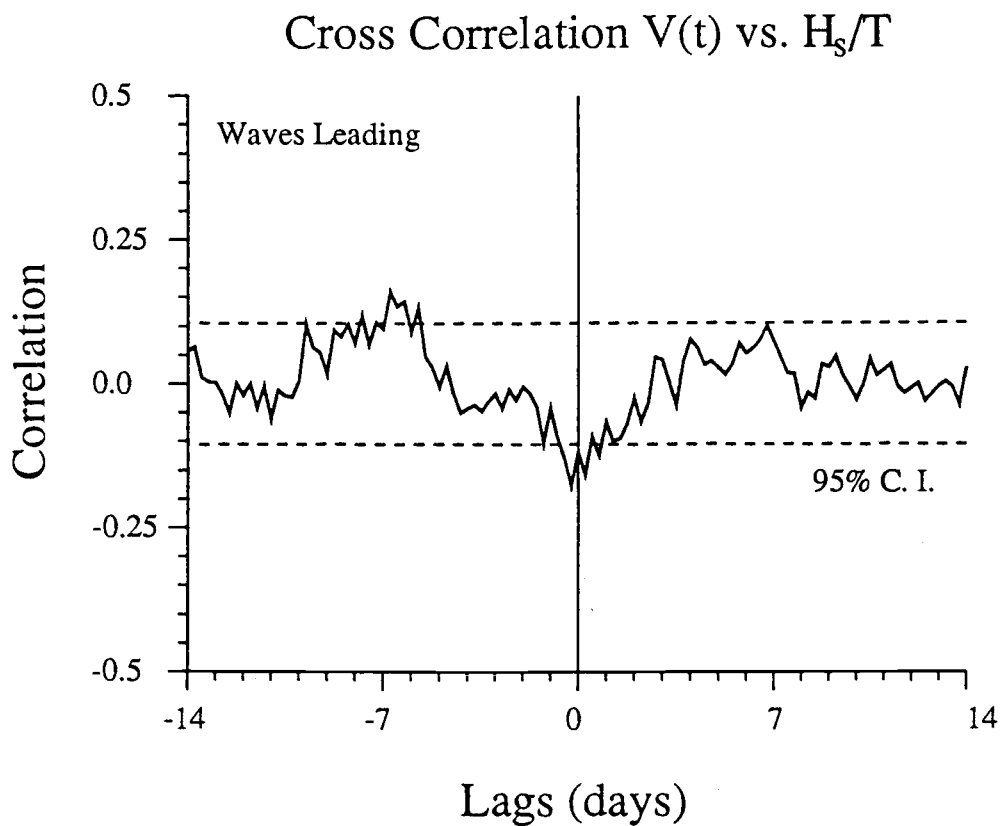


Figure B - 9. Cross correlation $V(t)$ vs. H_s/T for lags out to ± 14 days. The negative lags indicate waves leading. The 95% confidence intervals (dashed lines) were calculated using the long-lag artificial skill method after Davis, 1976.

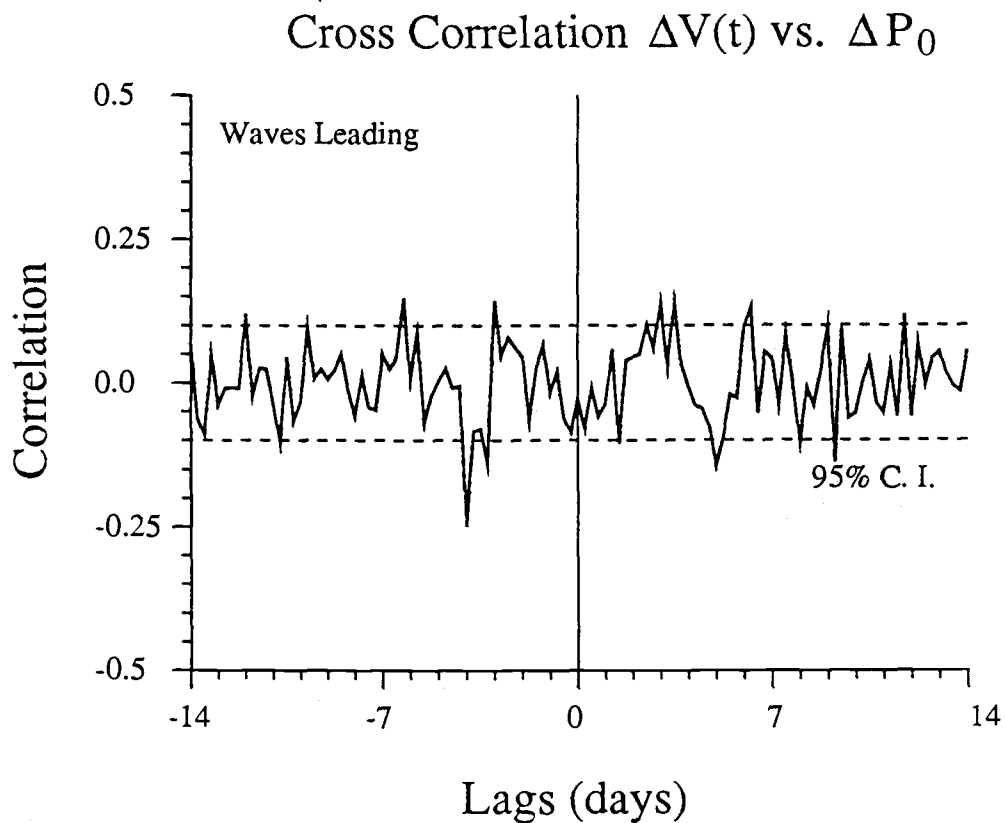


Figure B - 10. Cross correlation $\Delta V(t)$ vs. ΔP_0 for lags out to ± 14 days. The negative lags indicate waves leading. The 95% confidence intervals (dashed lines) were calculated using the long-lag artificial skill method after Davis, 1976.

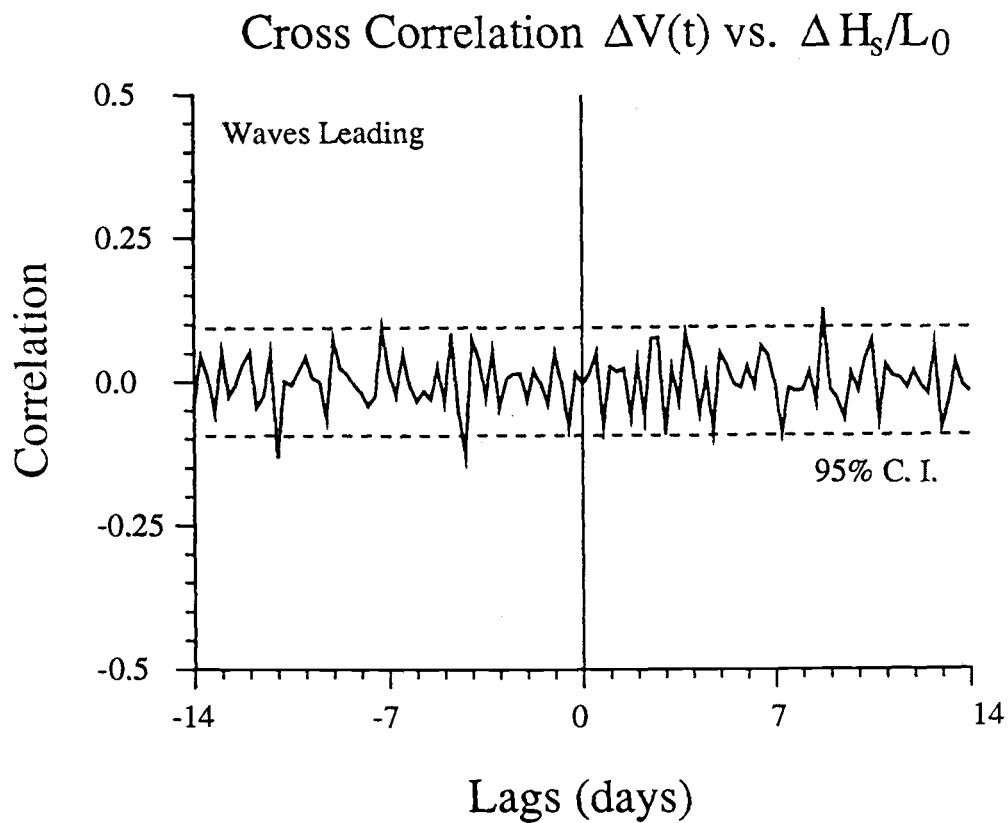


Figure B - 11. Cross correlation $\Delta V(t)$ vs. $\Delta H_s/L_0$ for lags out to ± 14 days. The negative lags indicate waves leading. The 95% confidence intervals (dashed lines) were calculated using the long-lag artificial skill method after Davis, 1976.

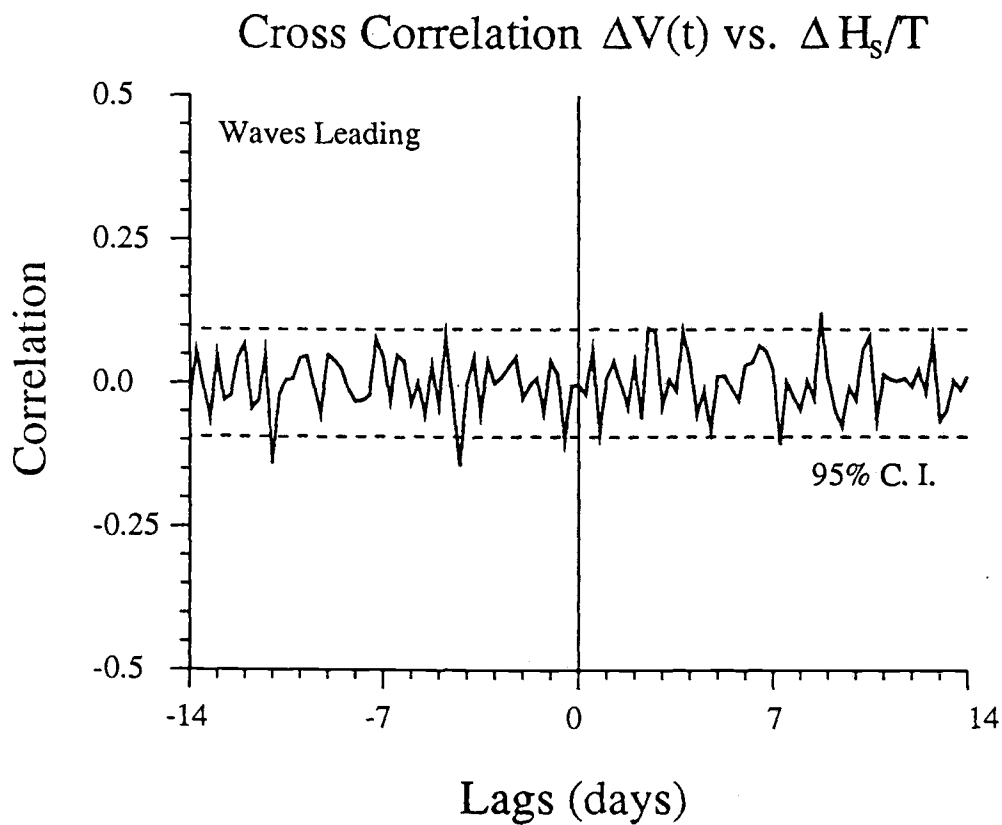


Figure B - 12. Cross correlation $\Delta V(t)$ vs. $\Delta H_s/T$ for lags out to ± 14 days. The negative lags indicate waves leading. The 95% confidence intervals (dashed lines) were calculated using the long-lag artificial skill method after Davis, 1976.